Thèse de doctorat

université
PARIS-SACLAY

Numerical simulation of the shock wave-boundary layer interaction in complex geometries

Thèse de doctorat de l'Université Paris-Saclay

École doctorale n° 579, sciences mécaniques et énergétiques, matériaux et géosciences (SMEMAG)
Spécialité de doctorat: mécanique des fluides
Unité de recherche: Université Paris-Saclay, Univ Evry, LMEE, 91020, Evry, France.
Référent: : Université d'Evry-Val-d'Essonne

Thèse présentée et soutenue à Evry, le 10/09/2020, par

Adarsh Baboo GUPTA

Composition du jury:

Christian TENAUD Directeur de recherche, LIMSI - CNRS	Président
Prakash Shamarao KULKARNI Professeur, Indian Institute of Science, INDIA	Rapporteur
Laurent DALA Professeur, Northumbria University, UK	Rapporteur
Ghislain TCHUEN Professeur-HDR, University of Dschang, CAMEROON	Examinateur
Bruno CHANETZ Directeur de recherche-HDR, ONERA	Examinateur
Luc LEGER Maître de Conférences-HDR, ICARE CNRS / Université d'Orléans	Examinateur
Amer CHPOUN Professeur-HDR, Université d'Evry-Val-d'Essonne	Directeur de thèse
Guillaume FOURNIER Maître de Conférences, Université d'Evry-Val-d'Essonne	Coencadrant de thèse

Acknowledgement

Foremost, I would like to show my sincere gratitude to the thesis director Professor Amer CHPOUN and co-supervisor Dr. Guillaume FOURNIER for the motivation and continuous support for my thesis work. Their vast knowledge of the subject, patience, and dedication have inspired me a lot for my research work and writing of this thesis, without them it was not possible for me to make my research successful.

I am very grateful to Professor Laurent DALA and Prakash S. KULKARNI for accepting being part of my defense jury and eventually reviewing the manuscript. They made several important suggestions which enhanced this edition.

A special thanks to Professor Christian TENAUD for being the president of my defense jury and his valuable suggestions and encouragement throughout my thesis.

I would like to thank Mr. Bruno CHANETZ, Prof. Ghislain TCHUEN, and Dr. Luc LEGER for being examiners, their encouragement, insightful comments, and hard questions.

I would like to thanks the lab director Professor Olivier QUEMENER, who has always been supportive.

I thank my fellow labmates: Dr. Pramod Kumar Chauhan, Dr. Benjamin Gaume, Dr. Sebastien Grosjean, Ms. Ana Gabriela Chavez, Mr. Sushil Sharma who have always supported academically as well as non-academically.

I am specially thankful to my family. No words can express how grateful I am to my parents. They always supported me morally, emotionally, and motivated me to accomplish my goals. I am thankful for almighty that He kept me thinking positive in all situations.

At the end, I am thankful to my beloved wife Geeta Gupta who was always there for me.

Synthèse en français

Les phénomènes d'écoulement supersonique connus sous l'intitulé de Interaction Onde de Choc Couche Limite ou Shock Wave Boundary Layer Interaction (SWBLI) constituent une classe de problèmes en aérodynamique supersonique très largement étudiée à la fois sur le plan expérimental et par les approches théorique et numérique. En effet, ces phénomènes apparaissent dans presque toutes les situations d'écoulements à grande vitesse avec des implications dans les industries aéronautique et aérospatiale. L'écoulement transsonique autour d'un profil d'aile, l'écoulement supersonique sur les surfaces de contrôle d'un engin spatial, les écoulements à l'intérieur d'une entrée d'air ou d'une tuyère propulsive sont autant d'exemples bien connus. Par exemple, l'interaction entre une onde de choc et une couche limite provoque sous certaines conditions (angle de choc ou de rampe, ou nombre de Mach...), un décollement de la couche limite qui conduit à une configuration très complexe d'écoulement. La bulle de recirculation est dans certaines circonstances instable et influe sur le système d'ondes de choc composé des chocs de séparation et de recollement ainsi que d'un train d'ondes de détente. La bulle de recirculation ainsi que le choc réfléchi sont connus pour être soumis à des oscillations longitudinales de très basses fréquences. Ces oscillations peuvent s'étendre sur quelques dizaines d'épaisseur de la couche limite initiale. La source de ces oscillations n'est pas encore complètement connue, mais deux hypothèses principales ont été avancées qui indiquent que celles-ci pourraient être dues soit aux structures tourbillonnaires dans la couche limite entrante ou soit à la création de structures cohérentes (tourbillons) dans la couche de mélange/ cisaillement en aval du point de séparation. Dans le passé, de nombreuses études concernant l'instationnarité de ces interactions ont été menées dans le cas de la couche limite entrante turbulente et mais très peu ont traité de la couche limite laminaire. Certaines des études précédentes ont conclu que le mouvement dans le sens de l'écoulement à basse fréquence est probablement associé aux structures irrégulières de la couche limite entrante.

L'objectif du présent travail de thèse est de fournir une meilleure compréhension des phénomènes physiques responsables des oscillations longitudinales à basse fréquence de la bulle de séparation. Afin d'étudier ce mouvement à basse fréquence, des Simulations Numériques Directes (DNS) de l'interaction entre l'onde de choc et la couche limite laminaire dans des géométries complexes ont été réalisées. Pour réaliser ces simulations, un solveur DNS/LES massivement parallèle (MPI), basé sur la méthode des volumes finis et développé au LIMSI-CNRS a été utilisé. Le solveur Chorus utilise un schéma de capture de choc Monotonicity-Preserving d'une précision d'ordre 7 en espace et en temps basé sur la méthode de Lax-Wendroff, pour les flux convectifs des équations de Navier Stokes. Les flux diffusifs sont discrétisés par un schéma centré de second ordre. Le code initialement

prévu pour les coordonnées cartésiennes rectilignes a été testé et validé pour la prise en compte des coordonnées curvilignes pouvant ainsi traiter les écoulements dans des géométries complexes.

La première partie du manuscrit est consacrée à la validation de l'approche numérique. L'influence de la distorsion du maillage a été analysée à partir de plusieurs cas-test. Les erreurs introduites par différents types de déformation pour les trois cas-test considérés (advection, turbulence et écoulement avec onde de choc) ont été analysées. Dans la mesure où les volumes de contrôle restent proches d'un parallélépipède, il a été montré que les erreurs dues à la déformation restaient faibles. Dans certains cas, il a été observé que l'introduction d'une non-orthogonalité du maillage entrainait une augmentation significative de ces erreurs.

La deuxième partie du travail de thèse concerne la validation du code dans le cas de l'écoulement supersonique autour d'une rampe de compression, qui est le cœur de la présente étude. Les validations ont été réalisées dans le cas d'écoulements non visqueux et visqueux sur une rampe de compression et la comparaison avec des données théoriques et numériques a été présentée. Cette comparaison a montré que les résultats obtenus avec le code CHORUS sont en bon accord avec les données de référence. Cependant, ces études sont assez anciennes (fin des années 1970) et de nombreux progrès ont été réalisés dans les méthodes numériques pour les simulations d'écoulements à grande vitesse. Malheureusement, comme cela a été mentionnée précédemment, il y a très peu d'études récentes concernant des simulations ou des expériences d'écoulement entièrement laminaire autour de rampes ou d'autres géométries complexes qui auraient pu aider à évaluer la capacité de CHORUS à calculer de tels écoulements. Il a donc été décidé de créer un cas-test à l'aide d'un solveur d'écoulement supersonique bien documenté et largement testé, rhoCentralFoam du package numérique open-source OpenFOAM. Les résultats obtenus ont montré un assez bon accord au vu des différences fondamentales entre les deux approches numériques. Ceci nous a donc permis de considérer que le code CHORUS pouvait être utilisé avec une grande confiance pour réaliser des Simulations Numériques Directes dans le cadre d'écoulement compressibles autour de géométries complexes.

En conséquence, le dernier chapitre s'est attelé à l'analyse physique de l'écoulement crée par le développement d'une couche limite laminaire autour de deux géométries : une rampe de compression classique et une rampe de compression-détente. Comme il a été dit précédemment, le but de ces simulations était de déterminer si les oscillations basse-fréquence de la zone de recirculation pouvaient être reliées à la présence de structures cohérentes dans la couche limite incidente. Les résultats ont montré que, dans les deux configurations testées, aucune oscillation n'est observée sur le choc de décollement ou sur la bulle de recirculation. L'analyse des spectres obtenus grâce à des sondes situées au voisinage du choc de décollement a néanmoins mis en évidence que toutes les fréquences associées aux oscillations étaient présentes dans ces signaux. La conclusion de cette étude est que l'absence des oscillations n'est pas, comme pensé initialement, due à l'absence de structures tourbillonnaires dans la couche limite incidente mais plutôt au fait que, dans le cas laminaire, la taille de la zone de recirculation est extrêmement importante. Ainsi, même si les perturbations responsables des oscillations dans le cas

turbulent sont également présentes en régime laminaire, elles sont trop amorties pour pouvoir déplacer le choc de décollement et/ou la zone de recirculation. La prochaine étape de ce travail devra donc consister à réduire soit le nombre de Mach à l'infini, soit l'angle de la rampe afin d'obtenir une zone de recirculation plus courte et d'observer si les oscillations apparaissent dans ce cas.

Contents

List of Figures

List of Tables

Introduction

General context

In the past, it was a dream for humans to fly faster and higher in the sky. Today, it is possible to say, the tremendous efforts of great scientists and engineers converted this human dream into reality such as the development of high-speed space vehicles. This endeavour culminated in the aftermath of WWII during the 50's and 60's in the context of strategic competition between the two superpowers of the time, i.e., United States (US) and Union of Soviet Socialist Republics (USSR) to achieve the goals of setting the first artificial satellite and sending the first man into the orbit and later landing on the moon. These steps, in the space conquest, were taken mainly with the help of German rocket scientists in the US and also partly in the USSR. Launch system design, calibration, and performance were mainly obtained by analytical approaches and with the help of the limited computational capabilities. Time constraint and limited computational capabilities resulted, in some cases, to oversize parts of systems.

After some drawdown during the 70's and 80's, a renewed interest in space activities is witnessed in the past two decades. This trend corresponds to the emergence of new competitor nations (Europe, Japan, India...) in the domain and also some private competitors. This new competition is mainly driven by economic interests rather than the strategic advantage and prestige as was for the first wave. Also, it arrives in the time of formidable progress in computational capabilities, numerical methods, and algorithms. So, nowadays, complex physical and particularly fluid flow phenomena with system sizing implication could be analyzed and as a consequence, the system performances could be optimized. It can contribute, for example, to increase payload or to use fewer propellants.

Among fluid flow phenomena, shock wave boundary layer interactions constitute a class of problems in the supersonic/hypersonic aerodynamics (figure 1) which was extensively investigated both theoretically and experimentally [129, 98, 62, 136, 18, 44]. Such interactions feature some fundamental aspects of supersonic fluid flows such as:

- Incident shock wave interaction with a developing boundary layer

- Viscous strong and weak interactions

- Flow separation

- Flow unsteadiness

- Shock-shock interactions

- Turbulence

- Vortex

- Etc.
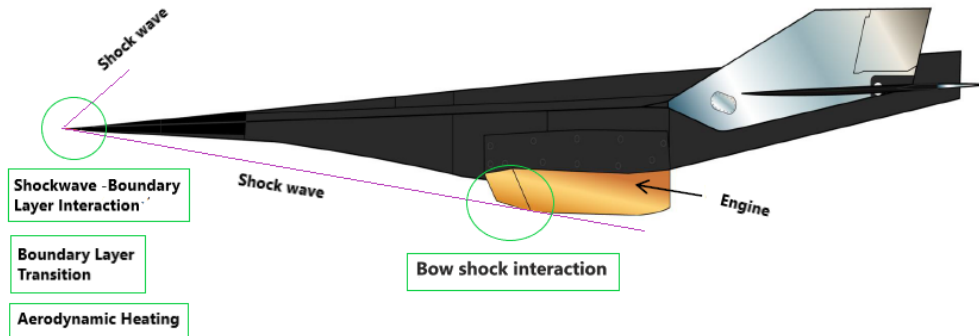
Figure 1: The aerodynamics environment of a supersonic/hypersonic aircraft.

In aeronautical and aerospace industries, the interactions between a shock wave and a boundary layer have a clear appearance almost in all high-speed flow. The supersonic flow over a flat plate, over a compression ramp and inside an air-intake, a nozzle, and a diffuser are well-known examples of these types of interactions. A brief explanation of these interactions environment are discussed below:

Shock wave boundary layer interactions take place in the flap/wing or body/wing junctions of a space vehicle. For some incoming flow conditions and geometry, flow can separate locally which drastically affects the flap efficiency and vehicle performance. Also, at the flow reattachment region on the flap, severe overheating could be expected to put the integrity of the vehicle in danger, if not taken properly into the account. The generic model of such flow situations known as ramp flows were extensively investigated in the past by experimental [25, 46, 134] and numerical means [28, 104, 162]. Incident shock wave/boundary layer interactions also take place in the air intake of supersonic/hypersonic vehicles powered by Scramjets (figure 2) [114, 17, 91, 165, 92].
Flow separation, shock-shock interaction can affect drastically the air intake efficiency leading to poor combustion and loss of propulsive power. Finally, as the last example, shock wave/boundary layer and shock-shock interactions take place in the divergent of a propulsive supersonic rocket nozzle particularly during the under-expansion regime at the lower altitudes of a given flight mission. Associated boundary layer separation and related shock wave (Fig. 3) impact on the inner nozzle wall can dramatically affect the specific impulse of the engine [4, 122, 111, 110, 72]. In all these flow situations, laboratory experiments and in-flight recorded data had shown flow unsteadiness, both in the streamwise and spanwise directions which may provoke harmful side loads in the case of the supersonic nozzle.
For the ramp flows, the reattachment shock wave unsteadiness was reported in the late 70's [46, 47]. This unsteadiness in the reattachment region of the ramp flow was reported in presence of complex transverse vortex structures (Görtler vortex) [10, 33, 155, 105,
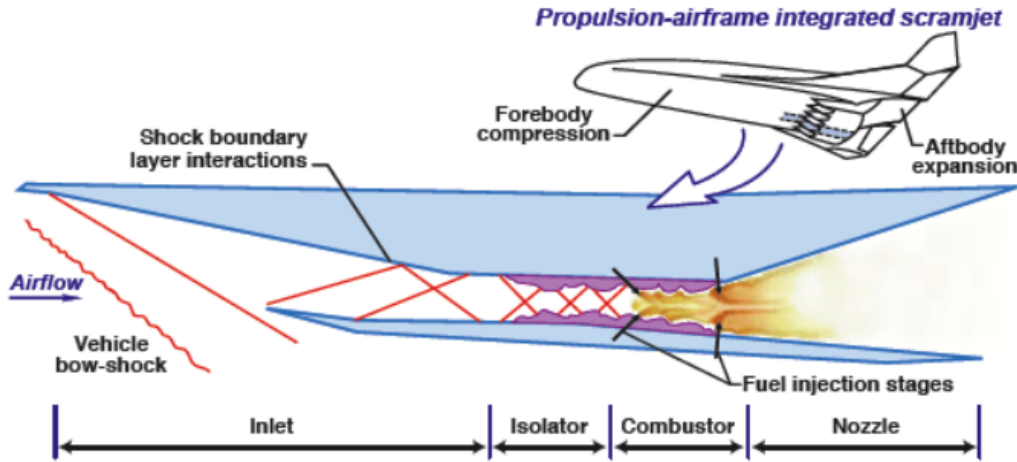
Figure 2: Flow-field characteristics of scramjet engine [145].
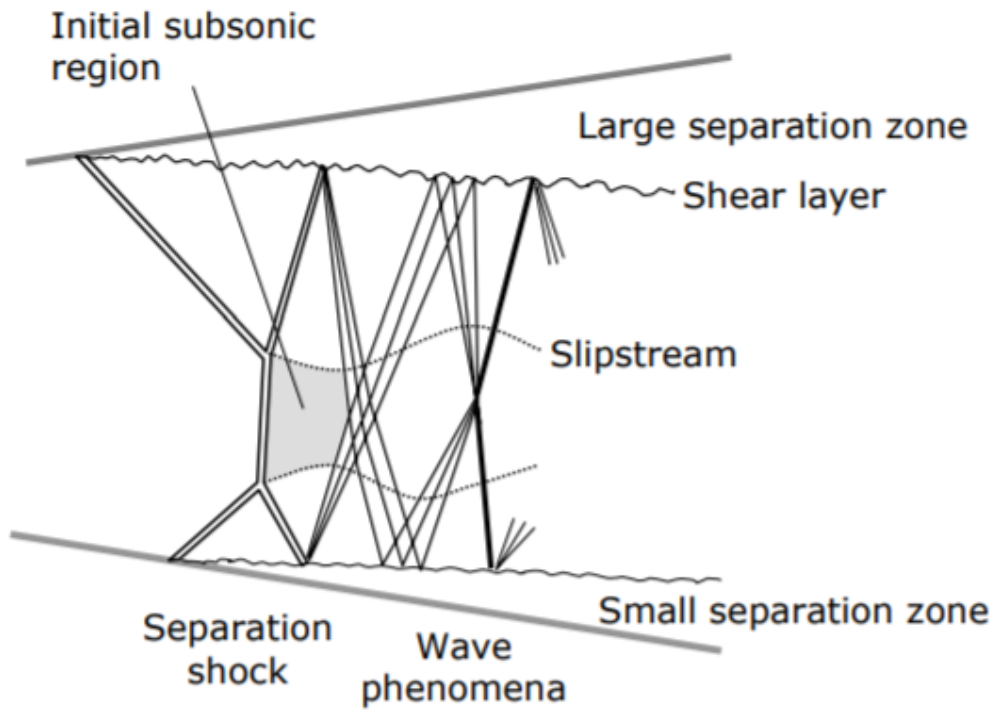
Figure 3: Principle phenomena in a supersonic nozzle at under-expanded regime [83].

104, 68]. In the case of the incident shock wave on a boundary layer (figure 4), similar reattachment shock unsteadiness was noticed in many studies [50, 53, 40, 95].
For some researchers, the flow, reattachment shock unsteadiness, and frequency could be related to the upstream incoming turbulent boundary layer features while others attribute the unsteady character of the separation to the downstream shear layer associated with shock-shock interaction region of the flow.

Although in some theoretical studies, stability analyses were carried out [126, 150], the mechanism behind the flow unsteadiness in such cases is yet to be truly known. In the early decades of the twentieth century, the experimental approach was the only source
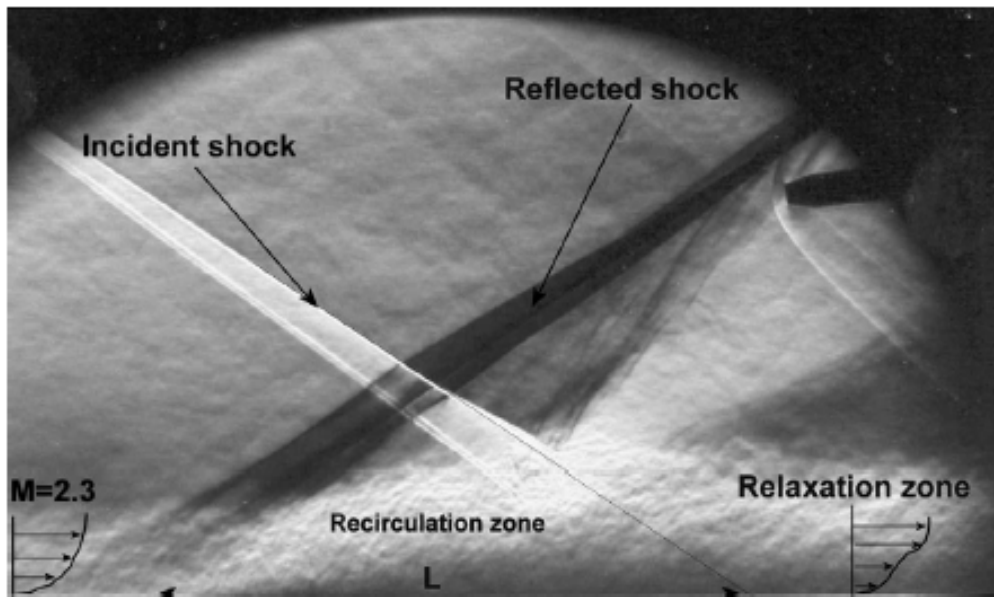
Figure 4: Schlieren of interaction between an incident shock wave and supersonic boundary layer [53].

to understand the flow unsteadiness in SWBLI. On the numerical side, the classical numerical methods such as RANS (Reynold Averaged Navier-Stokes) have no intrinsic capability to deal properly with supersonic flow unsteadiness. However, new advancements in computational capabilities and high-resolution numerical techniques have proved the possibilities to obtain important information from numerical simulations. Also, provide us an opportunity to closely examine the complex physical phenomena such as SWBLI in supersonic/hypersonic flows in recent decades. The emergence of modern numerical methods such as Large Eddy Simulation (LES), Direct Numerical Simulation (DNS) with high-resolution numerical schemes constitutes a powerful tool to apprehend such complex unsteady flow phenomena. However, these methods are highly time and memory consuming even with modern high-speed computers.

Study of the Subject

The interactions between shock waves and boundary layers have an interesting historical background and great strides have been made in the field of experiments and computational simulations over the last several decades. These interactions represent all kinds of complex fluid dynamics phenomena. The representation of these phenomena of interaction involves the coupling between the high-speed inviscid streams (inertial-dominated region) and low-speed boundary layer flows (viscous dominated region). The results of these phenomena were noticed as an adverse enlargement of the boundary layer due to the strong variation in pressure and temperature across the shock. Moreover, these phenomena generally lead to aerodynamic heating in re-entry vehicles, loss in performance of the aerodynamic devices, and large-scale unsteadiness that could cause additional problems such as buffeting in the aircraft's wings, air intakes' buzz that could be respon-

sible for structural fatigue [29, 49]. This is the reason, these interactions are demanding areas of study in the aeronautical/aerospace industries for both internal and external aerodynamics.

The interaction between a shock wave and a boundary layer provokes a premature shock-induced separation under any given circumstances such as high deflection in shock/ramp angle or high Mach number. This separation could create an unsteady recirculation bubble and, subsequently, a complex shock system consisting of the separation and reattachment shocks, as well as a fan of expansion waves. The oscillations of the recirculation bubble as well as of reflected shock were noticed around the separation point in the form of low-frequency streamwise motion that could develop over some tenth of boundary layer thickness [120, 9]. The source of these oscillations is still not completely understood, but there are two strong premises which indicate that either it could be due to the random structures in the incoming boundary layer [64] or to the shedding of coherent structures (vortices) in the mixing/shear layer downstream of the separation point [120, 11].

There are several studies in the past three decades that concerned the SWBLI unsteadiness by dealing with the turbulent boundary layer and only a few studies dealing with the laminar boundary layer [60, 131, 126]. Previous studies concluded that the low-frequency streamwise motion is likely to be associated with the irregular structures in the incoming boundary layer. The aim of the present thesis work is, therefore, to manifest that the streamwise motion still appears with an incoming laminar boundary layer and provides a better understanding of the possible source of this low-frequency streamwise motion. In order to investigate low-frequency streamwise motion, the DNS studies are performed in this current thesis project for the interaction between the shockwave-laminar boundary layer in two different complex geometries: a classical compression ramp and compression-expansion ramp.

Objective of this current study

The objective of the current thesis is to describe the physical behaviour of shockwave-laminar boundary layer interactions in the supersonic flow by using an in-house parallel (MPI) Finite-Volume based DNS/LES solver named as CHORUS developed at LIMSI-CNRS. This code was initially built for a cartesian mesh. The ability of code to deal with the curvilinear mesh system was never checked before. In order to deal with complex geometries, we modified the original version of this code. To check the ability of this modified code, the DNS simulations were performed on several test cases. The SWBLI unsteadiness and the possible source of low-frequency streamwise motions in the interaction environment of complex geometries are of particular interest. To develop the well-oriented framework for the current research study in order to meet the final goal, the objective of this thesis is divided into three-part:

Primary objective

To check the ability of the numerical scheme, computational analysis of several canonical test-cases (Advection-diffusion case, Taylor-Green Vortex, and presence of a shock...)

were performed in curvilinear coordinates. Every case has been selected for their own peculiarities and because reference data were available.

Intermediate objective

Before innovative DNS is performed, the code needs to be validated on the framework of supersonic flows around a compression corner, which is the core of the present dissertation. The validation studies have been carried out for the case of both inviscid and viscous flows over a compression ramp and the comparison with theoretical as well as numerical data will be presented. However, those studies are rather old (the late 1970s) and a lot of progress has been made in numerical methods for high-speed flow simulations. Unfortunately, as it was mentioned earlier, there are very few (to say the least) recent studies concerning simulations or experiments of fully laminar flow around ramps or other complex geometries that could have helped to assess Chorus' ability to compute such flows. It has then been decided to create our own test case, using a well-documented and extensively tested supersonic flow solver, rhoCentralFoam of the OpenFOAM open-source numerical package.

Final objective

The main objective of the current thesis is to perform DNS and physical analysis of three-dimensional unsteady shock wave-boundary layer interaction for two complex geometries: a classical compression ramp and compression-expansion ramp. Indeed, in order to deeply understand the low-frequency unsteadiness of the separation bubble, we consider the interaction between a shock wave and a laminar boundary layer, in which no incoming turbulent structures are encountered. Also, check that this low-frequency longitudinal motion of the separation bubble is recovered in the laminar regime or not while it is present in the turbulent case.

Outline of this thesis

Chapter 1 is dedicated to reviewing the important previous studies done in the field of physical analysis of SWBLI and modeling of supersonic/hypersonic flow. The focus is placed on studies involving various aspects of SWBLI in different interaction environments.

Chapter 2 discusses the numerical modeling of the governing equations. This numerical modeling is discussed with regard to numerical approach, domain size and discretization, boundary conditions and physics modeling.

Chapter 3 reviews the validation studies of the numerical scheme on distorted meshes (curvilinear mesh) for several canonical test cases (Advection-diffusion case, Taylor-Green vortex, and presence of a shock...).

Chapter 4 dedicated to checking the ability of the code (CHORUS) for the supersonic flows around a 2D compression corner in both the inviscid and viscous flow.

Chapter 5 presents the Direct Numerical Simulation (DNS) for three-dimensional unsteady SWLBLI in two complex geometries. A deep concentration is applied to the analysis of low-frequency longitudinal motion of the separation bubble. Also, it justified that this low-frequency motion of the separation bubble is recovered in the laminar regime or not while it is present in the turbulent case.

Chapter 1

Literature Review

Contents

In this chapter, we introduce an overview of the previous studies obtainable in the literature of shock wave-boundary layer interactions. We started this chapter with a discussion of the importance of the SWBLI phenomenon. The second section presents the different geometrical configurations in which they experience this complex phenomenon. The third section describes the SWBLI phenomenon in the laminar flow. The fourth section is concerned about the important aspects (separation, unsteadiness) of SWBLI. The last part of this chapter discusses different numerical methods for high-speed flow.

1.1 Importance of shock wave-boundary layer interactions

As time is going on, human being's desire to touch the sky and all its limits is also in their mind. In order to fulfill the desire to reach the sky, one needs supersonic/hypersonic

aircraft and that requires deep study of several important fluid dynamics phenomena. One of the fascinating phenomena is shock wave-boundary layer interaction. The harmful consequences of this phenomena have already been observed in many incidents in the history of high-speed aerodynamics. These consequences made this topic thought-provoking and attractive.

Due to the strong aerodynamic heating, the worst incident of damage in X-15 hypersonic airplane was noticed on October 3rd, 1967. A hole through a surface of the pylon burnt due to this high aerodynamic heating. Later, it was found that the biggest cause of this aerodynamic heating was the interaction of a shock from the ramjet nacelle to the pylon. Moreover, the impingement of a bow shock from this pylon to the bottom surface of the X-15 airplane caused a region of local aerodynamic heat damage figure 1.1. Another harmful consequence of SWBLI is observed in the ramp-shaped inlet of the engine intakes [133]. According to the operating conditions, different arrangements of SWBLI for a mixed ramp-shaped inlet is shown in figure 1.2. In this case, the shock waves interact with the developing boundary layer at the inlet surface and produce an adverse pressure gradient that separates the boundary layer from several downstream locations of the inlet. This flow separation affects engine performance by reducing the overall pressure recovery. An additional effect of this separation is the flow distortion that introduces the low-frequency large-amplitude oscillations. These low-frequency oscillations are sometimes known as the inlet buzz that can lead to the engine surge and structural fatigue of the aircraft. The occurrence of this phenomenon is also noticed when high deflection is required in the flaps to stabilize the supersonic/hypersonic vehicles. The results of both the high deflection and SWBLI are found in the detachment of flow upstream of the flap due to the adverse pressure gradient [12]. This detachment consequently affects and minimizes the maneuverability of high-speed airplanes. The combination of all these consequences of this phenomenon results in the structural fatigue of the components and sometimes the complete body of the aircraft. One of the positive effects of this phenomenon is found in the strong mixing of the air-fuel mixture due to the enhancement in turbulence. The literature of SWBLI concluded that the number of negative effects of this phenomenon exceeds the positive effects. This is the reason why various researchers are still analyzing this hazardous phenomenon to examine closely all the consequences caused by it.

Figure 1.1: An example of aerodynamic heating due to SWBLI. X-15 hypersonic test airplane (left) and Damage in X-15 hypersonic airplane (right). From [8].
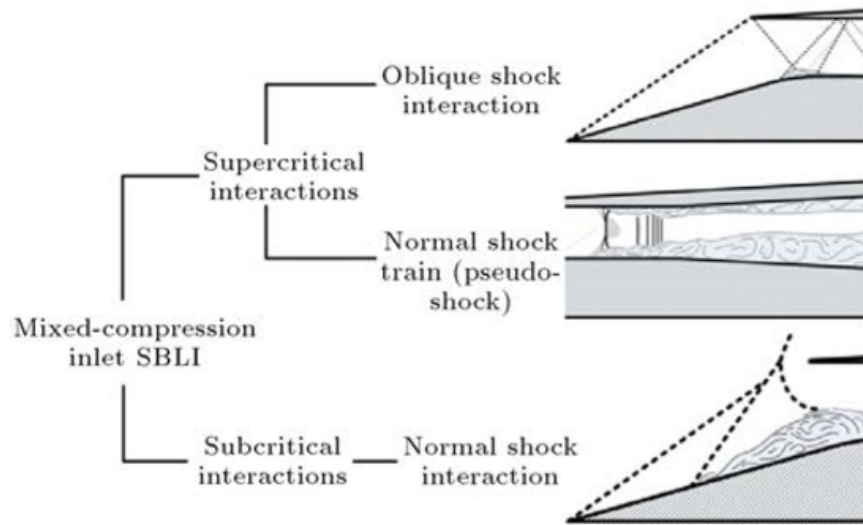
Figure 1.2: Different classes of SWBLI flow related to mixed ramp-shaped inlet. From [141].

1.2   SWBLI: Different interaction environments

1.2.1   Basic geometrical configurations

To understand the concept of SWBLI, it is important to consider the role of the surface geometries. It is because each geometry experience this harmful phenomenon but the appearance of interactions in each geometry is different and advantageous to study. The interaction of a shock wave with the developing boundary layer in different basic geometries are shown in figure 1.3 and have an important influence on far-field.

The first example (Fig. 1.3a) shows the supersonic flow over a 2D ramp. A reflected shock wave is reported in this type of configuration and the zone of interaction is influenced only by the upstream source of the disturbance. This configuration is an example of a short-range interaction (supersonic flow both the upstream and downstream of the interaction) and plays an important role at the control surface or when a change in the surface direction is required.

The second example (Fig. 1.3b) is a supersonic flow inside a channel. The zone of the interaction in this type of configuration is influenced by both the upstream and downstream source of the disturbances. A normal shock is reported in this configuration and the downstream disturbances are now available to propagate in the upstream through the subsonic region (close to the wall). This configuration is an example of medium-range interaction (supersonic flow upstream and subsonic flow downstream of the interaction).

The third example (Fig. 1.3c) is the transonic flow over an airfoil. The zone of interaction in this case is also influenced by both the upstream and downstream sources of the disturbances. The interaction in this type of configuration is no longer confined to happen in a closed duct so it is known as long-range interaction.

(a) Ramp

(b) Channel

(c) Transonic Airfoil
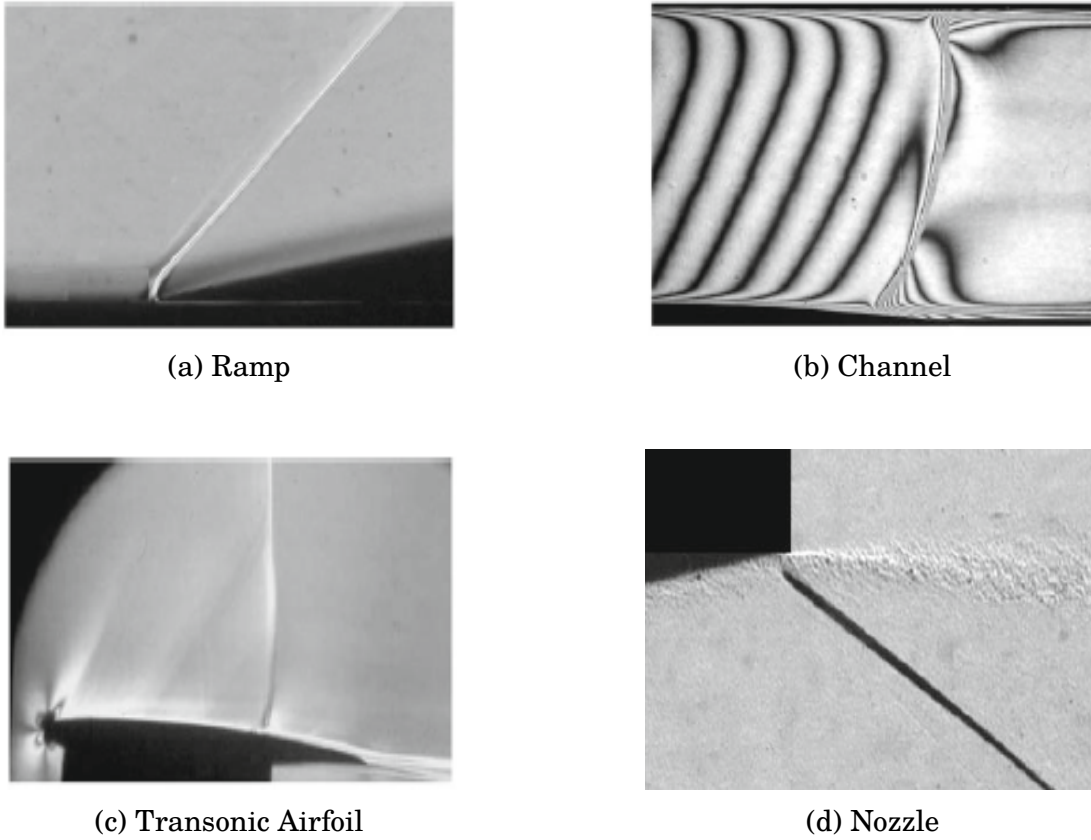
(d) Nozzle

Figure 1.3: Classification of shock wave boundary layer interaction in different environments. From [43].

The fourth example (Fig. 1.3d) is the supersonic flow at the exit of an over-expanded nozzle. An oblique shock appears due to the pressure difference at the exit of the nozzle. In this configuration, pressure discontinuity at the exit causes a flow deflection.

So far, we discussed SWBLI in basic geometries only but in order to achieve the objective of the current thesis, it is advantageous to analyze some other canonical configurations such as flow over a flat plate, a bump, a compression ramp, and double compression ramp (compression-expansion ramp).

1.2.2 SWBLI: Canonical configurations

Flat Plate

By considering this configuration, most of the literature in the past several decades provided a huge contribution to understanding the physical behaviour of SWBLI. The interaction of an incident shock with the developing boundary layer on the surface of a flat plate is shown in figure 1.4. Due to this interaction, strong variations in the pressure are notice behind the shock and performed as a strong adverse pressure gradient. This strong adverse pressure gradient separates the developing boundary layer from the surface of the flat plate.
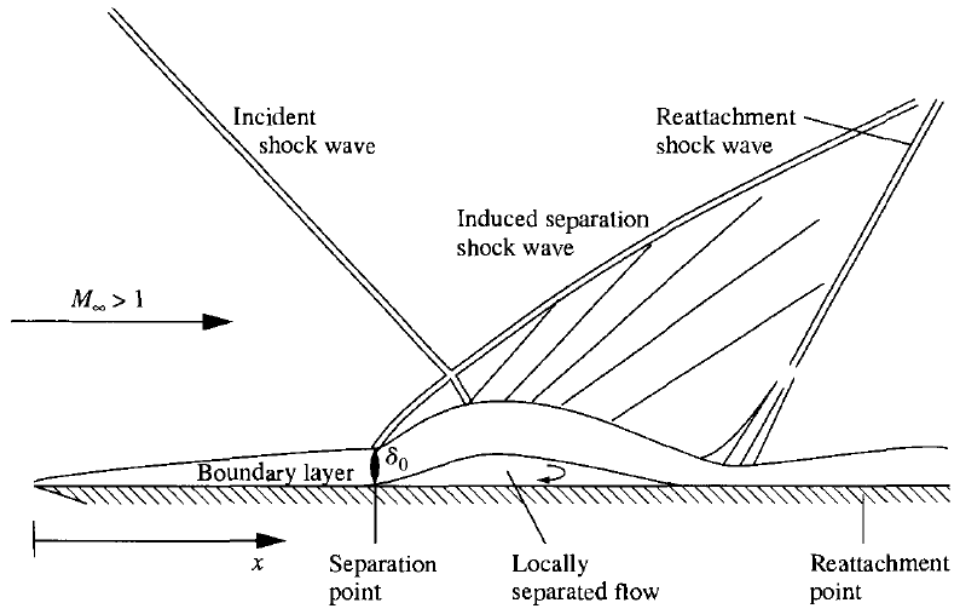
Figure 1.4: Interaction between the incident shock and the boundary layer on a flat plate. From [5].

The separation of the boundary layer happens slightly upstream of the interaction point of the incident shock. The high pressure across the shock feed upstream through the subsonic part of the boundary layer and disturb the incoming flow. Moreover, this separation of the boundary layer induces a separation shock at the separation point. As soon as this separated boundary layer starts to recover the surface of the flat plate, a pattern of multiple expansion waves is created. These waves turn the flow towards the surface and finally the boundary layer reattaches with the surface of the flat plate at the reattachment point. Another shock induces at the reattachment point known as the reattachment shock. A zone of strong aerodynamic heating is noticed at the reattachment point as the boundary layer became relatively thinner than the upstream boundary layer. A reflected shock is formed due to the combination of both the separation and reattachment shock, away from the surface of the plate.

Bump

The transonic interaction over the surface of a bump is shown in figure 1.5. Bumps are a well-known example of the canonical geometries that possess fascinating effects as a diversion system.
They play an important role in the diversion of the boundary layer due to both the favorable and adverse pressure gradients. The transonic flow (high speed subsonic) interacts with the lower surface of the bump and starts to accelerate the flow up to the supersonic speed and then decelerate the flow at the rear surface because of the bump curvature. This deceleration separates the boundary layer and forms a lambda-shock. The front leg of the lambda shock originates at the separation point of the boundary layer and the rear leg originates from the reattachment region. The applications of this type of interaction environment play an important role in the designing of transonic wings.

Figure 1.5: Transonic flow over a bump. From [96].

Compression ramp

The interaction environment over the supersonic compression ramp is shown in figure 1.6. When the supersonic flow encounters the surface of the compression ramp, the strong adverse pressure gradient generated by the compression ramp, enlarges the incoming boundary layer and eventually separates this layer from the surface. This separated boundary layer becomes a shear layer outer to a recirculation bubble around the compression corner. The boundary, by reason, is called the dividing line between the shear layer and the recirculation bubble. Further downstream, this shear layer interacts with the ramp in the reattachment region. Then the flow in the boundary layer continues to accelerate till the boundary layer and reaches a minimum thickness at the neck level. This interaction environment is different from the inviscid case where the discontinuity occurs at the deflection point by means of a single shock only.
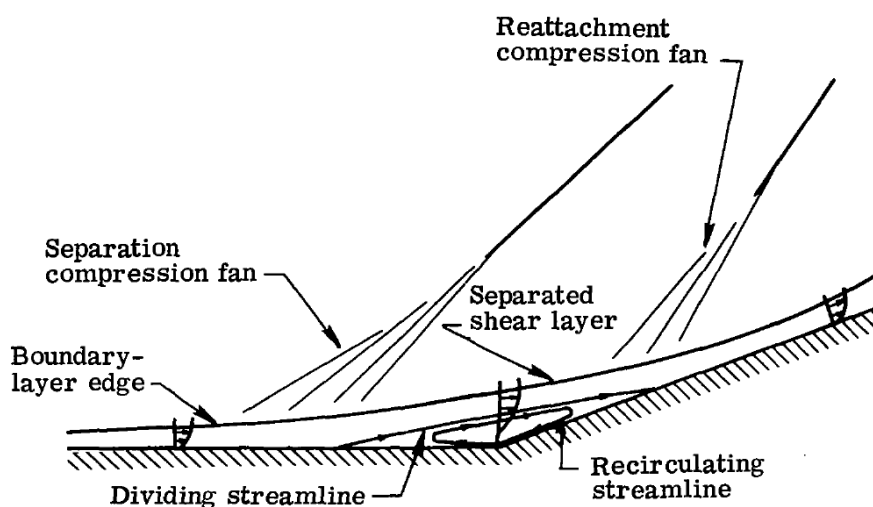
Figure 1.6: Supersonic flow over a compression ramp. From [28].

Compression-expansion ramp

The interaction environment of the double compression ramp (compression-expansion ramp) in supersonic flow is shown in figure 1.7.
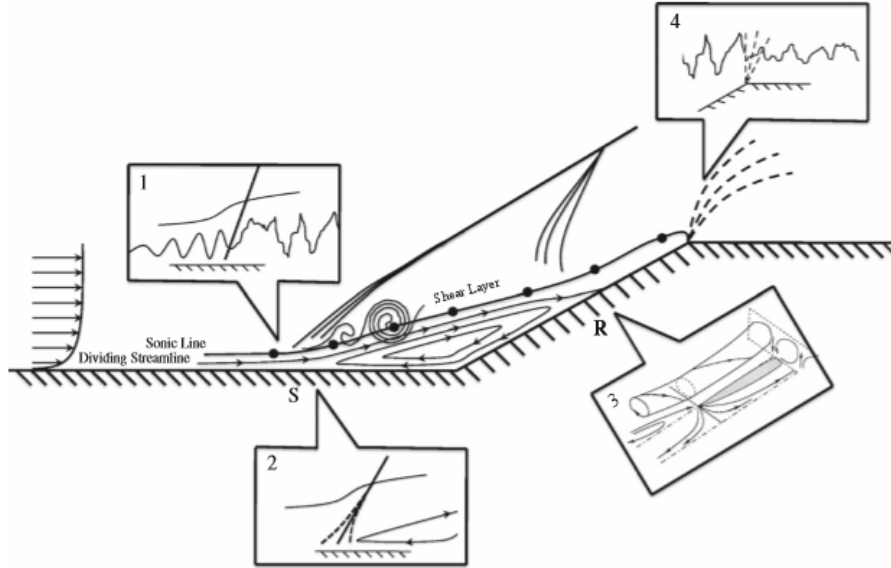
Figure 1.7: A schematic representation of the supersonic flow over a compression-expansion ramp. From [167].

The amplification in the turbulence level is found as a result of the interaction between the shock waves and the boundary layer (Inset 1). The possible relaminarization of the reverse flow is observed within the separated region due to the turbulent diffusion (Inset 2). The existence of the pairs of large counter-rotating streamwise vortices (Görtler vortices) is reported in the reattachment region as well as in the reverse flow of the separation zone (Inset 3). The interaction with Prandtl-Meyer expansion waves at the expansion corner caused the damping of the turbulent fluctuations (Inset 4). The positions of both the separation and reattachment points are indicated by **S** and **R** respectively.

1.3   SWBLI: Laminar flow

Most of the studies in the literature of SWBLI investigated the interaction of a shock with the turbulent boundary layer and only a few studies dealing with the laminar boundary layer. The insight flow physics of the laminar interaction made this phenomenon more interesting than the transitional or turbulent case. An earlier experimental study [1] investigated the laminar interaction in transonic flow, it is observed that the multiple shock structure (compression shock) depends on the incoming velocity. As the velocity (Mach number) increases, the multiple shock structure decreases and finally forms a lambda shock figure 1.8. A single lambda shock is observed beyond Mach 1.223.

In a flat plate case, Liepman *et. al.* [102] experimented and reported that the zone of interaction for a laminar flow can be several times longer than the turbulent case. Moreover, the process through which a reflected shock is generated in the region close to
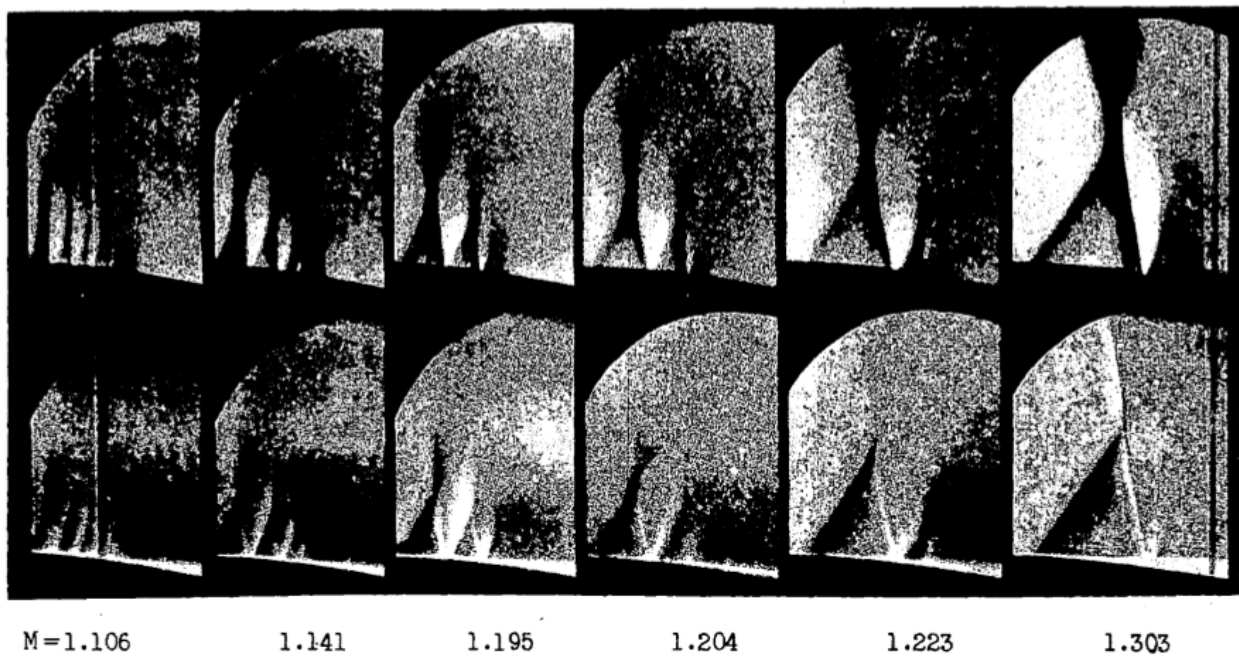
Figure 1.8: Schlieren illustration of lambda-shock with variation in Mach number. From [1].

the wall differs in the laminar interaction from the turbulent case and shown in figure 1.9.

(a) Turbulent flow   (b) Laminar flow

Figure 1.9: Reflected shock pattern. From [102].

Gadd *et. al.* [61] conducted a theoretical and experimental study for the laminar separation in the supersonic ramp flow to understand the effects of wall heating and cooling on the extent of separation. A tendency that the interaction extends further upstream and the pressure gradient correspondingly decreases as shown in figure 1.10, is noticed in the heated wall case.
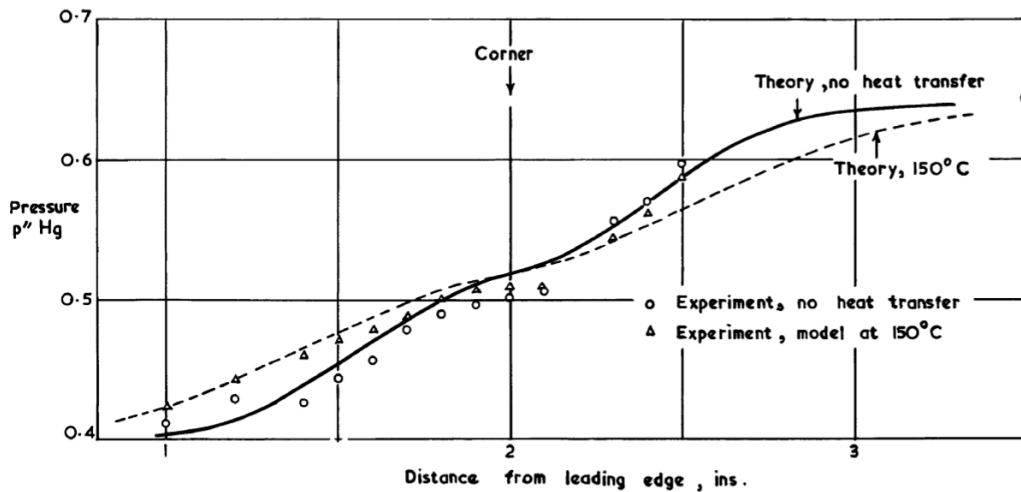
Figure 1.10: Comparison of theoretically and experimentally calculated pressure distributions. From [61].

Hakkinen *et. al.* [73] investigated the interaction between a shock wave and a laminar boundary layer on a flat plate. This study concluded that the pressure levels related to the separation depend only on the local conditions if the separated flow is adequately long. Furthermore, the length of the separated zone is almost proportional to the pressure rise that required to induce incipient separation. A study [25] based on the asymptotic triple-deck theory of the laminar boundary layer separation and reattachment is conducted for a supersonic compression ramp. All the triple-deck calculations in this study are based on the Stewartson-Williams' method [143] and reported that the regions of separation and reattachment become distinct with a plateau region of approximately constant pressure for large ramp angles shown in figure 1.11. Also, the available evidence in this study supports the aspect of this asymptotic theory of both the laminar separation and reattachment and is an adequate formulation for a practical purpose.

A similar study is carried out by Burggraf *et. al.* [26] for a comparison between the triple-deck theory based on Rizzetta, Burggraf, and Jenson's method [124] and the interacting boundary layer model based on Werle and Vats' method [159]. This study reported that the deficiency of this asymptotic theory is an experience, it is quantitatively accurate only at very high Reynolds number.

A combined experimental and numerical investigation is carried out by Degrez *et. al.* [42] for the interaction between the oblique shock wave-laminar boundary layer on a flat plate at Mach 2.25. This study closely examined the distribution of the pressure and velocity profile in the vicinity of the separation and reattachment zone as shown in figure 1.12. A good agreement is observed between the experimentally and numerically com-
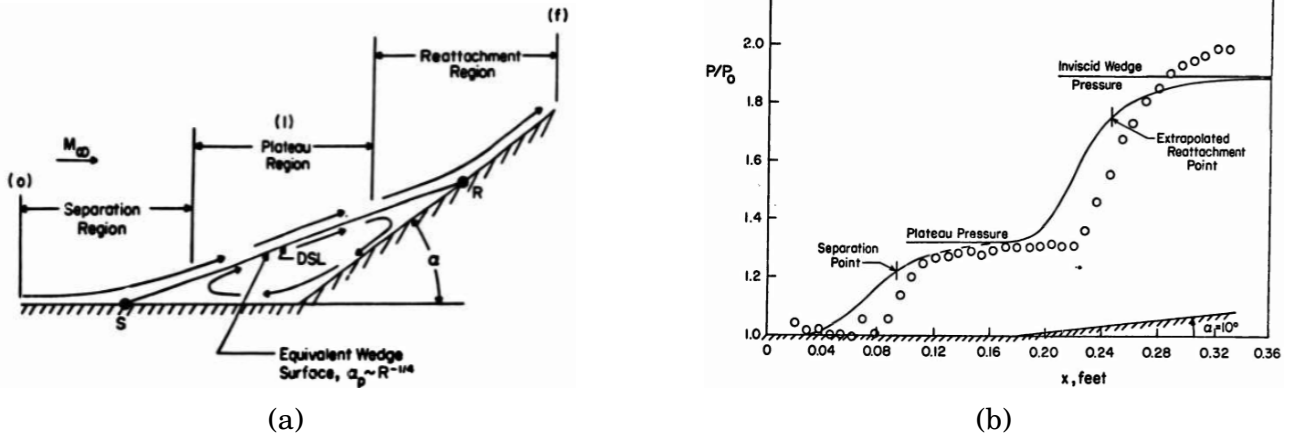
Figure 1.11: Laminar separation in compression ramp **(a)** and the theoretically calculated overall pressure distribution **(b)** at ramp angle $10°$. From [25].

puted velocity and pressure distribution in the upstream, separation, and reattachment region. A steeper pressure gradient at the reattachment point is observed in numerical computation than the experiment, there is no explanation for the same but a similar presence is noticed in another computational study [28].
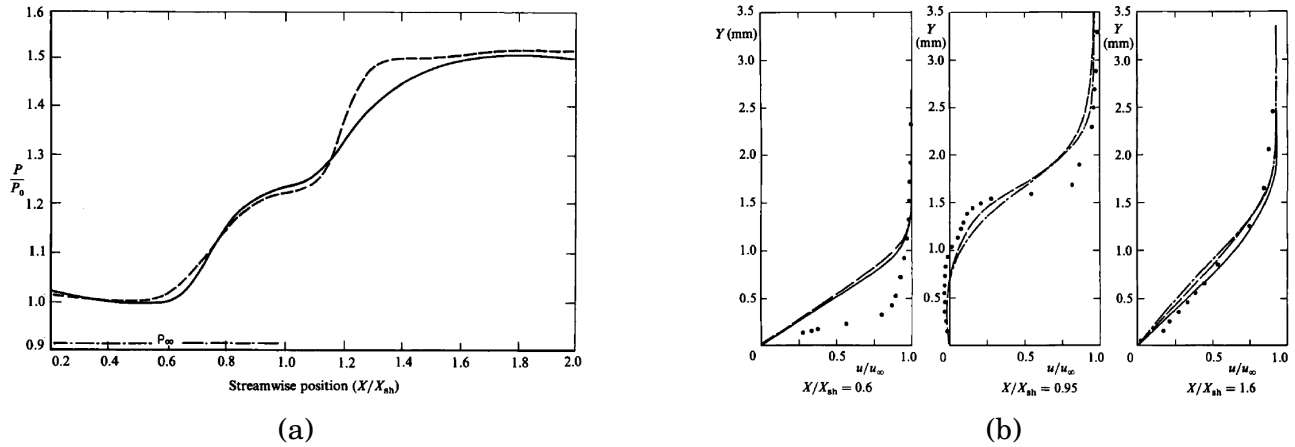
Figure 1.12: Comparison of pressure distributions **(a)** and velocity profiles at different locations **(b)**. From [42].

A computational investigation of the oblique shock-laminar boundary layer interaction is carried out for the range of Mach 1.4 to 3.4 and Reynolds number 1×10^5 to 6×10^5 [84]. The numerical results of this investigation reported that the extent of the separation bubble grows linearly with the strength of the incident shock and that in good agreement with the free interaction theory. A comparison of this numerical data with triple-deck theory shows a discrepancy in the estimation of the separation bubble's length scale. It is observed that the discrepancy increases with the increasing Mach number for a finite range of Reynolds numbers.

Several recent studies closely examined the complex physics of the shock wave-laminar

boundary layer interactions. Some aspects of the SWBLI unsteadiness are carried out by Robinet [126] for an oblique shock-laminar boundary layer interaction on a flat plate using DNS. This study found that the unsteadiness of the interaction region is not altered by the presence of upstream perturbations related to the mechanism of instabilities in the transition process. Moreover, this low-frequency unsteadiness of the interaction region emerges in a supercritical Hopf bifurcation associated with the passage of the separated boundary layer.

Recently, Fournier *et. al*. [60] performed DNS to examine the possible origins of the streamwise motions of both the shock-induced separation bubble and the reflected shock for the shock wave-laminar boundary layer on a flat plate. It is observed that the recirculation bubble moves upstream even if there are no oscillations which indicate that this movement is more likely due to the vortex shedding downstream of the separation. Moreover, strong shedding intermittency is evidenced figure 1.13, leading to the large-vortex free regions in the flow, responsible for very low-frequency mechanism.
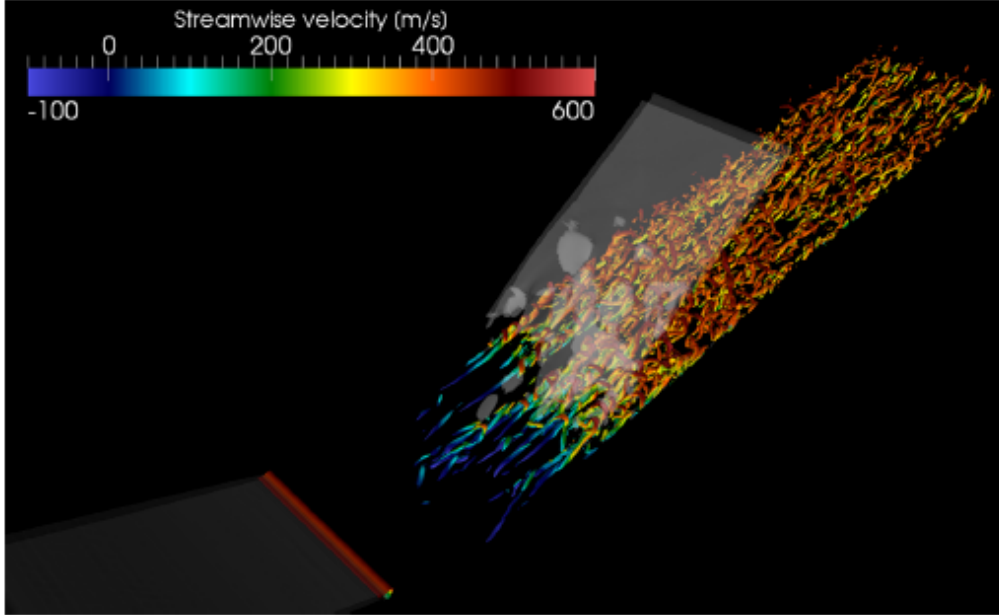
Figure 1.13: A schematic of coherent structures in the interaction region by using Q-criterion isosurfaces. From [60].

Giepman *et. al*. [66] conducted experiments for laminar and transitional oblique shock wave reflections by varying the Mach number (1.6 to 2.3), Reynolds number (1.4×10^6 to 3.5×10^6), and flow deflection angle (1° to 5°) on a flat plate. This study reported a long, flat, and triangular recirculation region for the laminar interactions figure 1.14. Moreover, for strong shock waves, the horizontal distance between the separation point and the top of the bubble increases linearly, although the horizontal distance remains nearly constant between the top of the separation bubble and the reattachment point with the shock strength. The boundary layer rests in the average laminar state upstream part of the recirculation bubble. However, transitions occur quickly after passing an incident shock wave.
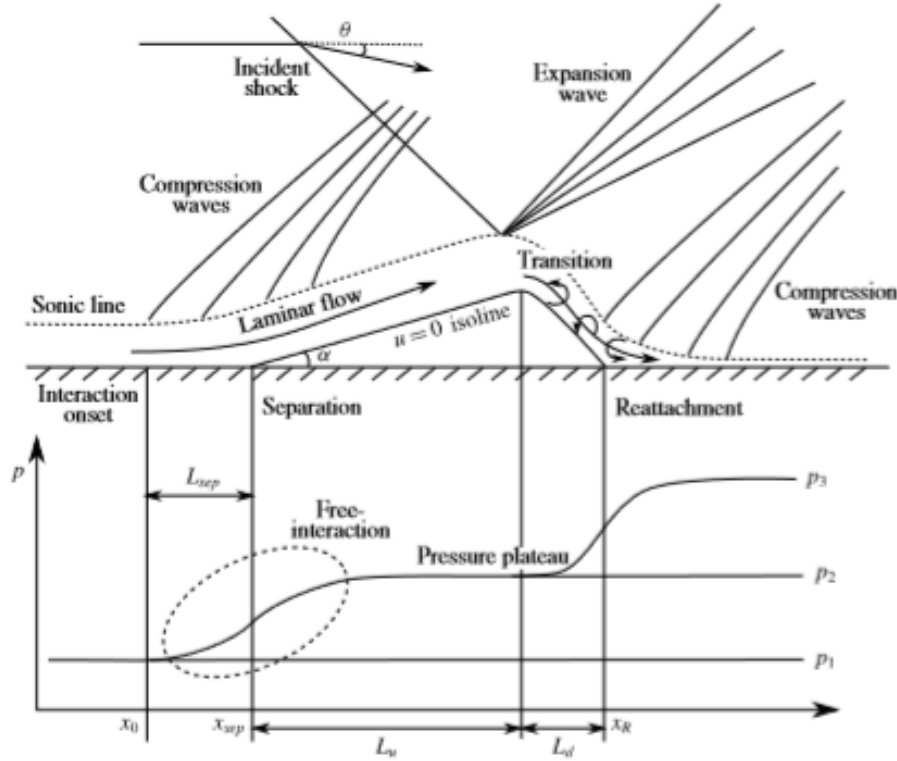
Figure 1.14: The pattern of reflection shocks in both the incoming laminar boundary layer and in the transition as well as the pressure distribution over the surafce of the wall. From [66].

1.4 Important and remarkable concerns of SWBLI

The interaction between the shock wave and the boundary layer represents all types of harmful fluid dynamics phenomena such as separation of the boundary layer, large scale unsteadiness, turbulence, huge variation in pressure and temperature, etc.. These harmful flow phenomena have a remarkable impact on both the external and internal surface of the aircraft as well as degrade the performance and maneuverability of the airplanes. Some of these flow phenomena are discussed here.

1.4.1 Separation of the boundary layer and formation of the recirculation bubble

In the past several decades, a large number of studies focused on the complex physical mechanism of SWBLI. These studies are helpful to deeply understand the complex structures of the flow separation induced by these interactions. The structure of this flow separation for both the laminar and turbulent cases is shown in figure 1.15.

When a strong incident shock impinges on the developing boundary layer, the strong pressure gradient behind the shock feed upstream through the subsonic stream of the developing boundary layer near the wall and eventually separates it from the surface of the wall. This separation originates from the separation point, located ahead of the impingement point of the incident shock. This separation forms a recirculation bubble
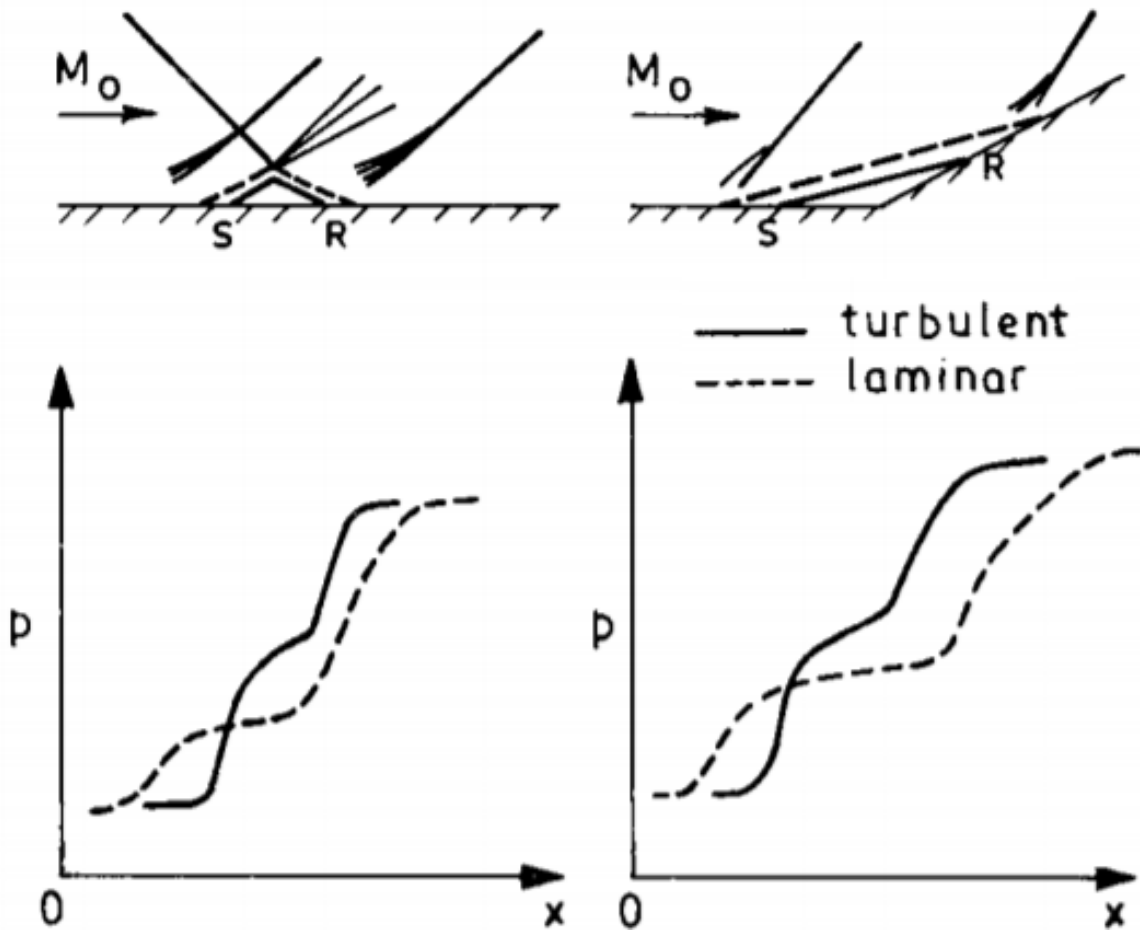
Figure 1.15: The shock pattern and distribution of wall pressure in the supersonic separated flow. From [156].

and proceeds from the reattachment point. The separated layer, originated from the separation point, becomes a shear layer that promotes the complex mixing caused by the energy transfer from the outer supersonic-inviscid stream into the separation region. This transformation of the mechanical energy, due to the complex mixing, causes the constant increment in velocity inside the shear layer until it overcomes the pressure gradient at the reattachment point. A sudden change in the pressure level at the separation and reattachment points, as well as constant pressure in the recirculation bubble due to the separation, is also shown in figure 1.15 [156]. Moreover, the overall increment in the pressure or pressure gradients due to the separation induced by the laminar interaction is lower than that of the turbulent case.

An experimental study [62] investigated the interaction between shock waves and boundary layers on a flat plate in supersonic flow. The results of this study noticed the importance of the boundary layer separation process and the transition in establishing the nature of the interaction. Moreover, the recirculation bubble is found in a triangular shape for the laminar interaction. Another experimental study [30] noticed the effect of Mach numbers and Reynolds numbers on the separation region. This study reported

that for supersonic flow, pure laminar separations are steady and depend only on a relatively small range of Reynolds numbers. The stability of the separated laminar shear layer increases with an increase in Mach number. Katzer [84] numerically investigated the interaction between an oblique shock and a laminar boundary layer for a range of Mach number 1.4 to 3.4 on a flat plate. The results of this study concluded that the length of the recirculation bubble is linearly dependent on the incident shock strength. Sivasubramanian and Fasel [139] performed DNS to investigate the shock-induced laminar separation bubble in the supersonic boundary layer with and without upstream disturbances. It is noticed in this study that the laminar recirculation bubble strongly amplified the upstream disturbances and the flow transitioned to the turbulence downstream of the bubble at higher shock strengths. The numerical study [131] of steady two-dimensional laminar interaction emphasized that the size of the recirculation bubble influence the motion of the low-frequency mechanism at the separation point. This sensitive separation of the laminar boundary layer could be seen as a great challenge in the intakes of the supersonic/hypersonic airplanes [13].

1.4.2   Characteristics of SWBLI unsteadiness

Several experimental and numerical studies in the past decades have shown the different aspects of the unsteadiness of shock wave boundary layer interactions. It is strongly noted that unsteadiness is an influential aspect of the separated flow. A spacious spectrum of frequencies and large scale motions is the evidence of this phenomenon.

Experimental predictions

Bogdonoff *et. al.* [19] conducted an experimental study for the interaction of a shock wave with a turbulent boundary layer on a flat plate at Mach 2.97. This study reported that the distribution of the static pressure on the wall indicates an upstream influence of about three boundary layer thickness while the overall interaction takes six boundary layer thickness. The investigation of wall pressure fluctuation is carried out by Kistler [87] for the turbulent separated regions ahead of a forward-facing step at Mach 3.40 and 4.54. This study concluded that the pressure fluctuations generate from two specific causes: fluctuation due to the changes in the shape of the separated region and the turbulent free shear layer. To investigate SWBLI unsteadiness in an attached and separated flow, Dolling and Or [47] experimented with two-dimensional compression ramp at Mach 3 and Reynolds number 1.4×10^6. This study emphasized that the shock wave organization is unsteady in both attached and detached flows. Moreover, this unsteady organization of the shock wave emerges in a region where the pressure signal is intermittent. Kussoy *et. al.* [94] examined the shock wave unsteadiness of the interaction between the shock wave and turbulent boundary layer for both the 2D and 3D geometries. It is found in this study 1.16, as the shock wave moves forward, the recirculation zone intends to expand and moves the separation point upward along with the cylinder and the reattachment point downward along with the flare. The recirculation zone contracts as the shock move backward.

Dolling [45] inspected the unsteady mechanism of the shock structure with and without separation in the compression ramp for different ramp angles from $8°$ to $24°$. The range
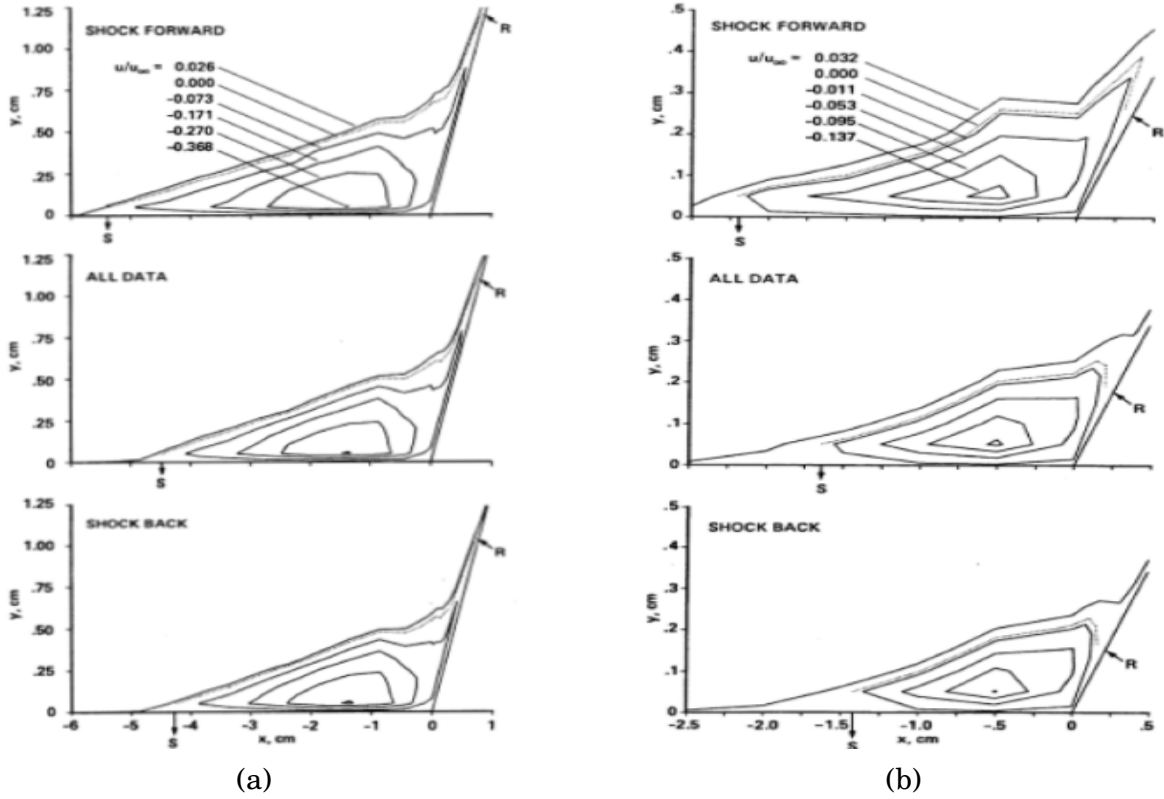
Figure 1.16: The contours of the mean velocity at two different shock angle $23°$ (a) and $5°$ (b). From [94].

and maximum amplitude of unsteady shock oscillations at the wall versus inviscid pressure rise are shown in figure 1.17. This study concluded that both the ratios of maximum turbulent intensity and the maximum amplitude of unsteady shock motion are growing almost linearly with the pressure rise. Moreover, this study clarifies that the turbulence amplification is not intimately linked to the size of the separated region for ramp angles less than $16°$, as no separation occurs at all for ramp angles less than $16°$.

The experiment of Andreopoulos *et. al.* [9] described that the unsteady shock motion causes a large amount of turbulence amplification but the downstream turbulence properties have no direct effect of the unsteady shock motion. Moreover, they found that the maximum turbulence intensity of mass-flux is amplified by a factor of 5 within the boundary layer above that upstream level while the mean mass-flux rose only by a factor of 2. Isocontours of the mass-flux/wall-pressure space-time correlation coefficients for the upstream and downstream boundary layer are shown in figure 1.18. Similar trends are observed in both the upstream and downstream boundary layers.

The upstream influence of the unsteadiness in the interaction environment of the laminar and turbulent flow for a compression corner is shown in figure 1.19 by Dolling and Murphy [46] using the time-averaged wall pressure distribution. It is noticed that the amplitude of fluctuations increased about the mean. Moreover, as the time-averaged wall pressure increases with the wall locations, the whole signal moves above the pres-
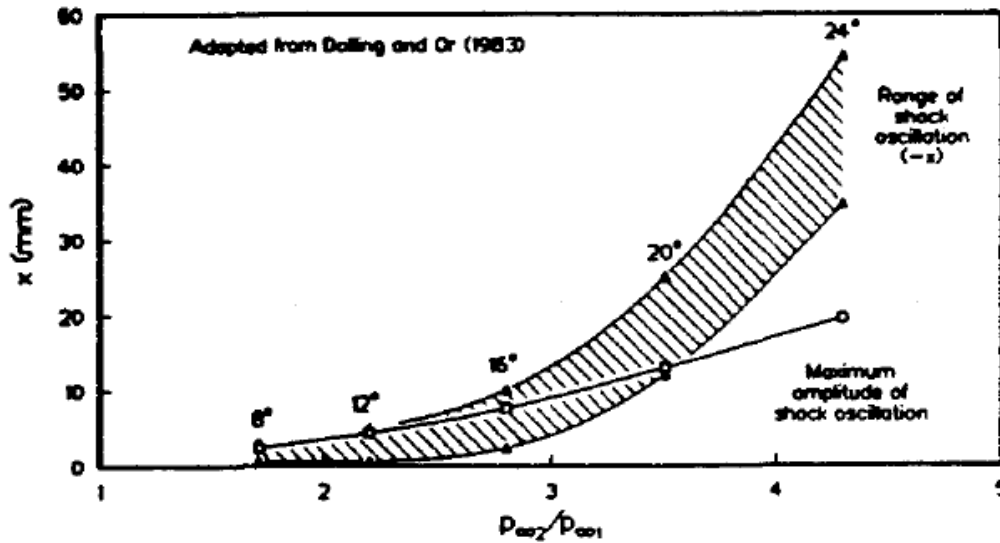
Figure 1.17: Schematic representation of the extent and amplitude of shock oscillations for the five ramp angles of compression corner. From [45].

sure axis. However, a single instant sketch cannot represent the downstream increase in the time-averaged wall pressure, a time history is needed at several locations in the intermittent case.

Plotkin [117] observed that the unsteady motion of a shock wave is directly related to the velocity fluctuations in the upstream boundary layer. Smits and Muck [140] also found the unsteady dynamics of shock in a spectrum of shock oscillation. Also, the studies [140, 56] related to this unsteady motion of the shock wave found no inter-relationship between the shock motion and the velocity fluctuations in the incoming boundary layer. They argued that the high-frequency dynamics of the separation shock is originated by the retaliation of this separation shock to the passage of discrete turbulent structure, although the large scale oscillations of the recirculation bubble possessed the low-frequency motion of the separation shock. The conclusion of their studies created a controversial moment. However, the source of those low-frequency oscillations is not found in their studies. Many of the recent investigations have been committed to finding out the possible source of these low-frequency mechanisms.

McClure [108] experimented with the unsteadiness related to the shock-induced separation of a turbulent boundary layer over a compression ramp at Mach 5. It is noticed that the oscillations in pitot pressure indicate substantial flapping of the separated shear layer. Moreover, the motion of separation shock is not directly associated with the size of the recirculation bubble. It may, although, respond to changes immediately downstream of the separation point. Unalmis and Dolling [155] experimented with a similar setup and found a relationship between the fluctuations of velocity in the spanwise direction and the size of the recirculation region. They also observed that the presence of vortical structures in the upstream boundary layer causes the low-frequency phenomena in the recirculation region. Beresh *et. al.* [15] found a correlation between the motion of the separation shock and the velocity fluctuations, present in the lower part of the upstream
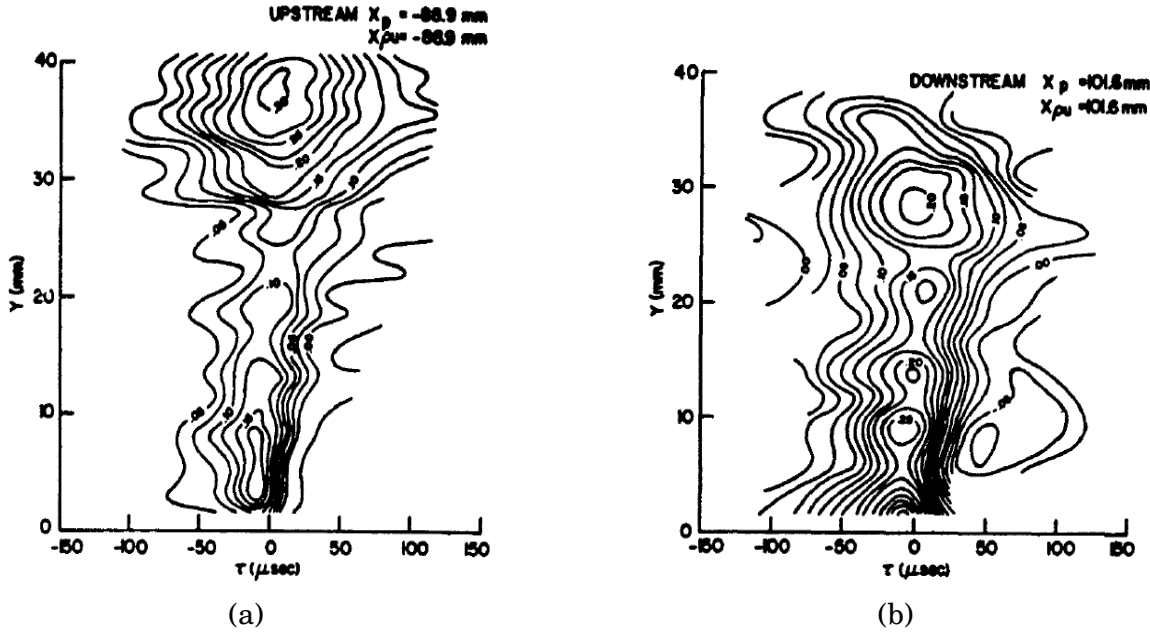
Figure 1.18: Isocontours of mass flux/wall pressure space-time correlation coefficient in upstream (a) and downstream (b). From [9].
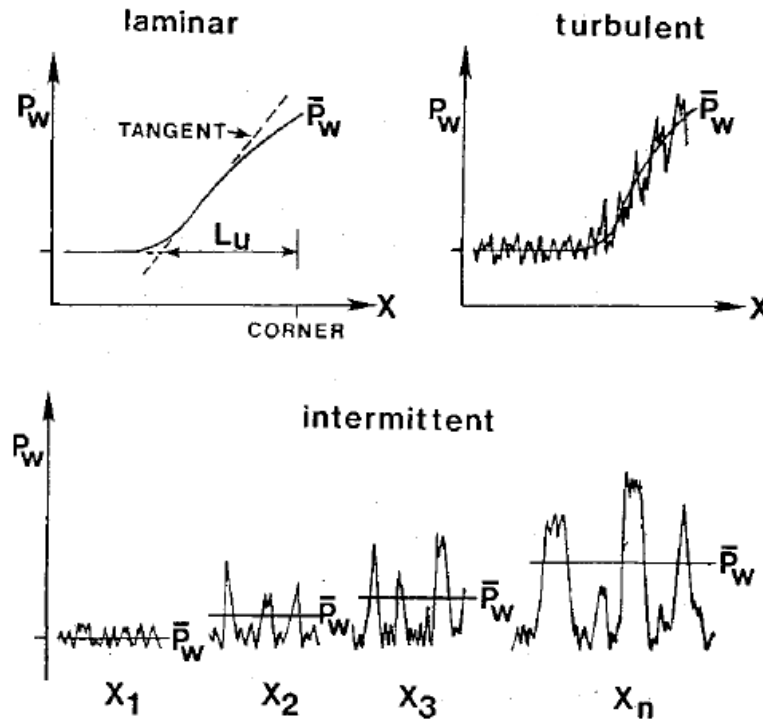
Figure 1.19: A physical interpretation of upstream influence in laminar and turbulent flow. From [46].

boundary layer. Also, a fuller velocity profile is found related to the downstream movement of the separation shock. However, a less fuller velocity profile is found related to the upstream movement of the separation shock. These velocity profiles are shown in

figure 1.20.
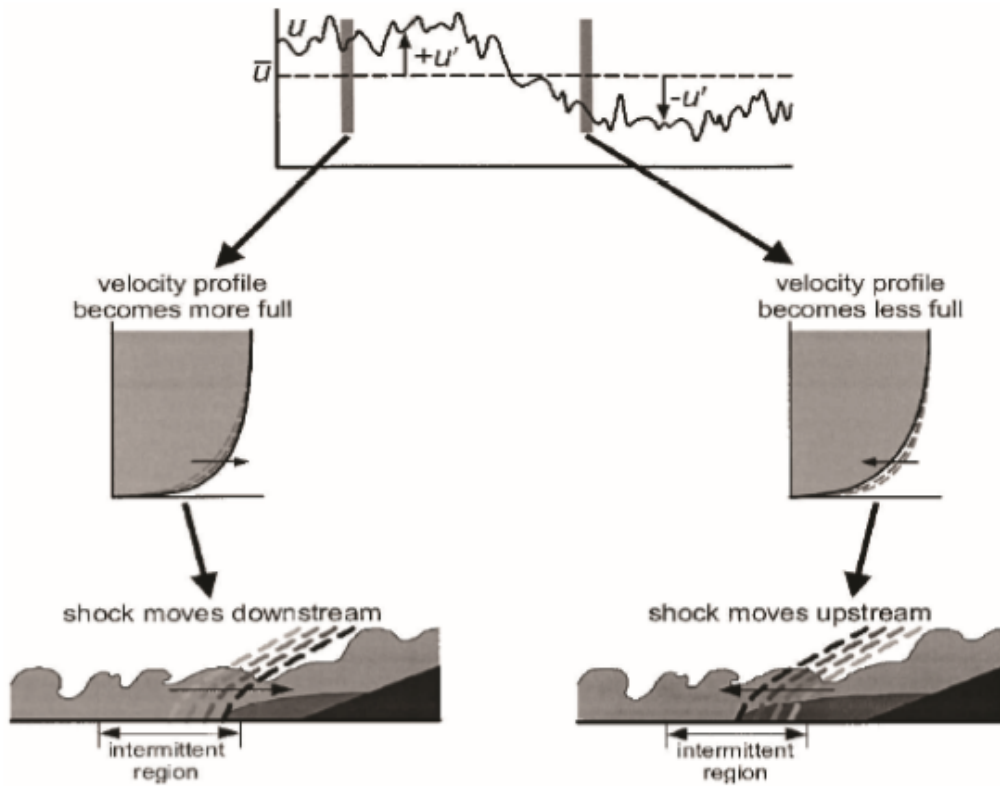
Figure 1.20: The relationship between upstream boundary layer and the extent of the separation zone. From [15].

Similar behaviour is observed by Hou [78] using the PIV (Particle Image Velocimetry) technique over a compression ramp for Mach number 2. He found a correlation between the low-frequency oscillations in the upstream boundary layer thickness and the motion of the separation shock in both the forward and rearward directions. The validation of this phenomenon is also carried out in another study [24] of blunt fin induced turbulent interactions at Mach 2. They noticed that the motion of the separation shock is harmonized according to the oscillations in the upstream boundary layer.

The outcome of the above important studies concluded that the motion of the separation shock is associated with the low-frequency mechanism. The turbulent structure present in the upstream boundary layer is not capable to define the origin of the low-frequency mechanism. Nonetheless, some of the recent important studies noticed that the presence of these turbulent structures in the incoming boundary layer is long enough to decide the low-frequency mechanism. An experimental study carried out by Kim and Adrian [86] for the turbulent boundary layer in the incompressible flow, proposed a model named VLSM (Very Large Scale Motion) to understand the large-scale mechanisms. They found the presence of the broad range of both the low and high speed turbulent strips, created by the hairpin packets and related to the VLSM model, shown in figure 1.21. This study suggested that the model may be a useful tool to understand the flow physics of oscil-

lations of both the separation shock and recirculation region. The experimental studies of Ganapathisubramani *et. al.* [63, 64] validated the above VLSM model by investigating the upstream influence on unsteady mechanism of the shock-induced separation in turbulent flow over a ramp at Mach 2. They found that the low-frequency unsteady mechanism of the shock-induced separation may occur due to the presence of both the low and high speed turbulent structures in the incoming boundary layer.
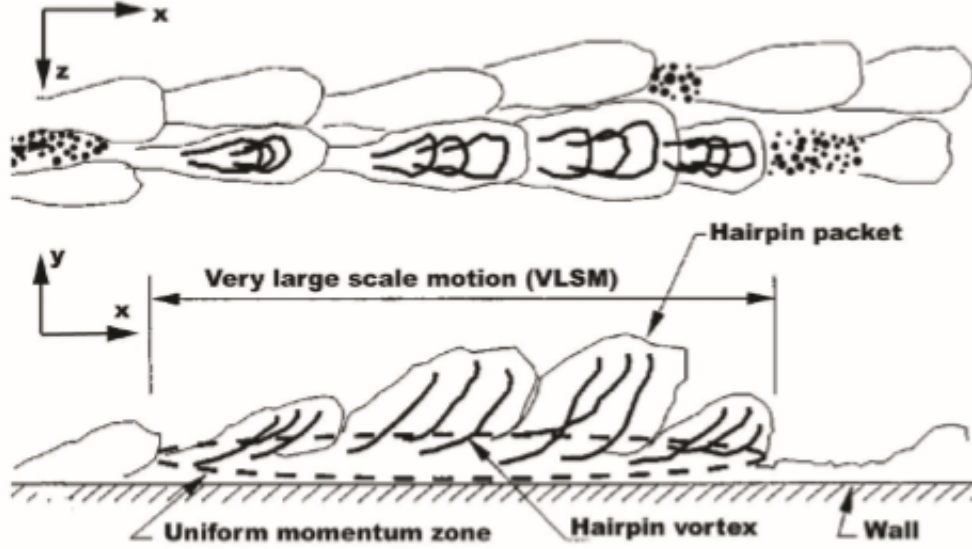
Figure 1.21: A schematic of VLSM (Very Large Scale Motion) model. From [86].

Souverein *et. al.* [142] confirmed the low-frequency dynamics of the reflected shock by investigating both the unsteadiness and temporal dynamics in the interaction between the planner shock and the turbulent boundary layer at Mach 1.69. A detailed experimental analysis [39] of a high Reynolds number ($Re \approx 200 \times 10^3$) shock wave-turbulent flow interaction on a flat panel at Mach 3 is conducted for the low-frequency unsteady dynamics of a large separation bubble. A huge increment in the low-frequency oscillation is observed in both the separation and reattachment regions as well as the excitement of high-frequency is also observed in the separation region.

Numerical predictions

The continuous efforts in developing the more accurate techniques for numerical simulations as well as ongoing advancements in computational power have proved that the CFD (Computational Fluid Dynamics) is a useful tool to analyze the flow physics of complex problems like SWBLI. Hybrid LES-RANS (Large Eddy Simulation/Reynolds Averaged Navier Stokes), LES (Large Eddy Simulation), and DNS (Direct Numerical Simulation) are found as powerful techniques that could tackle such complex problems with a high degree of accuracy. These techniques can help us understand the flow structure of the steady as well as unsteady harmful aspects of the shock wave boundary layer interactions. Some earlier studies [135, 90, 48] found that RANS simulations are not capable to predict the SWBLI unsteadiness which is a very important aspect of this phenomenon.

They noticed that the results obtained from RANS simulations are not in good agreement with the previous experimental studies in the strong interaction case.

The first successful attempt of LES is noticed by Hunt and Nixon [80] for a compression ramp induced shock-boundary layer interaction. Some results of this simulation are found in a good agreement with the experimental results for the frequency dynamics of the separation shock. Another numerical study [106] of the interactions between a normal shock and entropy fluctuations found a correlation between the fluctuations of temperature and velocity in the upstream boundary layer. Moreover, this correlation greatly altered the growth of the turbulence across the shock.

A very narrow recirculation region is investigated by Adams [2] using DNS for the ramp induced turbulent interaction at ramp angle 18° and Mach 3. They found no valid correlation between the fluctuations of temperature-velocity in the incoming boundary layer and the interaction region. Also, a close similarity is noticed between the oscillation frequency of the separation shock and the bursting frequency of the incoming boundary layer. The results of this DNS are also validated by Rizzetta *et. al.* [125] using LES for the same configuration and the ADM model (approximated deconvolution model) employed to the sub-grid scale modeling.

The numerical simulations are carried out by Yan *et. al.* [164, 163] to investigate the ramp induced interaction environment for different ramp angles using LES. However, the results of these simulations are not found in good agreement with the experimental results for the time evolution of the separation system as well as to capture the large scale motion of the separation shock. Garnier *et. al.* [65] carried out LES for the interaction of a shock wave with a turbulent boundary layer. Whereas, the analyzed results for mean and fluctuating velocity in this study are found in a good qualitative agreement with reference experimental data. This is another successful attempt of LES and recognized as a predictive tool for such complex phenomena. The existence of a three-dimensional large scale structure (Görtler-type vortices) is noticed in a numerical study [103] by performing LES for the compression corner induced turbulent interaction at Mach 2.95 and ramp angle 25°. All the results (distribution of wall pressure, skin friction, size of the recirculation region, shock position) of this simulation are found in good agreement with the experimental data. Knight *et. al.* [89] discussed the capabilities and limitations of both LES and DNS and concluded that these highly accurate methods have a strong capacity to capture all harmful aspects of SWBLI.

A numerical study of the shock wave and laminar boundary layer interaction concluded that the unsteadiness emerges from the presence of fluctuations in the recirculation region [20]. Moreover, this study proposed that the low-frequency mechanism may appear in the laminar interactions without the presence of turbulent structures in the upstream boundary layer. They investigated that the complexity occurs in the unsteadiness as the angle of incident shock increases. Also, the organization of interaction passes through the stage where the flow becomes stationary as well as three dimensional but seems unstable, and finally, it may lead to unsteady three-dimensional flow. This analysis is based on Dallman's conjecture [35] which suggested that before the appearance of the

unsteady vortex shedding, various regions of recirculation appear inside the elementary bubble and finally resulted as an overall flow structure change with the structurally unstable saddle to saddle networks. This phenomena is shown in the figure 1.22.
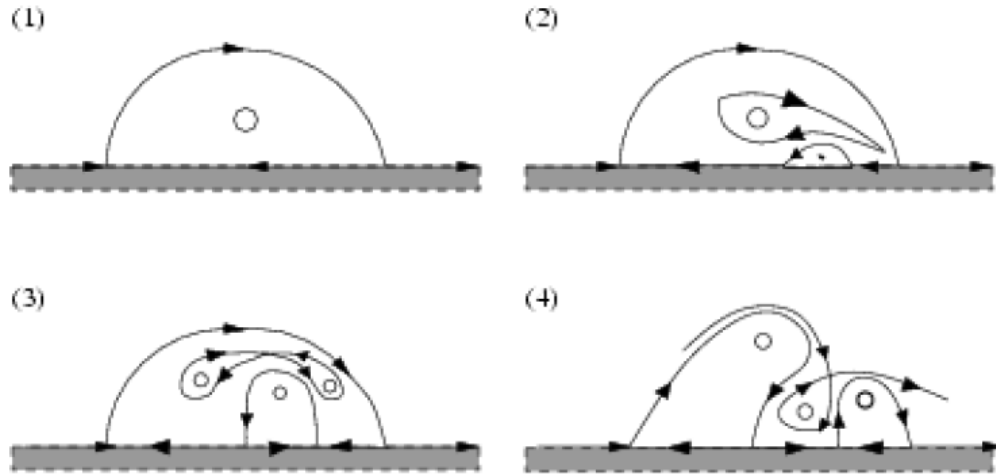
Figure 1.22: The representation of conjecture for topological changes of structure of separation bubble associated with the onset of the shedding of coherent structure. From [35].

To investigate the interaction between the shock wave and the turbulent boundary layer, Wu *et. al.* [161] performed DNS for two configurations: compression ramp and reflected shock case. The results of this simulation are found in good agreement with the experiments for ramp case but have some conflicts with the experimental results for the reflected shock case in the sense of three-dimensional structures and the pressure distribution inside the recirculation bubble.

A study of compressible turbulence for supersonic flows [53] suggested that the low-frequency mechanism in the recirculation region may be a possible source of the unsteady motion of the separation shock. At the same time, Pirozzoli and Grasso [116] performed DNS to investigate the shock wave-turbulent interaction on a flat plate at Mach 2.25. They suggested that the large-scale low-frequency unsteady motion of the separation shock is related to the shedding of the coherent structure in the shear layer close to the average separation point. The pattern of this phenomenon is recorded at different time instants in the 2D plane and shown in figure 1.23. Moreover, the interactions of these coherent structures with the impinging shock generate the acoustic waves. Those waves feed upstream and produce the low-frequency unsteady mechanism in the recirculation bubble as well as flapping motion in the reflected shock.

To analyze the shock wave-turbulent boundary interaction, DNS is performed by Wu and Martin [162] for a compression ramp at Mach 2.9 and ramp angle 24°. It is found that the

low-frequency dynamics of the separation point and shock are correlated with and fall behind the motion of the reattachment point. The breakdown of the recirculation bubble due to the fluid rupture outside the bubble is shown in figure 1.24 for six consecutive time intervals. Also, no variations are found in the mean properties of the upstream boundary layer with both downstream and upstream positions of the shock, suggesting that the low-frequency dynamics of the shock are dominated by the downstream flow.
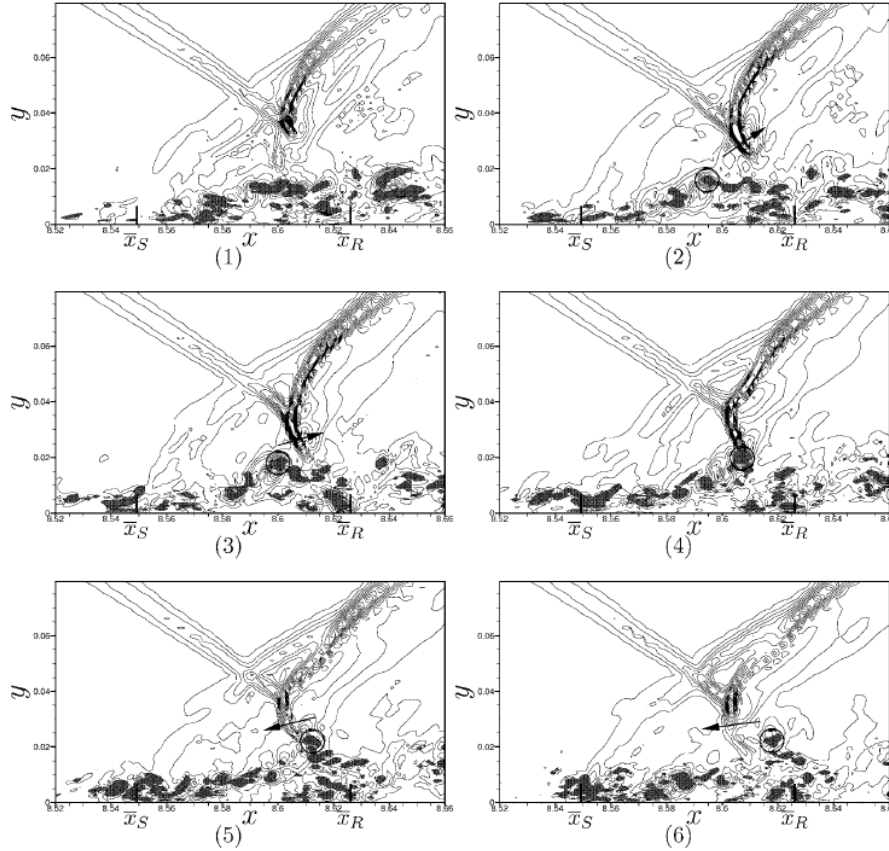
Figure 1.23: 2D instantaneous flow field in sense of the modulus of pressure gradient and the vortical structure shown by gray color patches. The instantaneous motion of the shock foot shown by arrow and the circle represents the specific vortex. From [116].
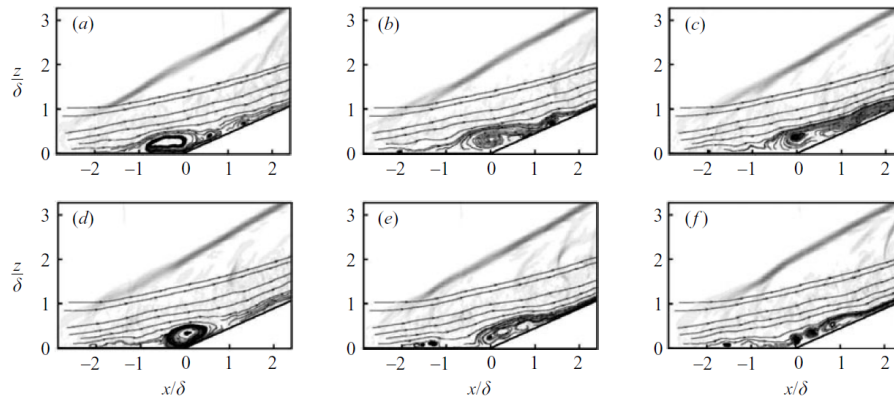
Figure 1.24: The breakdown of the recirculation bubble represented by using stream line and the location of the shock shown by contours of pressure gradient. From [162].

Touber and Sandham [154] conducted several simulations, using LES, to investigate the low-frequency unsteadiness for the interaction between oblique shock and turbulent boundary layer on a flat plate at Mach 2.3. In this study, the analyzed results for the low-frequency unsteady dynamics of the separation shock are found in good agreement with the experimental data. It is also noticed that a hardly separated flow has the same unsteady trend in the separation shock.

To investigate the origin of the low-frequency oscillations, Hadjadj [70] performed LES for the interaction between a shock wave and a turbulent boundary layer on a flat plate at Mach 2.28. He observed in this study that the reflected shock oscillates at low-frequencies and those frequencies are present within the separation bubble. These results highly attributed a hypothesis that the low-frequency dynamics of the coupled system (shock and separation bubble) generated the unsteady dynamics of the reflected shock.

The unsteadiness of a shock reflection on a turbulent boundary layer is investigated by Agostini *et. al.* [3] at Mach 2.3 using the data of LES. Different cases ranging from weak to strong separation are simulated in this study. It is noticed that the low-frequency unsteady dynamics of the shock are linked to the low-frequency motion of the mixing-layer developed downstream of the incident shock. Also, the medium-frequency of the shock is linked to the shedding of the large coherent structure in the mixing layer.

Priebe and Martin [120] performed DNS to analyze the low-frequency unsteadiness in the compression ramp induced shock-turbulent interaction at the ramp angle of $24°$ and Mach 2.9. They found that the flapping of the shear layer leads to the low-frequency oscillations of the recirculation bubble. Also, the intensity of the turbulence (active turbulent structures) fluctuation in the shear layer depends on the low-frequency dynamics of the separation bubble. Figure 1.25 shows that the low intensities of the turbulence correspond to the shrinkage in the recirculation bubble (both the upper and lower lefts) and the high intensities correspond to the expansion in the recirculation bubble (both the upper and lower rights). The results of this study are further validated in other numerical studies [99, 100] by performing LES on the same flow configuration. The presence of the turbulent structures as well as the shock wave is shown in figure 1.26 for the same flow configuration.

A computational analysis is performed by Aubard *et. al.* [11] to investigate the low-frequency dynamics in the environment of shock-turbulent boundary layer interaction using LES. It is observed that the low-frequency oscillations in the separation bubble are linked to the forward and backward movement of the separation shock. However, the medium-frequency of oscillation is found related to the shedding of the large coherent structure in the mixing layer.

Grilli *et. al.* [68] performed LES to examine the interaction between the compression-expansion ramp and turbulent boundary layer at Mach 2.88 and ramp angle $25°$. This investigation indicated the presence of the streamwise Görtler-type vortices in the flow field. Those vortices are emanated from the heart of the separation zone downstream of the compression corner and travel along the wall of the ramp. Also, those vortices die out when interacting with the Prandtl-Meyer expansion waves originated at the expansion
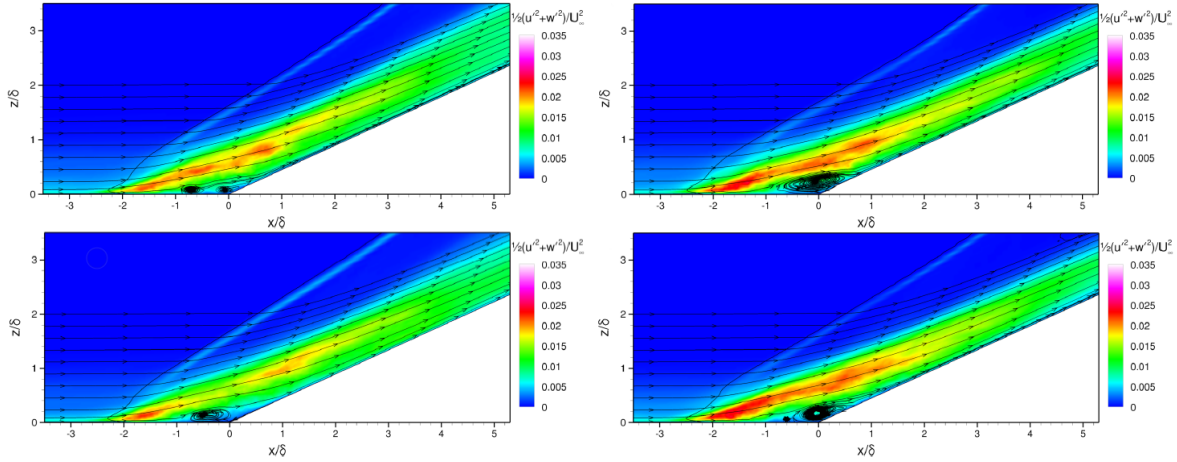
Figure 1.25: Spanwise-averaged low-pass filtered flow fields at the instants. In-plane turbulent kinetic energy is calculated using high-pass filtered fluctuations of the velocity. From [120].
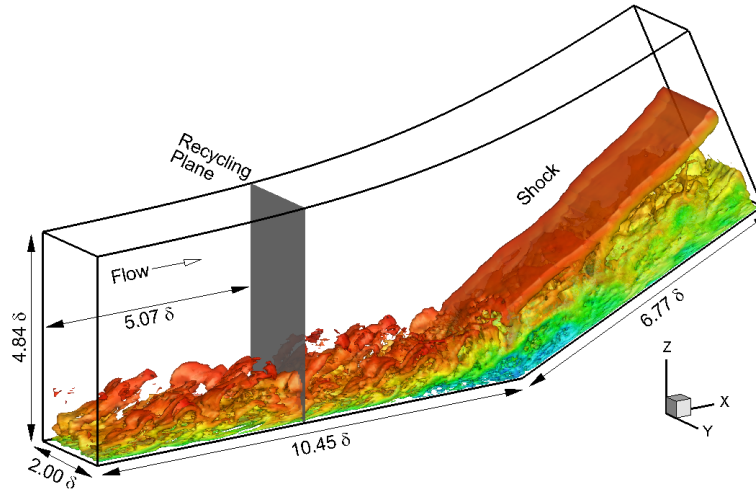
Figure 1.26: Instantaneous flow field in a computational domain by using isosurface of density gradient. From [99]

corner. The instantaneous flow field is found similar to another experimental study 1.27. The incoming boundary layer (point 1) is disturbed by the separation shock (point 2). A region of the reverse flow (point 3) as well as a free shear layer (point 4) appeared due to the interaction. The shocklets (point 5) travel with this separated shear layer as well as the recompression in the reattachment region generates the unsteady lambda shock structure (point 6).

To investigate the low-frequency unsteadiness in a flat plate induced shock-laminar boundary layer interaction, DNS is performed by Sansica *et. al.* [131] for two different forced steady scenarios (small and large recirculation bubble) at Mach 1.5. The low-frequency dynamics for both the scenarios are shown in figure 1.28. It is noticed that the low-frequency dynamics grow at a lower frequency for the small separation (upper left) than the low-frequency dynamics of the large separation (upper right). This trend indicates that the laminar boundary layer responsible for the downstream shedding of the coherent
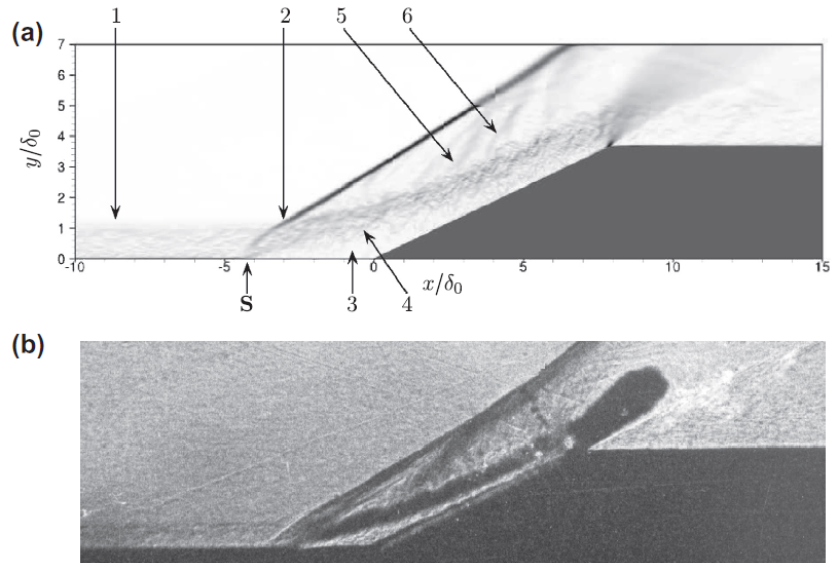
Figure 1.27: Instantaneous flow field. Numerically computed using spanwise gradient of density (a) and experimental schlieren visualization (b). From [68].

structure in various frequency ranges depends on the separation size. Also, the reaction of the low-frequency dynamics of the small separation influence both the upstream and internal forcing (upper left and lower left) while the large separation influence the internal forcing linearly (lower right). The feedback of the large separation to upstream forcing at the separation point increases quadratically with high energy (lower right). A strong dependent compromise is found again by Clemens and Narayanaswamy [32] between the fluctuations in the upstream boundary and size of the separation. It is observed that the influence of the fluctuations in the incoming boundary layer is reduced with the increasing size of the separation region.

Larchevêque [95] performed LES to investigate the low-frequency unsteady dynamics of the shock wave-boundary layer interaction with separation in transitional flow. Also, the low-frequency motions of the recirculation bubble are not found directly linked to the fluctuations in the incoming boundary layer. It is shown in figure 1.29 that the transiently growing recirculation bubble brings some similarity of the stationary bubble with low-frequency dynamics as far as the oblique mode with medium frequency is concerned.

Fournier *et. al.* [59] performed DNS for both the 2D and 3D flat plate induced shock wave-laminar boundary layer interaction at Mach 2.23 and shock angle $33.1°$. They found that the streamwise oscillations are recovered for the reflected shock in the 2D case whereas no oscillations of the shock are recovered for the 3D case. In the 3D case, they found the upstream movement of the reflected shock but no clear frequency appeared. Moreover, an interesting phenomenon is observed for the 3D case that some vorticity-free regions due to the non-uniformity of the vortex shedding downstream of the reattachment point increase the three-dimensionality of the flow. To analyze the low-frequency unsteadiness of the shock wave-turbulent interaction with the mean flow separation, Pasquariello *et. al.* [113] performed LES at Mach 3. The analyzed results of this study hold the theory that the low-frequency unsteadiness is conducted by the inherent structure of the interaction region in which Görtler-type vortices could be noticed as continuous forcing for
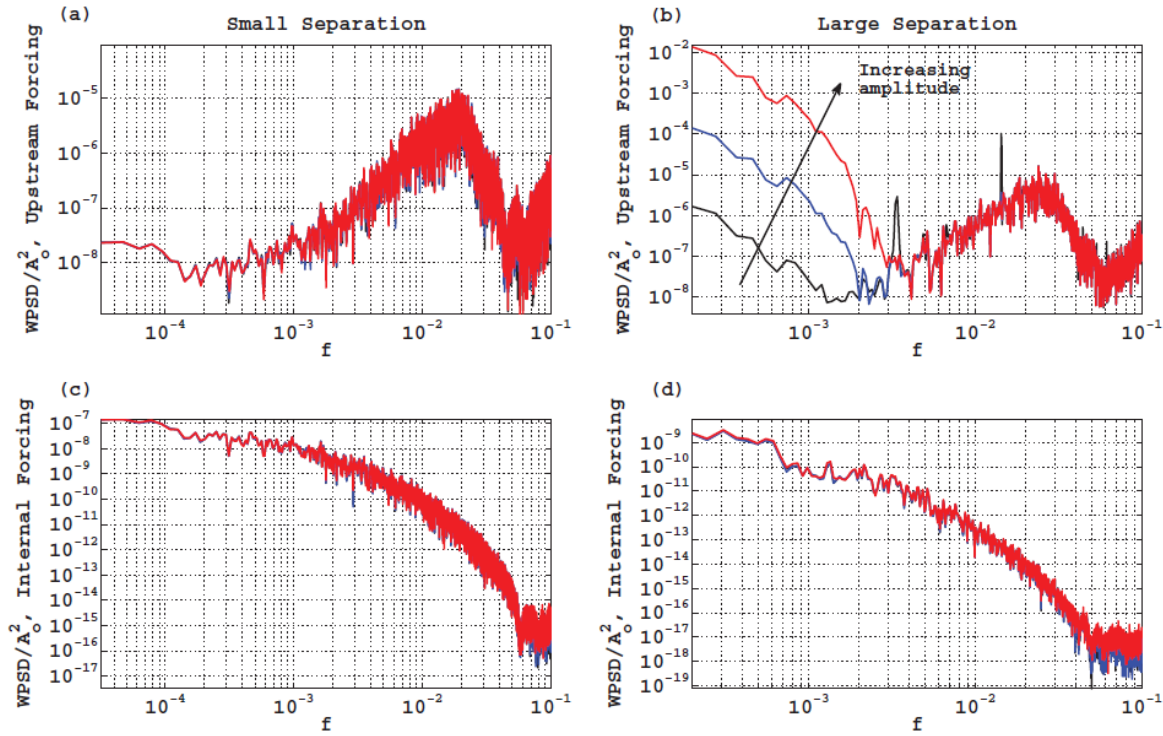
Figure 1.28: Analysis of the low-frequency dynamics by linearity test: Weighted PSDs normalized by forcing amplitude square at the separation point in response to upstream forcing (a,b) and internal forcing (c,d). From [131].

strong interactions.

An Implicit Large Eddy Simulation (ILES) is performed by Vyas *et. al.* [157] to understand the dynamic character of the interaction region based on the budget of the turbulent kinetic energy. As the flow approaches the interaction region, the production term magnifies. The isosurface of the production term at three different levels is shown in figure 1.30. The massive rate of production is found around both the mean incident and reflected shock while the drop in the rate is found rapidly away from the shock. Also, the strong magnitude of the production term is noticed in the interaction region, however, it started to moderate in the reattachment region.

To investigate the optimal spatial growth of Görtler type vortices, Dwivedi *et. al.* [54] performed DNS simulation for the different shock angles in a flat plate induced laminar interaction at Mach 5.92. In this simulation, it is observed that a steady three-dimensional flow field appeared for strong interactions which indicated the existence of the streamwise Görtler type structures that are periodic in the spanwise direction. After analyzing those streamwise Görtler vortices, it is found that some structures are more energetic than others. The growth of these Görtler type structures appeared near the reattachment region as well as further downstream of the same region.

To understand the effects of the unsteadiness, DNS is performed by Khotyanovsky and Kudryavtsev [85] for the flat plate induced transitional interaction at Mach 2. It is observed that the flow oscillations in the interaction region induced by the large scale tur-

(a) Low frequency unsteadiness

(b) Oblique modes
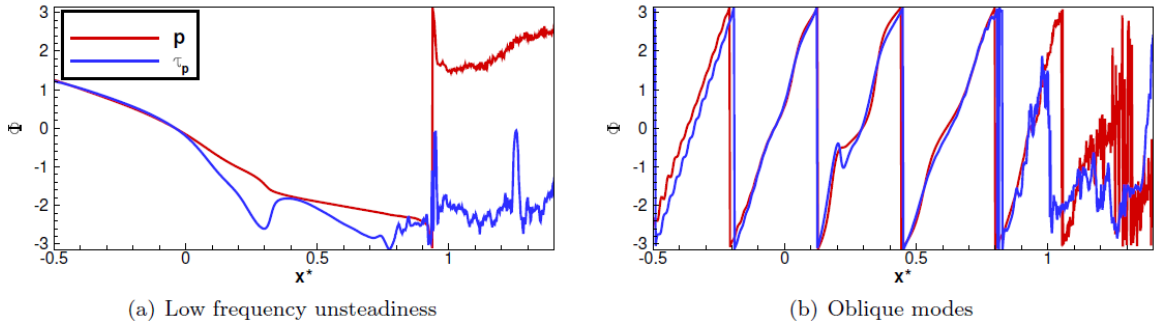
Figure 1.29: The streamwise evolution of the phase for the wall pressure and skin friction with respect to the separation point. From [95].
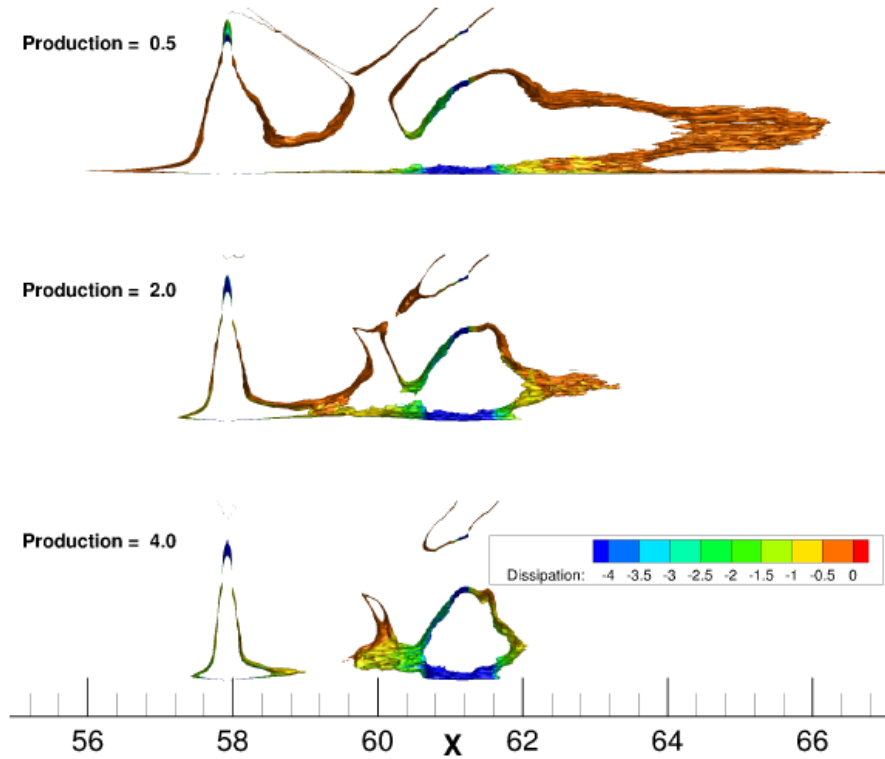
Figure 1.30: Isosurface of the production term at three different levels and colored by the dissipation. From [157].

bulent structure appeared in the transitional boundary layer. Also, those oscillations revealed the unsteady mechanism of impinging and reflected shock in the recirculation region. The three-dimensional unsteady dynamics of the separated flow is shown in figure 1.31.

Poggie *et. al.* [118] investigated the global flow structure and unsteady dynamics in a highly confined ramp induced interaction at Mach 2.25 and ramp angle of 24°. A symbolic discrepancy is observed in the flow field structure when the results of this simulation with confining sidewalls compared to the symmetric or periodic boundary conditions at the lateral boundaries of the domain. By using conditional averages and spatial correlations, the large scale symmetric as well as asymmetric dynamics of the recirculation regions
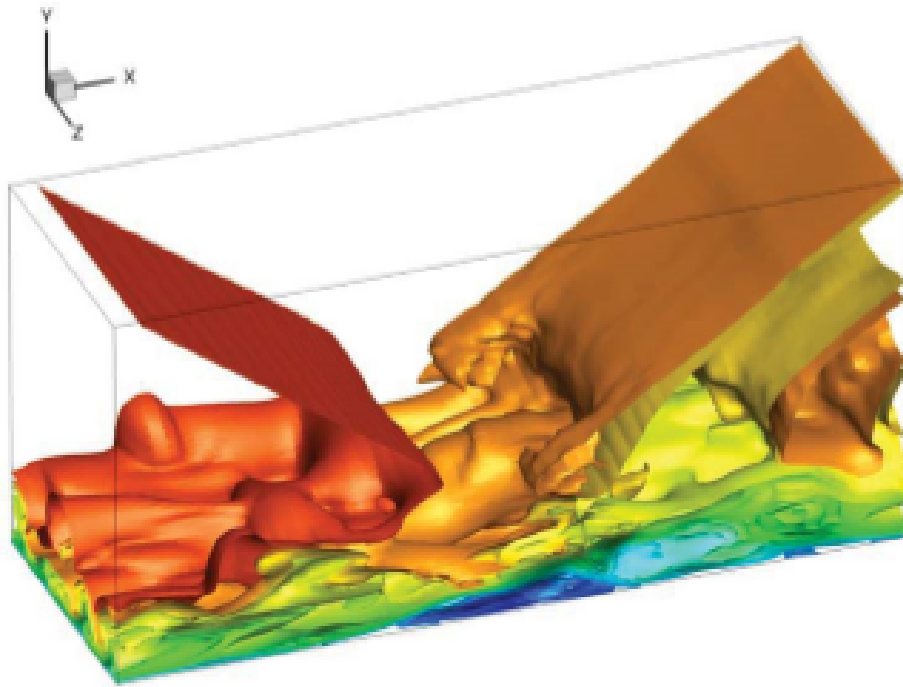
Figure 1.31: Isosurface of instantaneous streamwise velocity in the interaction region. From [85].

are observed in the instantaneous flow field. Also, the mean and unsteady flow is highly influenced by the presence of sidewalls.

1.5 High-order numerical methods for compressible flows

In the literature of numerical schemes, most of the developed numerical integrations can be split into two categories, the first one is combined Spatio-temporal methods and the second one is the methods based on the separate Spatio-temporal discretization. Over the past few decades, more sophisticated methods have emerged with superior impact retention properties that solve some of the problems with classical schemes.

Method of lines

The method of lines is the classical approach to obtain high-order numerical methods. This approach mainly concerns separate Spatio-temporal methods. The majority of the separate Spatio-temporal methods are based on multi-level, high-order Runge-Kutta (RK) time discretization. At each time step, high-order spatial sampling is used which sometimes involves a restriction procedure in the flow calculations to prevent spurious oscillations. Although more work [138] and [137] on individual space-time methods is still ongoing, a family of ENO/WENO is a very well known classical shock-capturing approach for spatial discretization. The global stencil is larger for these separate Spatio-temporal

scheme since spatial sampling is applied to each sub-step of temporal discretization. It is shown that these approaches are very accurate in smooth regions, they are well-recorded shock waves but behave too diffusive near contact discontinuities. Various studies are conducted to obtain more accurate forecasts using numerical techniques based on WENO family [2, 148, 107, 161, 116, 120, 70, 157]. However, these methods are very expensive in terms of computational cost.

One-Step (OS) schemes

In contrast to the separate Spatio-temporal schemes, combined Spatio-temporal schemes are typically developed using the Lax-Wendroff approach. Such schemes have a minimum global stencil and optimal non-oscillating conditions based on restrictions on the preservation of monotonicity that could be easily realized. These accurate numerical schemes offer a compromise between high precision in smooth areas and efficient shock-capturing technique. These one-step monotonicity preserving schemes provide accurate results that can be well compared with classical high-order separate space-time schemes at a lower cost [36]. One-step (OS) schemes are developed first for one-dimensional scalar equations (linear and nonlinear) and then for a multidimensional system of nonlinear equations [148]. Various numerical studies [127, 60, 14] are performed to obtain more accurate results by using these one-step schemes for the high-speed aerospace applications.

Shock-capturing techniques

Conventional shock approaches include a monotonic upstream centered scheme for conservation laws (MUSCL) and total variation diminishing (TVD). Over the past two decades, more sophisticated techniques have emerged with superior impact detection. These techniques have features that solve some of the traditional scheme problems. Whatever the method (separate or combined), to avoid spurious oscillations near strong gradient areas, a special limiting method should be used. To capture the sharp discontinuities without any oscillation, TVD schemes generally considered suitable. However, it is known that TVD constraint clips the extrema in strong gradient areas that appear to be a serious flaw in the limiting process. To avoid excessive accuracy loss, the monotonicity preserving (MP) criteria, introduced by Suresh and Hunyh [146] which extend the TVD intervals so that the numerical flux could maintain a certain value, must be met. In particular, to generalize the MP conditions considering the flux limitations, the initial restrictions of MP Suresh and Hunyh [146] are rewritten in the TVD structure without CFL limitations. The MP conditions that maintain accuracy can be expressed directly as limiting function [36]. The MP constraints are written for each characteristic field and can also be found in [36]. It is also important to note that the main difference is that the MP restrictions apply to non-monotonic data and TVD for monotonic data, so the scheme does not oscillate around the discontinuities. Another popular classical shock-capturing technique is an ENO/WENO family of schemes. One of the computational studies [76] first presented this ENO method which is well-known classified higher order numerical method for convection dominated problems. The key advantage of these schemes is their ability to attain promptly high order accuracy in smooth regions while preserving stable, non-oscillating, and sharp discontinuities. Therefore, these schemes are especially

useful for tasks that contain both strong discontinuity and complex structures of smooth solutions but very expensive in computational cost. A study [148] has made a possible comparison between TVD, MUSCL, ENO, and the old version of a weighted essentially non-oscillating scheme (WENO). It is noticed in this study that the TVD scheme adds a large amount of diffusion by using the Van-Leer harmonic limiter. Also, the MUSCL scheme led to abnormal results including induced low-frequency oscillations downstream of the shock. However, a better agreement with the reference results is achieved using the ENO/WENO family of schemes. The best impact resolution characteristics are obtained using a 5th order WENO formulation.

A recent review [22] of high-order shock-capturing methods was motivated by the need to address the unstable rocket launch flow. The purpose of the review is to recover the actual 2nd order-MUSCL scheme in the Launch ascent and Vehicle Aerodynamics (LAVA) finite-difference code with a present-day substitute. A comparison between the Central-AD (central finite differencing with artificial dissipation), LAD (localized artificial diffusivity), and WENO (weighted essential non-oscillatory) schemes are made in this study. The 6th-order Central-AD is found to be the cheapest numerical method compared to the existing MUSCL scheme with better spectral resolution. Although, at low cost, Central-AD worked poorly compared to the other approaches but allowed good spectral resolution for turbulent flows and proved to be a feasible option for flows that contain weak shocks. However, its performance against strong shocks is rated as poorly observed fluctuations; both Central-AD and LAD are inferior to more reliable WENO systems. Shock-capturing methods lead to excessive loss of numerical dissipation, accomplishing them observed to be a destitute choice to deal with small-scale structures in transient and fully turbulent flows. To obtain analogous resolution as the non-dissipative scheme, substantial fine meshes are required. Those fine meshes are not practical for DNS and severely limit the scope of the problem that could be solved.

Different numerical approaches for complex (SWBLI) simulations

Most of the computational studies [116, 154, 120, 11, 131] in the literature of shock wave boundary layer interactions, based on DNS/LES simulations, used different numerical approaches (method of lines). Those studies are listed below:

- In a numerical study of Adams [2], he used a 5th-order hybrid compact finite-difference ENO scheme for the spatial discretization of the convective fluxes and 6th-order central compact finite difference for the diffusive fluxes. The 3rd-order Runge-Kutta scheme is used for the time integration.

- In a computational study of Pirozzoli and Grasso [116], the 7th-order finite difference WENO scheme is used for the discretization of convective fluxes. The viscous fluxes are discretized by the 4th-order compact finite difference scheme. The 4th-order explicit Runge-Kutta scheme is used for the time integration.

- In the numerical study of Touber and Sandham [154], they discretized the convective fluxes by using a 5th-order WENO scheme combined with a centered 4th-order scheme, via a selective Ducros's sensor. A centered 4th-order accurate scheme is

used for viscous fluxes. The 3rd-order explicit Runge-Kutta scheme is used for the temporal discretization.

- In a numerical study of Stephan and Martin [120], the inviscid fluxes are discretized by the 4th-order WENO scheme and the viscous fluxes are discretized by using standard 4th-order central differences. The temporal discretization is performed by the 3rd-order low-storage Runge-Kutta scheme.

- In a computational study of Sansica *et. al.* [131], the 4th-order central differencing scheme is used to discretize the internal points of the computational domain. A 4th-order boundary scheme is performed for boundary points. An entropy-splitting approach is also used to improve numerical stability. To capture discontinuities (shocks) accurately with the high-order central scheme, a total variation diminishing (TVD) scheme is combined with an artificial compression method. A 3rd-order low-storage Runge-Kutta schemes are used to perform the temporal discretization.

1.6   Conclusions

We carried out an overview of the previous studies obtainable in the literature of the shock wave-boundary layer interactions. We discussed several important aspects of SWBLI in different geometrical configurations. The center of our attention is specially dedicated to the low-frequency unsteady mechanism of SWBLI. It is discussed in section 1.4.2 that no studies have made any clear explanation of the physical mechanism promoting the low-frequency unsteadiness in the whole SWBLI system. The source of low-frequency oscillations is still not completely understood, but there are two strong premises which indicate that either it could be due to the random structures in the incoming boundary layer or to the shedding of coherent structures (vortices) in the mixing/shear layer downstream of the separation point. We also discussed different numerical approaches to solve the governing equations in the compressible flow and specially the SWBLI phenomenon.

Chapter 2

Numerical Methods

Contents

2.1 The governing equations in cartesian coordinates

The Navier-Stokes equations, resulting from the application to a fluid domain of the three fundamental principles of mechanics, namely the conservation of mass, momentum, and energy, can be written in their conservative form as [152]:

$$\frac{\partial \mathbf{U}}{\partial t} + \nabla.\mathbf{F_c} - \nabla.\mathbf{F_v} = \mathbf{0} \tag{2.1}$$

where U, the vector of conservative variables, $\mathbf{F_c}$, the convective fluxes, and $\mathbf{F_v}$, the diffusive fluxes are defined by:

$$\mathbf{U} = \begin{bmatrix} \rho \\ \rho\mathbf{u} \\ \rho E \end{bmatrix}$$

$$\mathbf{F_c} = \begin{bmatrix} \rho\mathbf{u} \\ \rho\mathbf{u} \otimes \mathbf{u} + p\mathbb{I} \\ (\rho E + p)\mathbf{u} \end{bmatrix} \tag{2.2}$$

$$\mathbf{F_v} = \begin{bmatrix} 0 \\ \mathbf{\Pi} \\ \mathbf{u}.\mathbf{\Pi} + \lambda\nabla T \end{bmatrix}$$

ρ, $\mathbf{u}$, E, p and T are the density, velocity vector, total energy per unit mass, thermodynamic pressure, and temperature respectively. The fluid considered in the present study has been supposed to verify the ideal gas hypothesis. As a consequence, the ideal gas equation of state, defined by $p = \rho r T$, r being the specific gas constant, as well as the definition of the total energy per unit mass $E = c_v T + \frac{1}{2}\mathbf{u}.\mathbf{u}$, with c_v the heat capacity at constant volume, have been introduced to close the system of equations.

The viscous stress tensor $\mathbf{\Pi}$ is expressed, by invoking Stokes' hypothesis, as:

$$\mathbf{\Pi} = \mu(\nabla\mathbf{u} + \nabla^T\mathbf{u}) - \frac{2}{3}\mu\nabla.\mathbf{u} \tag{2.3}$$

The dynamic viscosity μ is supposed to depend only upon the temperature through Sutherland's law [147]:

$$\mu(T) = \mu_{ref}\left(\frac{T}{T_{ref}}\right)^{3/2}\frac{T_{ref} + S}{T + S} \tag{2.4}$$

with $\mu_{ref} = 1.716 \times 10^{-5}\ Pa.s$, $T_{ref} = 273.15\ K$ and $S = 110.4\ K$.

The Prandtl number Pr being specified as a parameter since the fluid is chosen, the temperature-dependant thermal conductivity λ can then deduced from the equation $\lambda = \frac{\mu C_p}{Pr}$.

2.2   Extension to curvilinear coordinates

In this section, a generalized coordinate transformation of the governing equations in conservative form is implemented. When one wants to study the flow around a complex geometry such as a compression ramp, one must solve the Navier-Stokes equations in the real physical domain $P = P(x, y, z)$. However, for numerical reasons mainly linked to the discretization order, it is more efficient to solve those equations in a cartesian computational domain $C = C(\xi, \eta, \zeta)$. Consequently, all the derivatives in P must be expressed as a combination of their computational counterparts in C.

In general, and even if the resolution is more complicated, it is easier to define the *inverse* C-to-P transformation that writes:

$$x = x(\xi, \eta, \zeta, t) \tag{2.5}$$
$$y = y(\xi, \eta, \zeta, t) \tag{2.6}$$
$$z = z(\xi, \eta, \zeta, t) \tag{2.7}$$

rather than the *direct P-to-C* transformation leading to a more straightforward resolution.

Using the the chain rule of differential calculus on 2.5, 2.6 and 2.7, the partial derivatives in the computational domain can be related to their equivalents in the physical domain by:

$$\frac{\partial}{\partial \xi} = \left(\frac{\partial}{\partial x}\right)\left(\frac{\partial x}{\partial \xi}\right) + \left(\frac{\partial}{\partial y}\right)\left(\frac{\partial y}{\partial \xi}\right) + \left(\frac{\partial}{\partial z}\right)\left(\frac{\partial z}{\partial \xi}\right) \tag{2.8}$$

$$\frac{\partial}{\partial \eta} = \left(\frac{\partial}{\partial x}\right)\left(\frac{\partial x}{\partial \eta}\right) + \left(\frac{\partial}{\partial y}\right)\left(\frac{\partial y}{\partial \eta}\right) + \left(\frac{\partial}{\partial z}\right)\left(\frac{\partial z}{\partial \eta}\right) \tag{2.9}$$

$$\frac{\partial}{\partial \zeta} = \left(\frac{\partial}{\partial x}\right)\left(\frac{\partial x}{\partial \zeta}\right) + \left(\frac{\partial}{\partial y}\right)\left(\frac{\partial y}{\partial \eta}\right) + \left(\frac{\partial}{\partial z}\right)\left(\frac{\partial z}{\partial \zeta}\right) \tag{2.10}$$

Or, in matrix notations:

$$\begin{bmatrix} \frac{\partial}{\partial \xi} \\ \frac{\partial}{\partial \eta} \\ \frac{\partial}{\partial \zeta} \end{bmatrix} = \begin{bmatrix} \frac{\partial x}{\partial \xi} & \frac{\partial y}{\partial \xi} & \frac{\partial z}{\partial \xi} \\ \frac{\partial x}{\partial \eta} & \frac{\partial y}{\partial \eta} & \frac{\partial z}{\partial \eta} \\ \frac{\partial x}{\partial \zeta} & \frac{\partial y}{\partial \zeta} & \frac{\partial z}{\partial \zeta} \end{bmatrix} \begin{bmatrix} \frac{\partial}{\partial x} \\ \frac{\partial}{\partial y} \\ \frac{\partial}{\partial z} \end{bmatrix} \tag{2.11}$$

It is then possible to solve system 2.11 for $\frac{\partial}{\partial x}$, $\frac{\partial}{\partial y}$ and $\frac{\partial}{\partial z}$ using Cramer's rule. The derivatives in the P domain are then expressed as:

$$\frac{\partial}{\partial x} = \frac{1}{J}\left[+\frac{\partial}{\partial \xi}\left(\frac{\partial y}{\partial \eta}\frac{\partial z}{\partial \zeta} - \frac{\partial z}{\partial \eta}\frac{\partial y}{\partial \zeta}\right) - \frac{\partial}{\partial \eta}\left(\frac{\partial y}{\partial \xi}\frac{\partial z}{\partial \zeta} - \frac{\partial z}{\partial \xi}\frac{\partial y}{\partial \zeta}\right) + \frac{\partial}{\partial \zeta}\left(\frac{\partial y}{\partial \xi}\frac{\partial z}{\partial \eta} - \frac{\partial z}{\partial \xi}\frac{\partial y}{\partial \eta}\right)\right] \tag{2.12}$$

$$\frac{\partial}{\partial y} = \frac{1}{J}\left[-\frac{\partial}{\partial \xi}\left(\frac{\partial x}{\partial \eta}\frac{\partial z}{\partial \zeta} - \frac{\partial z}{\partial \eta}\frac{\partial x}{\partial \zeta}\right) + \frac{\partial}{\partial \eta}\left(\frac{\partial x}{\partial \xi}\frac{\partial z}{\partial \zeta} - \frac{\partial z}{\partial \xi}\frac{\partial x}{\partial \zeta}\right) - \frac{\partial}{\partial \zeta}\left(\frac{\partial x}{\partial \xi}\frac{\partial z}{\partial \eta} - \frac{\partial z}{\partial \xi}\frac{\partial x}{\partial \eta}\right)\right] \tag{2.13}$$

$$\frac{\partial}{\partial z} = \frac{1}{J}\left[+\frac{\partial}{\partial \xi}\left(\frac{\partial x}{\partial \eta}\frac{\partial y}{\partial \zeta} - \frac{\partial y}{\partial \eta}\frac{\partial x}{\partial \zeta}\right) - \frac{\partial}{\partial \eta}\left(\frac{\partial x}{\partial \xi}\frac{\partial y}{\partial \zeta} - \frac{\partial y}{\partial \xi}\frac{\partial x}{\partial \zeta}\right) + \frac{\partial}{\partial \zeta}\left(\frac{\partial x}{\partial \xi}\frac{\partial y}{\partial \eta} + \frac{\partial y}{\partial \xi}\frac{\partial x}{\partial \eta}\right)\right] \tag{2.14}$$

where J is called the *Jacobian* of the transformation and is defined by:

$$J = \frac{\partial(x, y, z)}{\partial(\xi, \eta, \zeta)} = \begin{vmatrix} \frac{\partial x}{\partial \xi} & \frac{\partial y}{\partial \xi} & \frac{\partial z}{\partial \xi} \\ \frac{\partial x}{\partial \eta} & \frac{\partial y}{\partial \eta} & \frac{\partial z}{\partial \eta} \\ \frac{\partial x}{\partial \zeta} & \frac{\partial y}{\partial \zeta} & \frac{\partial z}{\partial \zeta} \end{vmatrix} \tag{2.15}$$

It physically represents the ratio of the volume in the physical plane to that of the computational space. The derivatives $\frac{\partial \xi}{\partial x}, \frac{\partial \eta}{\partial x}, \frac{\partial \zeta}{\partial x}, \frac{\partial \xi}{\partial y}, \frac{\partial \eta}{\partial y}, \frac{\partial \zeta}{\partial y}, \frac{\partial \xi}{\partial z}, \frac{\partial \eta}{\partial z}$, and $\frac{\partial \zeta}{\partial z}$ are known as the *metrics* of the transformation and represent the ratio of arc lengths in the computational plane to that of the physical plane.

Inserting Eq. 2.12 to 2.15 into the Navier-Stokes equations (Eq. 2.1), it is possible to write them into their strong conservative form, in the curvilinear coordinates system (See [6], for instance):

$$\frac{\partial \hat{\mathbf{U}}}{\partial t} + \nabla.\hat{\mathbf{F}}_{\mathbf{c}} - \nabla.\hat{\mathbf{F}}_{\mathbf{v}} = 0 \tag{2.16}$$

where

$$\hat{\mathbf{U}} = J\mathbf{U}$$

$$\hat{\mathbf{F}}^{(\xi)} = \mathbf{F}^{(\mathbf{x})}\left(\frac{\partial y}{\partial \eta}\frac{\partial z}{\partial \zeta} - \frac{\partial z}{\partial \eta}\frac{\partial y}{\partial \zeta}\right) - \mathbf{F}^{(\mathbf{y})}\left(\frac{\partial x}{\partial \eta}\frac{\partial z}{\partial \zeta} - \frac{\partial z}{\partial \eta}\frac{\partial x}{\partial \zeta}\right) + \mathbf{F}^{(\mathbf{z})}\left(\frac{\partial x}{\partial \eta}\frac{\partial y}{\partial \zeta} - \frac{\partial y}{\partial \eta}\frac{\partial x}{\partial \zeta}\right)$$

$$\hat{\mathbf{F}}^{(\eta)} = \mathbf{F}^{(\mathbf{x})}\left(\frac{\partial z}{\partial \xi}\frac{\partial y}{\partial \zeta} - \frac{\partial y}{\partial \xi}\frac{\partial z}{\partial \zeta}\right) - \mathbf{F}^{(\mathbf{y})}\left(\frac{\partial z}{\partial \xi}\frac{\partial x}{\partial \zeta} - \frac{\partial x}{\partial \xi}\frac{\partial z}{\partial \zeta}\right) + \mathbf{F}^{(\mathbf{z})}\left(\frac{\partial y}{\partial \xi}\frac{\partial x}{\partial \zeta} - \frac{\partial x}{\partial \xi}\frac{\partial y}{\partial \zeta}\right) \quad (2.17)$$

$$\hat{\mathbf{F}}^{(\zeta)} = \mathbf{F}^{(\mathbf{x})}\left(\frac{\partial y}{\partial \xi}\frac{\partial z}{\partial \eta} - \frac{\partial z}{\partial \xi}\frac{\partial y}{\partial \eta}\right) - \mathbf{F}^{(\mathbf{y})}\left(\frac{\partial x}{\partial \xi}\frac{\partial z}{\partial \eta} - \frac{\partial z}{\partial \xi}\frac{\partial x}{\partial \eta}\right) + \mathbf{F}^{(\mathbf{z})}\left(\frac{\partial x}{\partial \xi}\frac{\partial y}{\partial \eta} - \frac{\partial y}{\partial \xi}\frac{\partial x}{\partial \eta}\right)$$

In those equations, $\hat{\mathbf{U}}$ and $\hat{\mathbf{F}} = \hat{\mathbf{F}}_{\mathbf{c}} + \hat{\mathbf{F}}_{\mathbf{v}}$ are the vector of conservative variables and the fluxes in curvilinear coordinates, respectively. The superscripts $^{(x)}$, $^{(y)}$, $^{(z)}$, $^{(\xi)}$, $^{(\eta)}$ and $^{(\zeta)}$ represent the components of the fluxes.

In a more practical point of view, each metrics is computed using a 2^d-order scheme.

2.3 Numerical methodology

In order to simulate the supersonic flow of interest in this Ph.D., around A high-order finite volume approach has been used to solve the Navier-Stokes equations (2.1 to 2.3). The resolution is split into an inviscid Euler part and a viscous part, through an operator splitting procedure. The One-Step Monotonicity Preserving (OSMP) scheme is used for the discretization of the Euler part. This scheme, developed by Daru and Tenaud [37], is based upon the Lax-Wendroff approach and ensure the same order of accuracy in both time and space in the regular regions. In all the present study, a 7th order scheme, denoted as OSMP7 has been used. As far as the diffusive part is concerned, a combination between a classical centered 2nd-order scheme and 2nd-order Runge-Kutta time integration has been used. It is noteworthy than increasing the approximation order of the viscous terms does not significantly improve the solution [14].

In this part, the OSMP7 scheme will be presented. For the sake of simplicity, the main discussion will be held for a 1D case. The extension to the 3D case, with its peculiarity, will then be presented. In order not to over-complicate the equations, the hatted $\hat{F}$ notation will be dropped but the reader has to be reminded that the fluxes considered here are those described in equations 2.17.

In one dimension, the Euler equations write:

$$\frac{\partial \mathbf{U}}{\partial t} + \frac{\partial \mathbf{F}_{\mathbf{c}}}{\partial x} = \mathbf{0} \qquad (2.18)$$

that becomes, once discretized:

$$\mathbf{U}_i^{n+1} = \mathbf{U}_i^n - \frac{\Delta t}{\Delta x}\left(\mathbf{F}_{c_{i+1/2}}^n - \mathbf{F}_{c_{i-1/2}}^n\right) \qquad (2.19)$$

$\mathbf{U}_i^{n+1}$ is the value of U at time $n\Delta t$ and position $i\Delta x$, Δt and Δx being the time step and cell size respectively.

A 7th-order One-Step scheme (OS7) is then used to approximate the convective flux $\mathbf{F}^n_{c_{i+1/2}}$ [37]:

$$\mathbf{F}^n_{c_{i+1/2}} = \mathbf{F}^{Roe}_{i+1/2} + \frac{1}{2} \sum_{k=1}^{3} \left(\Phi^7_k (1 - |\nu_k|) \, \delta\alpha_k \, |\lambda_k| \, .\mathbf{r}_k \right)_{i+1/2} \tag{2.20}$$

In this equation, Φ^7_k are the accuracy function that ensures the 7th-order of the scheme. $\delta\alpha_k$ is the kth Riemann invariant while λ_k and $\mathbf{r}_k$ are the eigenvalues and right eigenvectors of the Roe-averaged Jacobian matrix $\dfrac{\partial \mathbf{F}}{\partial \mathbf{U}}$, respectively. ν_k is defined as $\nu_k = \frac{\Delta t}{\Delta x}\lambda_k$. Finally, $\mathbf{F}^{Roe}_{i+1/2}$, the first-order Roe flux at the cell interface, is such that:

$$\mathbf{F}^{Roe}_{i+1/2} = \frac{1}{2}\left(\mathbf{F}^n_{c_i} + \mathbf{F}^n_{c_{i+1}}\right) - \frac{1}{2}\sum_{k}\left(|\lambda_k|\,\delta\alpha_k.\mathbf{r}_k\right)_{i+1/2}$$

Following the Lax-Wendroff procedure, the 7th-order accuracy functions $\Phi^7_{k_{i+1/2}}$ are split into even, expressed by a centred scheme, and odd contributions, using upwind approximations. This then reads:

$$\Phi^7_{k_{i+1/2}} = \sum_{n=1}^{3} \Psi^{2n}_{k_{i+1/2}} - js \sum_{n=1}^{3} \Psi^{2n+1}_{k_{i+1/2-js/2}} \tag{2.21}$$

with $js = sign(\lambda_{k_{i+1/2}})$ and where the Ψ functions are computed by:

$$\Psi^{2n}_{k_{i+1/2}} = \sum_{l=0}^{2n-2} (-1)^l C^l_{2n-2}.\left(c_k^{(2n)}\delta\alpha_k\right)_{i+1/2+n-1-l}, \tag{2.22}$$

$$\Psi^{2n+1}_{k_{i+1/2-js/2}} = \sum_{l=0}^{2n-1} (-1)^l C^l_{2n-1}.\left(c_k^{(2n+1)}\delta\alpha_k\right)_{i+1/2+(n-1-l).js} \tag{2.23}$$

In the previous formula, $C^l_r = \dfrac{r!}{(r-l)!\,l!}$ and $c_k^{(q)}$ are coefficients that depends upon the local CFL number through:

$$\left(c_k^{(q+1)}\right)_{i+1/2} = \frac{|\nu_k|_{j+1/2} + (-1)^q \lfloor \frac{(q+1)}{2} \rfloor}{q+1}.\left(c_k^{(q)}\right)_{i+1/2}, \quad q \geq 2$$

One of the drawbacks of using high-order numerical schemes is the appearance of spurious oscillations in the vicinity of discontinuities (shock). One solution to tackle this problem is to use Total Variation Diminishing (TVD) constraints [75]. However, this approach is known for clipping the solution's extrema. Monotonicity-Preserving (MP) constraints [146] must then be applied on the accuracy functions Φ in order to loosen the TVD constraints close to extrema.

In order to limit the problems appearing when one wants to the extent a coupled time and space scheme such as OSMP to the 2D and 3D cases, a Strang directional splitting [144] is used. The main drawback of this strategy is that it is only second-order accurate when directional operators do not commute. However, and even if the order of accuracy is lowered compared to the tensorial multistage approach, the combination OSMP scheme-Strang splitting has been shown to gives accurate results with very small error level at low cost [37, 38].

2.4   Computational domain and boundary conditions

The computational domain for the current study of three-dimensional interaction be-
tween a shock wave and the laminar boundary layer in both configurations (compression
and compression-expansion ramp) is shown in figures 2.1 and 2.2 respectively. All bound-
ary conditions imposed at the corresponding boundary surface are also represented.
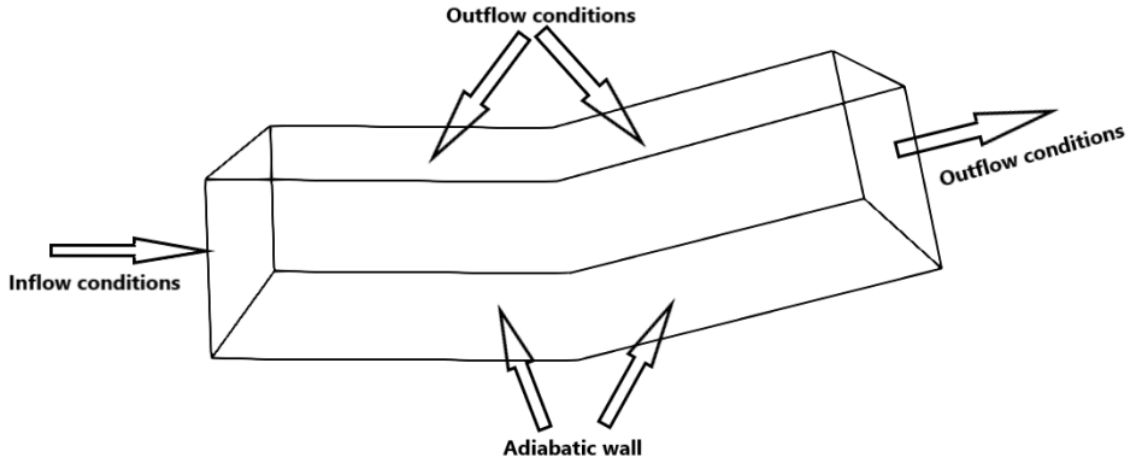
Figure 2.1: Computational domain and boundary conditions for the simulation of com-
pression ramp.
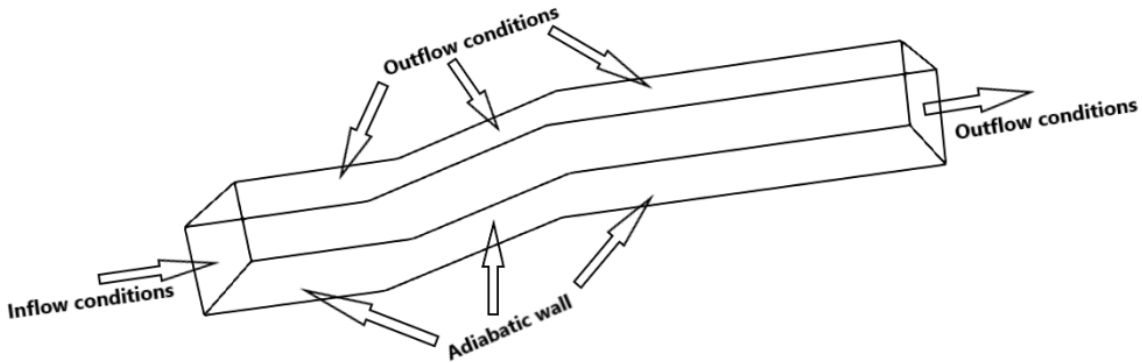
Figure 2.2:   Computational domain and boundary conditions for the simulation of
compression-expansion ramp.

In both configurations, inflow conditions are applied on the leftmost boundary, adiabatic
(insulated) solid walls are considered on the lower boundary and outflow conditions are
imposed on the upper and rightmost boundaries. All those boundary conditions will be
explained in the following parts.

2.4.1 Inlet and outlet conditions

Both inlet and outlet conditions are based on Thompson's method [151], that consists in solving, for each direction, a 1D wave equation defined by:

$$\frac{\partial U_i}{\partial t} + \lambda_i \frac{\partial U_i}{\partial x} = 0 \tag{2.24}$$

where U_i is known as the ith Riemann invariant associated to the characteristic velocity λ_i corresponding to the eigenvalue of the Jacobi matrix of the Euler fluxes in the x direction. According to the type (inlet or outlet) of conditions and the direction (sign) of λ_i, four cases can be encountered:

Inlet condition and incoming wave $(\lambda_i \geq 0)$: the value of the characteristic fields is imposed.

Inlet condition and outgoing wave $(\lambda_i < 0)$: the derivatives of U_i are computed by using a second-order upwind scheme.

Outlet condition and incoming wave $(\lambda_i < 0)$: In order to prevent the wave from coming into the domain, their speed is cancelled, leading to the resolution of the equation $\frac{\partial U_i}{\partial t} = 0$

Outlet condition and outgoing wave $(\lambda_i \geq 0)$: the derivatives of U_i are computed by using a second-order upwind scheme.

2.4.2 Adiabatic walls and no-slip conditions

With respect to the solid walls (lower boundary), no-slip and adiabatic wall conditions have been imposed. The no-slip conditions is obtained using:

$$u_{wall} = v_{wall} = w_{wall} = 0 \tag{2.25}$$

The equation used to compute the density at the wall is obtained by combining the continuity equation and eq. 2.25. It reads:

$$\frac{\partial \rho}{\partial t} = - \left(\frac{\partial \rho w}{\partial z} \right)_{wall} \tag{2.26}$$

It is solved by approximating the wall derivatives with a 4th-order forward finite-difference scheme.

The adiabatic condition is obtained by cancelling the heat flux at the wall, leading to:

$$\left(\frac{\partial T}{\partial z} \right)_{wall} = 0 \tag{2.27}$$

The temperature at the wall is then prescribed by solving equation 2.27, also discretized by a 4th-order forward finite-difference scheme.

2.5 Grid generation

In the present study, and more particularly in Chapter 3, several meshes have been considered in order to test CHORUS in complex geometries. All non-classical meshes will be presented in this part. In each case, the computational domain $C(\xi, \eta, \zeta)$ is a parallelepiped of dimensions $L_{x_{max}} \times L_{y_{max}} \times L_{z_{max}}$ and is transformed into the physical domain $P(x, y, z)$ through the use of inverse relations $x = x(\xi, \eta, \zeta)$. Because of the transformations uses, the number of Control-Volumes (cells in 2D case) in each direction is such that $n_x = n_\xi$, $n_y = n_\eta$ and $n_z = n_\zeta$. As a consequence, and for the sack of simplicity, indexes will be denoted as i, j and k either in the computational or the physical plane.

2.5.1 Hyperbolic Tangent Distorted Mesh

The first mesh to be considered has the peculiarity to have a parallelepiped outline. Only the interior CVs or cells are affected by the transformation, that reads:

$$\begin{cases} x(i, j, k) & = \xi(i) \\ y(i, j, k) & = \eta(j) \\ z(i, j, k) & = \frac{L_{z_{max}}}{2} \left[1 + \frac{\tanh\left[r(i)\left(\frac{\zeta(k)}{L_{z_{max}}} - 0.5 \right) \right]}{\tanh\left(\frac{r(i)}{2} \right)} \right] \end{cases} \tag{2.28}$$

$r(i)$ is the ξ-depending stretching coefficient, defined:

$$r(i) = DP \cos\left(\frac{2\pi\xi(i)}{Lx_{max}} \right) \tag{2.29}$$

with DP the amplitude of the deformation.

In the present study, the distortion have only been applied to the z direction, as shown by the $x(i, j, k) = \xi(i)$ and $y(i, j, k) = \eta(j)$ equations, but it could be easily transposed a full 3D-distortion by modifying those lines. An example of a Hyperbolic Tangent Distorted Mesh, obtained by applying eq. 2.28 to a square regular cartesian mesh with $DP = 4$ is shown in Figure 2.3.
Another advantage of this mesh is that even for large deformation amplitudes, the cells stay rather orthogonal in most of the domain.

2.5.2 Sine-Distorted Mesh

A second mesh has been tested that does not conserve the parallelepiped aspect of the computational domain. On the contrary, the outline has a sine-based boundary. For the Vortex-Convection test case (section 3.1), the distortion has been only applied in the x direction, through:

$$\begin{cases} x(i, j, k) & = \xi(i) + A \sin\left(\frac{2\pi\zeta(k)}{L_{z_{max}}} \right) \\ y(i, j, k) & = \eta(j) \\ z(i, j, k) & = \zeta(k) \end{cases} \tag{2.30}$$
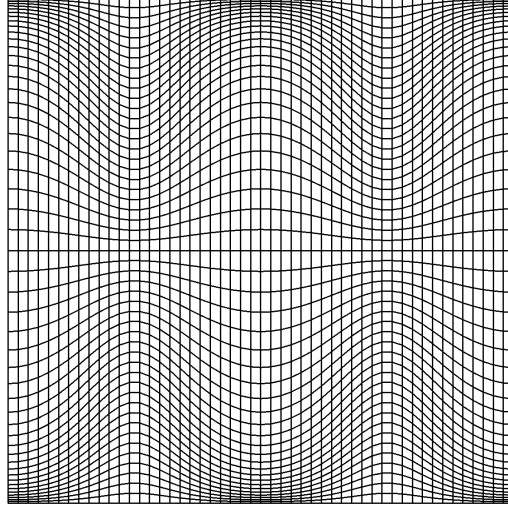
Figure 2.3: Example of a Hyperbolic Tangent Distorted Mesh with $DP = 4$.
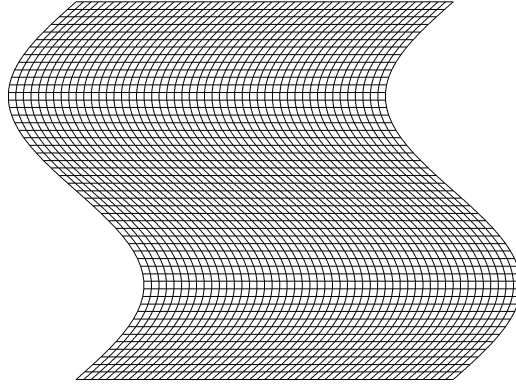
Figure 2.4: Example of a 2D-Sine-Distorted Mesh with $A = 0.18$.

with A the amplitude of the deformation. An example of a 2D-Sine-Distorted Mesh with $A = 0.18$ is represented in Figure 2.4.

For the 3D TGV case, the deformation is applied in every direction such that:

$$
\begin{cases}
x(i,j,k) &= \xi(i) + A\sin\left(\frac{2\pi\zeta(k)}{L_{z_{max}}}\right) \\
y(i,j,k) &= \eta(j) + A\sin\left(\frac{2\pi\xi(i)}{L_{x_{max}}}\right) \\
z(i,j,k) &= \zeta(k) + A\sin\left(\frac{2\pi\eta(j)}{L_{y_{max}}}\right)
\end{cases}
\tag{2.31}
$$

An example of a 3D-Sine-Distorted Mesh with $A = 0.18$ is represented in Figure 2.4. It is noteworthy that, between the 2D and the 3D cases presented here, the computational domain differs. It is a 1×1 square in 2D while it is a $(2\pi)^3$ cube in 3D. As a consequence, the deformation, that is directly related to the size of the computational domain, is weaker in 3D even if the same amplitude $A = 0.18$ is used.
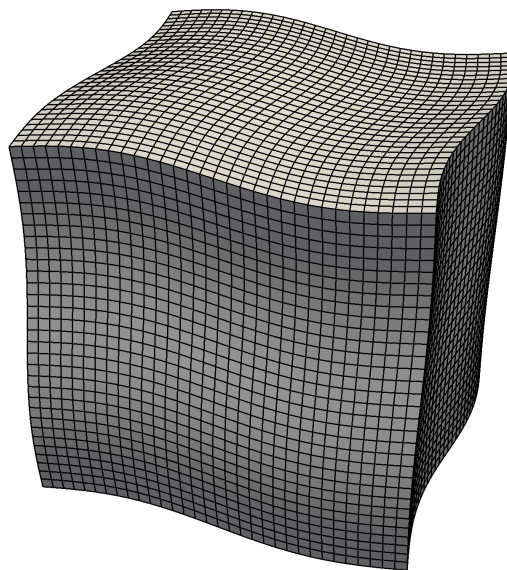
Figure 2.5: Example of a 3D-Sine-Distorted Mesh with $A = 0.18$.

Chapter 3

Numerical analysis of canonical flows on distorted meshes

Contents

Introduction

In this chapter, the influence of the mesh distortion will be analysed for several test-cases. Every case has been selected for their own peculiarities (Advection-diffusion case, turbulence, presence of a shock . . .) and because reference data are available. Those data will be used to assess the performance of the scheme for the distorted mesh. For each test-case, a mesh convergence study has first been performed and several types and/or amplitudes of distortion, described in detail in section 2.5, have been tested.

3.1 Convection of a vortex

The first test-case to be considered is the well-known example of the convection of a vortex. The goal here is to quantify the diffusive and dispersive errors created by the mesh distortion. In this section, the flow configuration and all the reference data are taken from [148].

3.1.1 Flow configuration

In a uniform flow at $Ma = 0.8$ and $Re = 10^4$, a Taylor vortex is initially centred in a square domain of dimensions $[0,1] \times [0,1]$ at $(x_0, y_0) = (0.5, 0.5)$. The vortex is defined by imposing a tangential velocity u_θ given by:

$$u_\theta(r) = C_1 r \ e^{-C_2 r^2}$$

where $r = \sqrt{(x - x_0)^2 + (y - y_0)^2}$ is the distance from the vortex centre. C_1 and C_2 are two constants defining the size of the viscous core. In order to have a core radius of 0.5, these constants are chosen such that $C_1 = 6.595$ and $C_2 = 88.89$. The tangential velocity is then projected onto the (ξ, η) system of curvilinear coordinates (See section 2.2).

From a numerical point of view, the time step is chosen such that $CFL < 0.5$ and periodic boundary conditions are applied in both directions. As a consequence, the uniform flow will convect the vortex towards the right of the domain and the periodic conditions will take it back to the left. The flow conditions ($U_\infty = 1.$) and geometry ($L = 1.$) have been chosen so that the time needed for the vortex to come back to its initial position is $t = 1$. The total simulations have been run for a dimensionless time $t = 5$, corresponding to five periods.

3.1.2 Mesh Convergence

Before considering the influence of the distortion, a mesh convergence study has been performed. Three uniform cartesian meshes have been considered ranging from $2,500$ cells to $40,000$ cells. The mesh parameters are gathered in Table 3.1.

Mesh Name	# of cells	Δt
M_1	50×50	$2 \ 10^{-3}$
M_2	100×100	10^{-3}
M_3	200×200	$5 \ 10^{-4}$

Table 3.1: Mesh parameters used for the vortex convection test-case.

The streamwise evolution of the pressure and vertical velocity are represented in Figures 3.1 and 3.2, respectively. From M_2, the results are in very good agreement with the reference values for both quantities. The differences with respect to the reference values, computed and compiled in Table 3.2, show that the error is very small (smaller than 0.19%) even for the coarsest mesh. In a will to conjugate performance and CPU time

(and to fit the meshes used in the reference paper) the study about the influence of the mesh distortion will then be performed with meshes containing the same number of Cells as M_3.
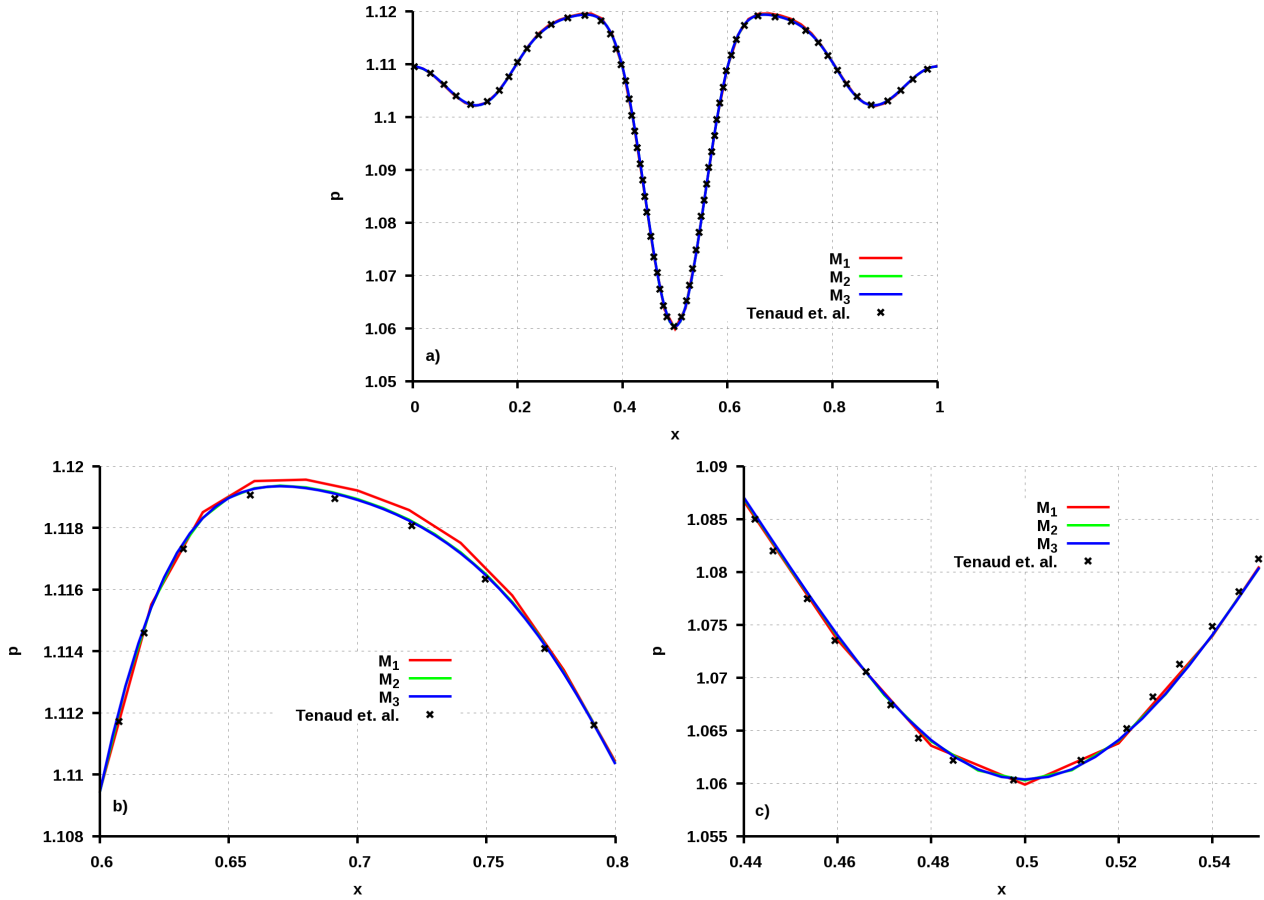
Figure 3.1: Streamwise evolution of the pressure at $y = 0.5$ and $t = 5$ for three different meshes. a: Whole domain; b: Zoom on p_{max}; c: Zoom on p_{min}.

3.1.3 Influence of Distortion

Two kinds of distorted mesh have been used in this study. The first type is the hyperbolic tangent-distorted mesh (HTD). It has the peculiarity to only modify the interior cells of the domain, the boundaries remaining unchanged. The second one is the so-called sine-distorted mesh (SD), which yields a deformation on both the boundary of the domain and the interior cells. A significant difference between those two deformations is that the cells stay quasi-orthogonal almost everywhere with the hyperbolic tangent whereas most of them are skewed when using the sine-distortion. Finally, in order to be resolution independent, the same number of cells ($200 \times 200 = 40{,}000$) has been used for each simulation.
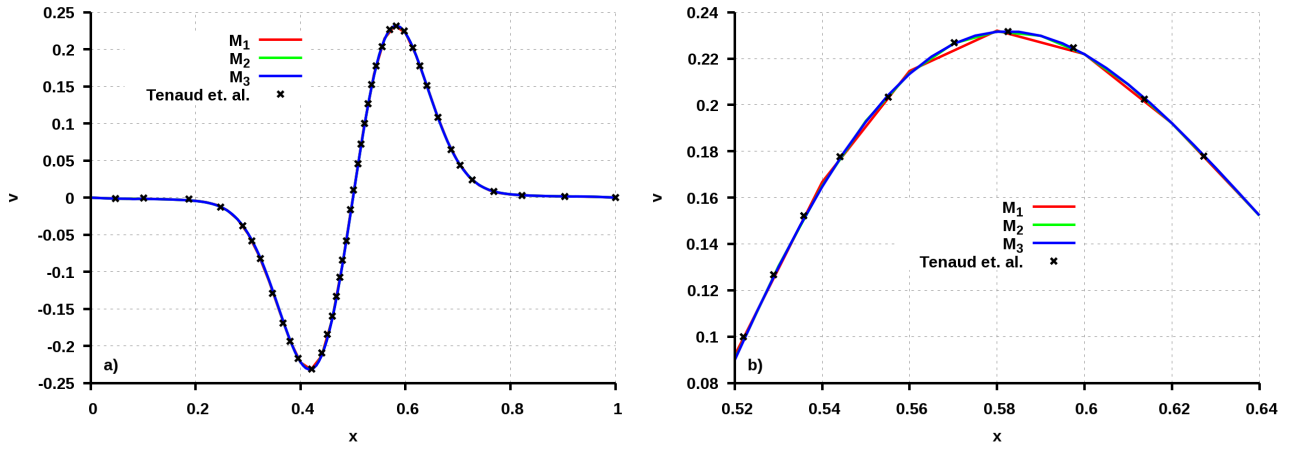
Figure 3.2: Streamwise evolution of the vertical velocity at $y = 0.5$ and $t = 5$ for three different meshes. a: Whole domain; b: Zoom on v_{max}.

Case	p_{min}		v_{max}	
	Value	Error %	Value	Error %
Tenaud *et. al.* [148]	1.06052	-	0.23163	-
M_1	1.05987	0.06	0.23206	0.19
M_2	1.06027	0.02	0.23170	0.03
M_3	1.06036	0.01	0.23160	0.01

Table 3.2: Errors on the minimum pressure and maximum vertical velocity with respect to the reference values at $t = 5$, for three different cartesian meshes.

3.1.3.1   Hyperbolic tangent-distorted mesh

The HTD meshes used in this part have been created using Eq. 2.28. Several deformation parameters have been chosen, ranging from $DP = 0.5$ to $DP = 4$, but only the results for $DP = 1.0$, $DP = 1.5$ and $DP = 2.0$ will be presented here. The subsequent meshes can be found in Figure 3.3.
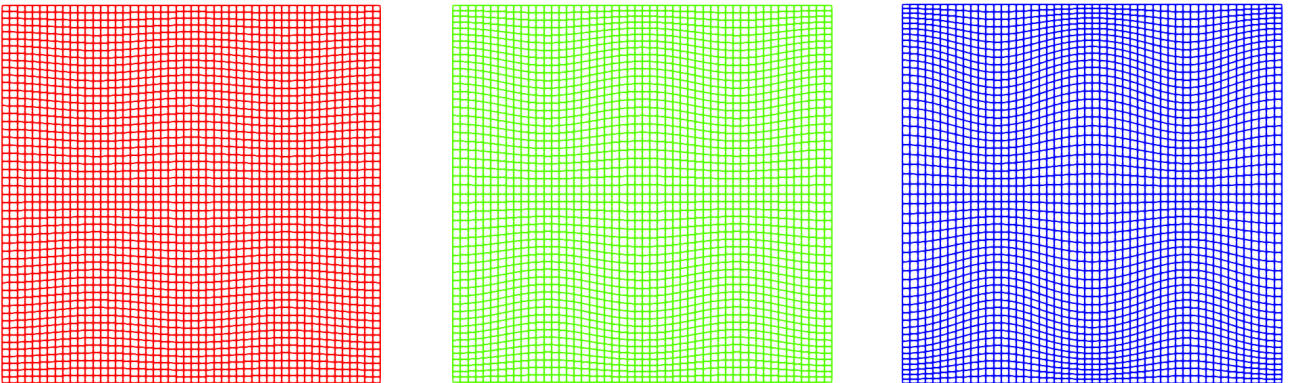
Figure 3.3: HTD meshes with $DP = 1.0$ (left), $DP = 1.5$ (center), and $DP = 2.0$ (right). Every four points are shown in each direction.

The streamwise evolutions of the vertical velocity and pressure at final time ($t = 5$) are shown in figures 3.4 and 3.5 for three different deformation parameters. In this case, the results are in perfect agreement with the reference values for every tested cases. The errors on both p_{min} and v_{max} are really small as shown in Table 3.3. It is noteworthy that the errors are distortion-independent up to $DP = 2.0$ and even for the highest tested deformation ($DP = 4.0$) they stay insignificant (0.1% on p_{min} and 0.3% on v_{max}). This observation tends to show that the errors in this case are scheme-induced rather than distortion induced.
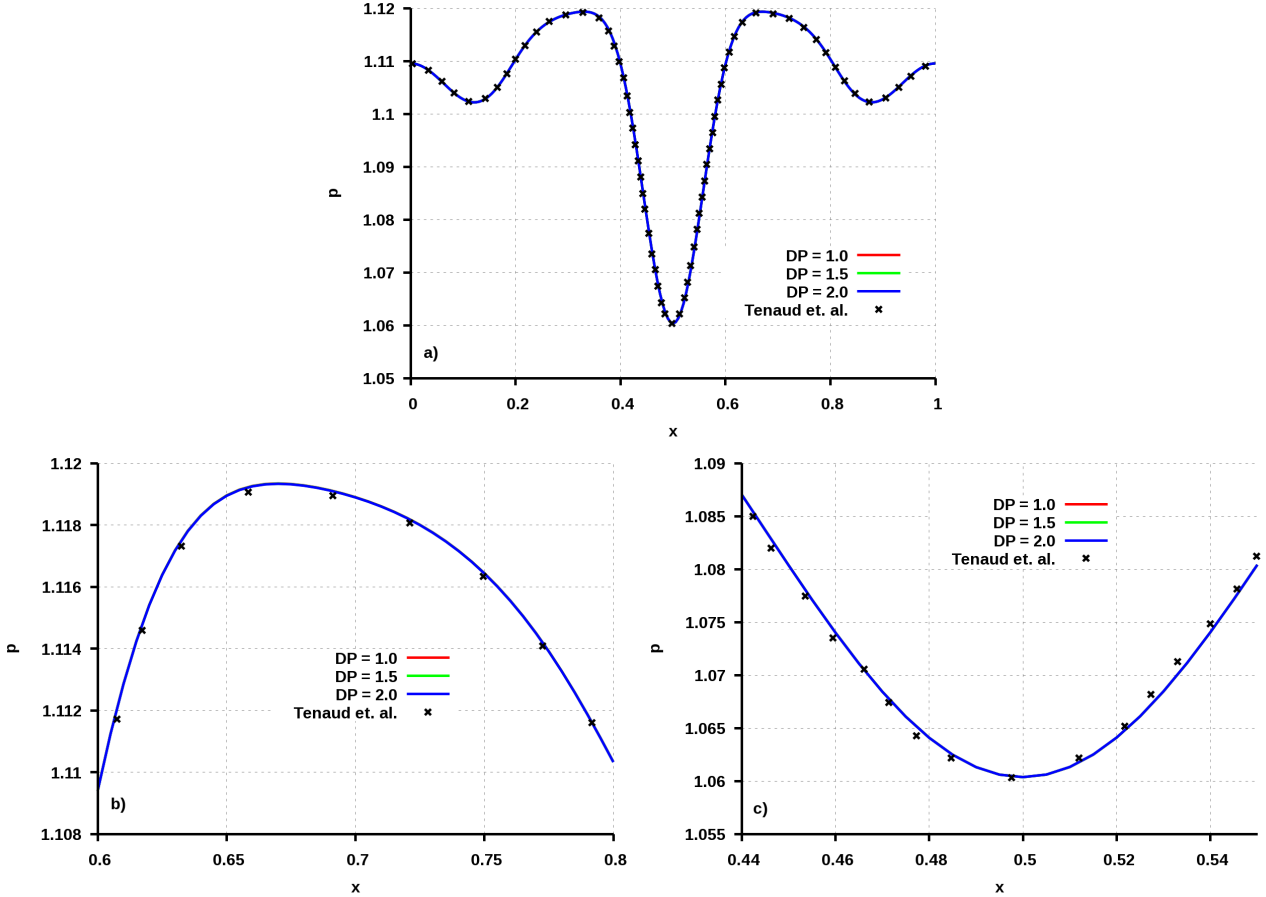
Figure 3.4: Streamwise evolution of the pressure at $y = 0.5$ and $t = 5$ for three different HTD meshes. a: Whole domain; b: Zoom on p_{max}; c: Zoom on p_{min}.

The isocontours of both the vertical velocity and pressure plotted in figure 3.6, shows that no significant differences are visible between the cases.

The present results have been shown to be in very good agreement with the reference data when the cells are distorted but stay quasi-orthogonal almost everywhere. Another type of deformation, that does not conserve the mesh-orthogonality has also been tested in order to check the response of the CHORUS code in such cases.

3.1.3.2 Sine-distorted mesh

In order to have very skewed, non-orthogonal cells, a sine-deformation have been created using Eq. 2.30. Several deformation amplitudes have been chosen, ranging from $A = 0.03$
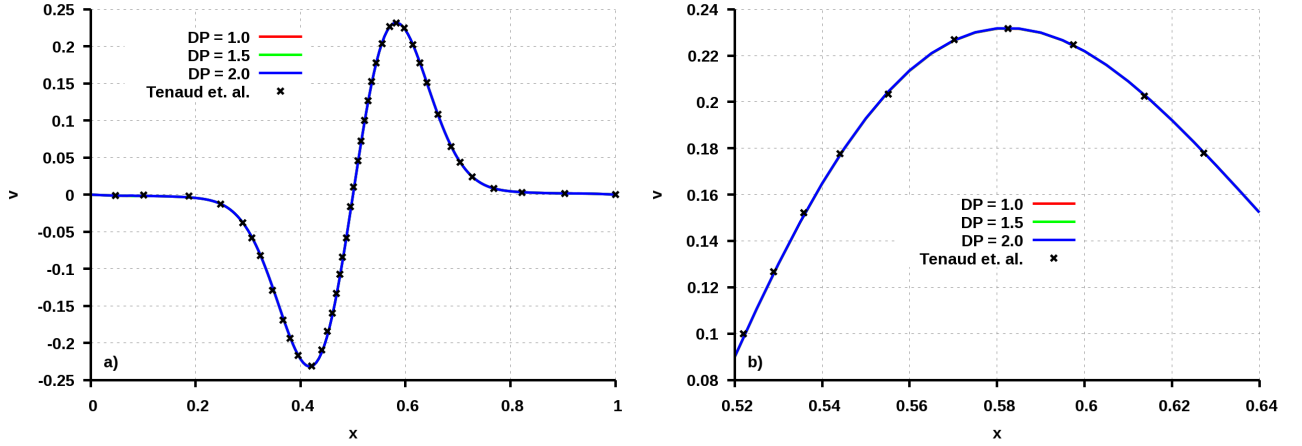
Figure 3.5: Streamwise evolutions of the vertical velocity at $y = 0.5$ and $t = 5$ for three different HTD meshes. a: Whole domain; b: Zoom on v_{max}.

Case	p_{min}		v_{max}	
	Value	Error %	Value	Error %
Tenaud *et. al.* [148]	1.06052	-	0.231630	-
Cartesian mesh	1.06036	0.01	0.23160	0.01
$DP = 1.0$	1.06037	0.01	0.231813	0.08
$DP = 1.5$	1.06037	0.01	0.231840	0.09
$DP = 2.0$	1.06037	0.01	0.231864	0.1

Table 3.3: Errors on the minimum pressure and maximum vertical velocity with respect to the reference values at $t = 5$, for 3 different HTD meshes.

to $A = 0.30$, but only the results obtained with $A = 0.03$, $A = 0.09$ and $A = 0.18$ will be presented here. The resulting meshes can be found in Figure 3.7.

The streamwise evolutions of the vertical velocity and pressure at final time ($t = 5$) are shown in figures 3.8 and 3.9 for three different distortion amplitudes. It is clear that for small and mild deformations, the results show a very good agreement with the reference values, both for the pressure and vertical velocity (Table 3.4). For a strong deformation ($A = 0.18$), the velocity and pressure profiles start to diverge from the reference data but the relative error stays perfectly acceptable (around 1.2%). An extreme deformation has also been tested ($A = 0.30$). Even in this very unfavourable case, the errors are very limited (0.8% on p_{min} and 3.3% on v_{max}).

The influence of distortion is also illustrated by isocontours of both the vertical velocity and pressure in figure 3.10. As suspected provided the values in Table 3.4, the differences are very small between all the cases and are gathered in the part where the cells are more distorted.

The simulations for SD meshes have shown that, although the error is quite larger than for HTD meshes, the results are in good agreement with the reference data even when the cells are very skewed. Unlike in the hyperbolic-tangent case, the error in this case seem to be deformation dependent since it goes from 0.02% for $A = 0.03$ to 1.2% for $A = 0.18$.
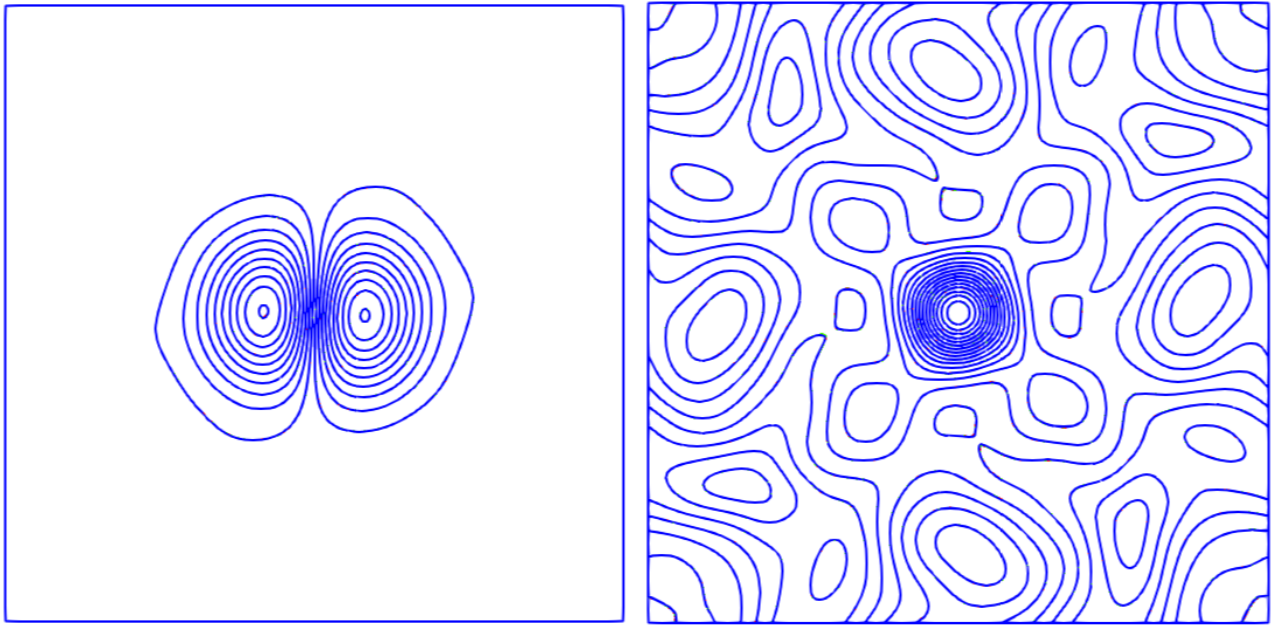
Figure 3.6: Isocontours of the vertical velocity (left) and pressure (right) at $y = 0.5$ and $t = 5$ for three different HTD meshes.
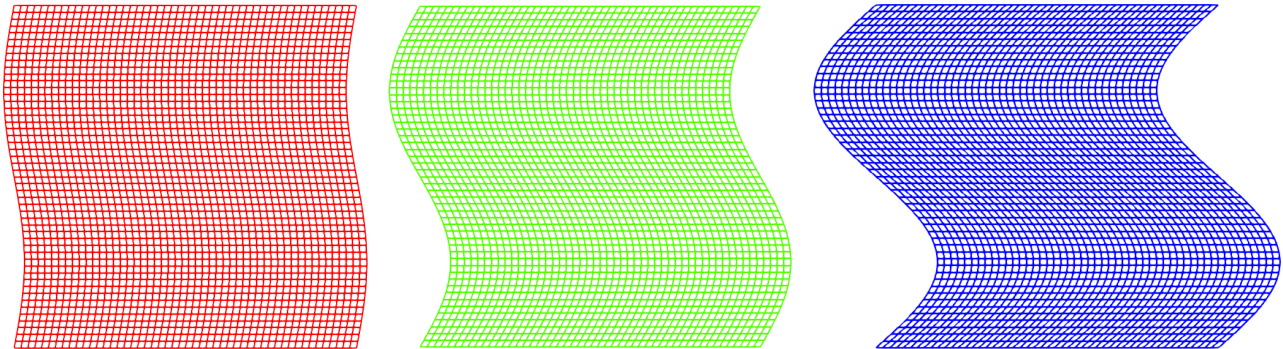
Figure 3.7: SD meshes with $A = 0.03$ (left), $A = 0.09$ (center), and $A = 0.18$ (right). Every four points are shown in each direction.

Case	p_{min}		v_{max}	
	Value	Error %	Value	Error %
Tenaud *et. al.* [148]	1.06052	-	0.231630	-
Cartesian mesh	1.06036	0.01	0.23160	0.01
$A = 0.03$	1.06038	0.01	0.231592	0.02
$A = 0.09$	1.06069	0.02	0.230922	0.3
$A = 0.18$	1.06266	0.2	0.228897	1.2

Table 3.4: Errors on the minimum pressure and maximum vertical velocity with respect to the reference values at $t = 5$, for 3 different SD meshes.
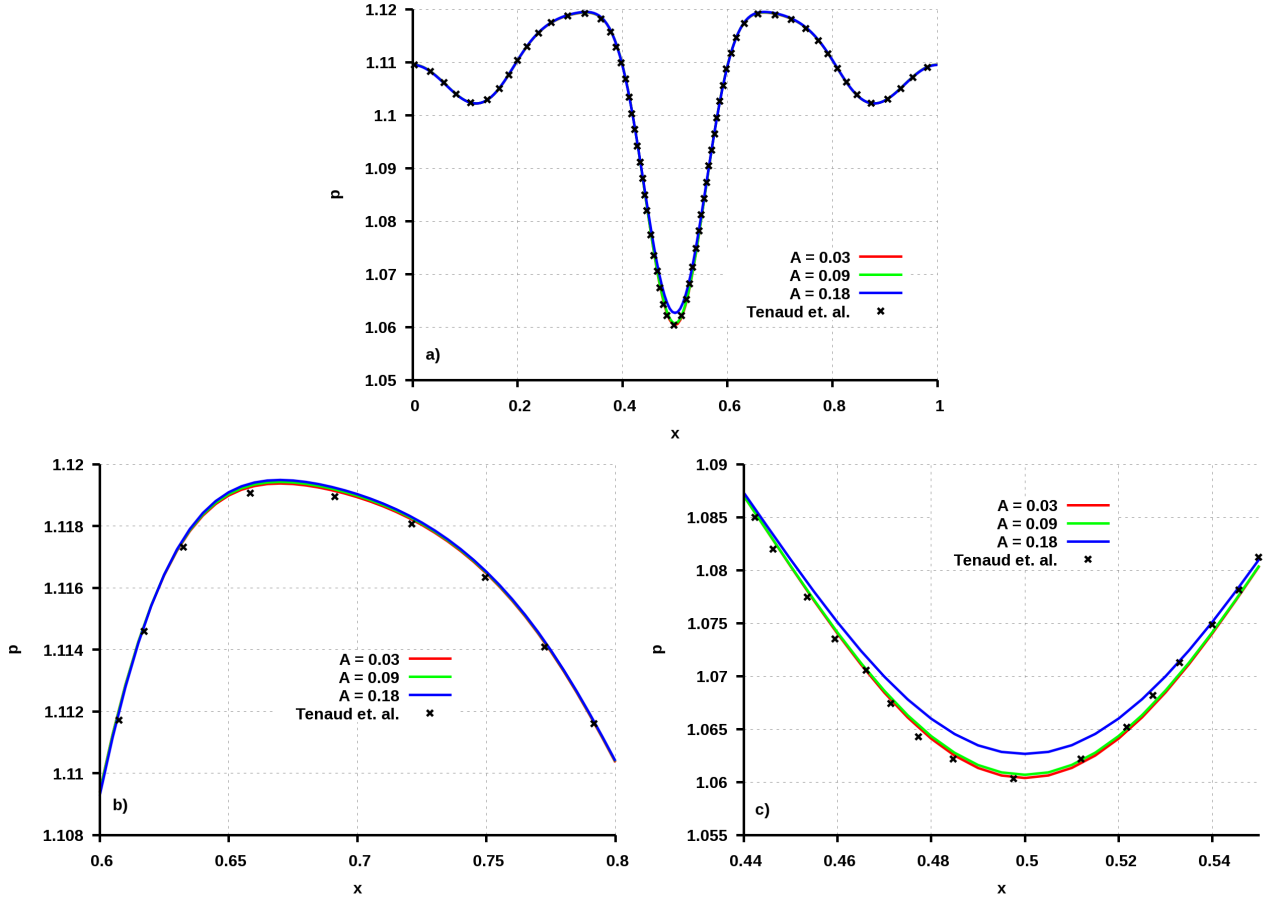
Figure 3.8: Streamwise evolution of the pressure at $y = 0.5$ and $t = 5$ for three different SD meshes. a: Whole domain; b: Zoom on p_{max}; c: Zoom on p_{min}.
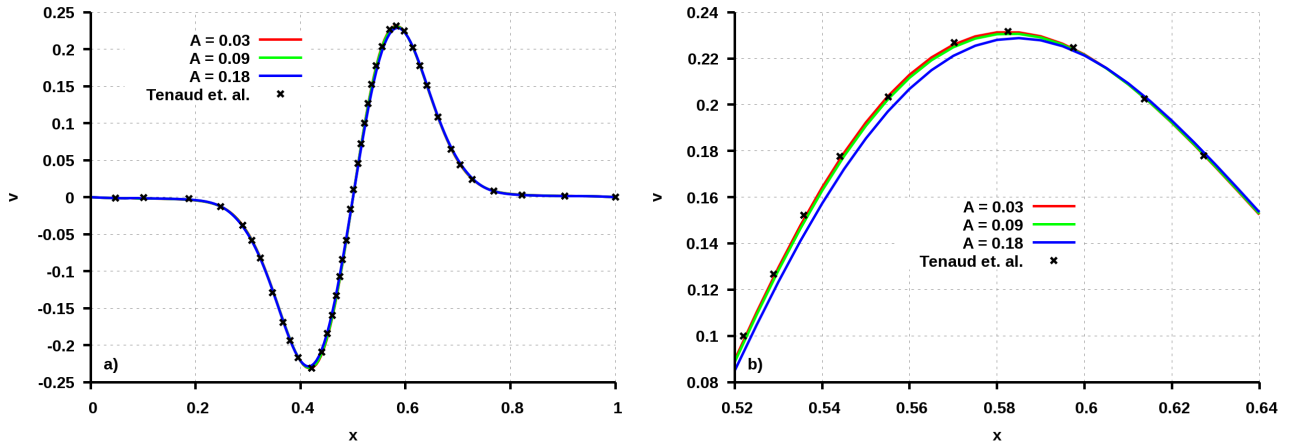
Figure 3.9: Streamwise evolutions of the vertical velocity at $y = 0.5$ and $t = 5$ for three different SD meshes. a: Whole domain; b: Zoom on v_{max}.

In this part, two different deformations have been tested fo the canonical case of a vortex convected by a uniform flow. The results obtained show a very good agreement with the
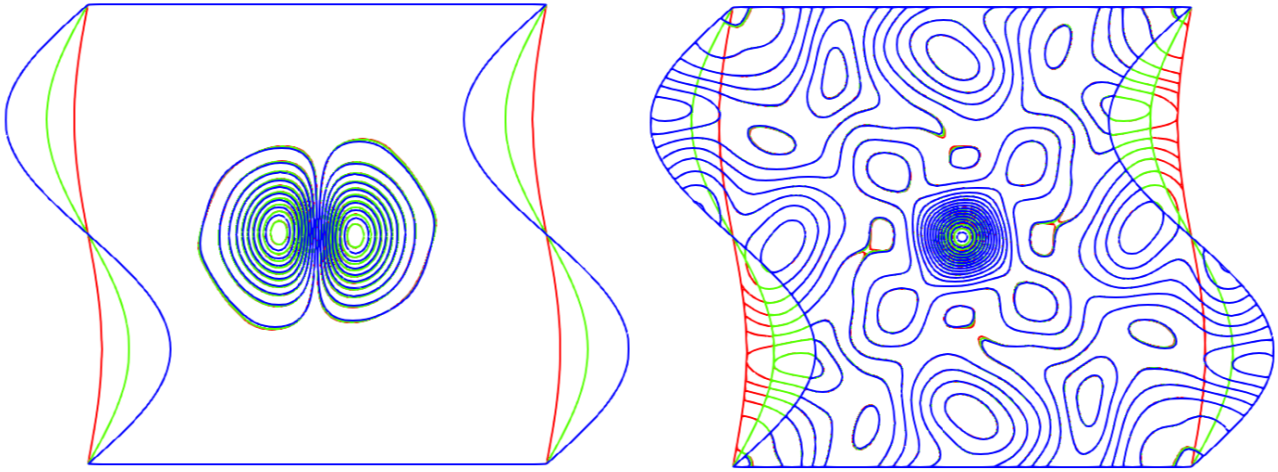
Figure 3.10: Isocontours of the vertical velocity (left) and pressure (right)at $y = 0.5$ and $t = 5$ for three different sine-distorted meshes.

reference data, even for large deformations. In addition, the conservation of the cell-orthogonality seems to lead to smaller errors than the use of non-orthogonal meshes. A study on the influence of the mesh orthogonality has been performed in the compression ramp case and will be presented in section 4.4.

3.2 Interaction between a shock wave and a temperature spot

Introduction

The second test-case to be considered is the well-known example of the interaction between a shock wave and a temperature spot. This is a canonical case based on problems that are typically encountered when a flame is hit by a shock wave. The goal here is to analyse the capability of the shock-capturing techniques implemented in CHORUS to correctly predict the mechanisms of vorticity production in presence of a shock wave for distorted meshes.

Two of the most relevant quantities to check if one wants to assess a code's ability to predict the vorticity production are the integrals of the moduli of vorticity (IVM) and baroclinic torque (IBT) over the whole domain Ω. They are defined by:

$$IVM = \int_\Omega |\omega|\, d\Omega \tag{3.1}$$

$$IBT = \int_\Omega \left| \frac{\nabla P \times \nabla \rho}{\rho^2} \right| d\Omega \tag{3.2}$$

The flow considered here being 2D and nearly inviscid, the baroclinic torque is the only mechanism that can create vorticity.

3.2.1 Flow configuration

A rectangular domain, of dimensions $[0, 2] \times [0, 1]$, is initially split into two regions by a normal shock wave located at $x_0 = 1$ (Fig. 3.11).
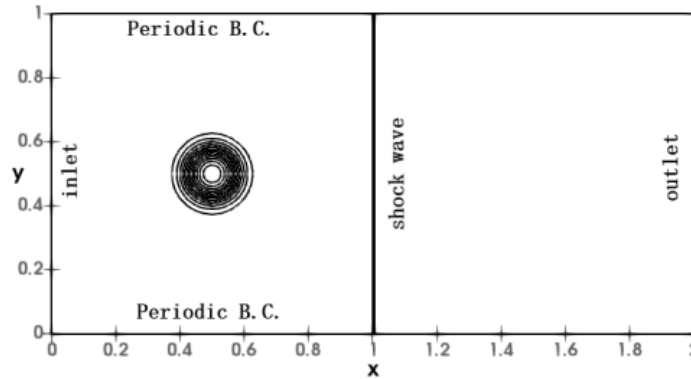
Figure 3.11: Illustration of the initial and boundary conditions in the case of the interaction between a shock wave and a temperature spot. From Tenaud *et. al.* [148]

For $x < x_0$, the flow conditions (ρ_0, u_0, T_0 and p_0) are chosen such that $M_0 = 1.1588$. Re_0, the Reynolds number based on the flow conditions upstream of the shock and on x_0, is equal to 2,000. The pressure jump through the shock wave is $\frac{\Delta p}{p_0} = 0.4$. Downstream of the shock wave, the remaining variables are initialised by using Rankine-Hugoniot

relationships. A spot of temperature, centred at $(x_0, y_0) = (0.5, 0.5)$, is then superimposed to the base flow. It is defined by:

$$\frac{\Delta T(r)}{T_0} = \frac{1}{\alpha^4}(r^2 - \alpha^2)^2 e^{-\frac{r^2}{\sigma^2}}$$

where $r = \sqrt{(x - x_0)^2 + (y - y_0)^2}$ is the distance from the center of the temperature spot. $\alpha = 7$ and $\sigma = 0.07$ are two constants defining the size of the temperature spot.

From a numerical point of view, the time step is chosen such that $CFL < 0.5$. Periodic boundary conditions are applied on top and bottom boundaries. The upstream boundary is considered as an inlet whereas the downstream boundary is set as an outlet (See section 2.4 for more details). All the simulations have been run for a dimensionless time $t = 1$, which guarantees that the temperature spot will entirely cross the shock wave.

3.2.2 Mesh Convergence

Before considering the influence of the distortion, a mesh convergence study has been performed. Four uniform cartesian meshes have been considered ranging from 800 to $80,000$ cells. The mesh parameters and timesteps are gathered in Table 3.5.

Mesh Name	# of Cells	Δt
M_1	40×20	$5 \ 10^{-3}$
M_2	100×50	$2.5 \ 10^{-3}$
M_3	200×200	10^{-3}
M_4	400×200	$5 \ 10^{-4}$

Table 3.5: Mesh parameters

The time evolutions of IVM (Eq. 3.1) and normalised IBT (Eq. 3.2) are plotted in Figure 3.12 for four different cartesian meshes.
The observation of the reference data is really useful to understand the underlying physics of the flow. Since the initial flow field does not introduce any vorticity, both integrals are equal to zero up to $t = 0.3$. At that particular time, the temperature spot starts to interact with the shock wave and vorticity is being created by the baroclinic effect. The production sharply increases up to $t = 0.5$, as the first half of the spot crosses the shock wave, and then decreases as sharply to reach a very low value after $t = 0.7$. This non-zero value is due to the fact that the interaction is not entirely over.

The analysis of the results for IVM shows that it is largely over-predicted after $t = 0.5$ for resolution up to M_3 (Table 3.6). Those results agree with the observation from Tenaud *et. al.* [148] showing that TVD schemes induce the creation of extra vorticity within the shock after the interaction. This is confirmed by Figure 3.13 in which the residual vorticity created within the shock can be seen. It is obvious that using a finer mesh decrease this non-physical vorticity creation. As a consequence, all the simulations in the following part will be carried on with a number of cells equivalent to M_4 in order to
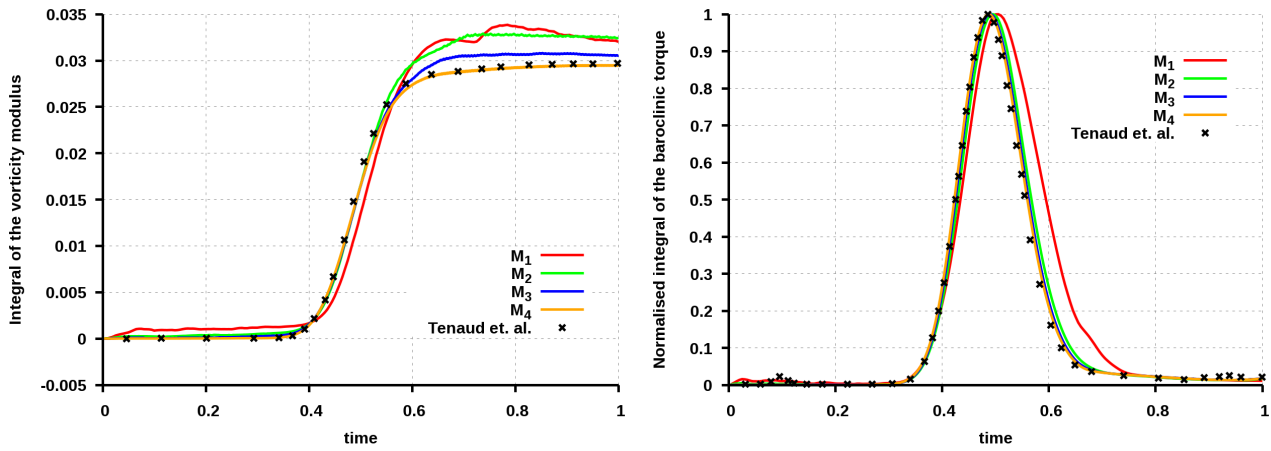
Figure 3.12: Time evolution of IVM (left) and normalised IBT (right) for four different cartesian meshes.

limit the influence of the TVD scheme. Concerning IBT, all meshes (except M_1) are in good agreement with the reference values.

Mesh	IVM at $t = 1$.	
	Value	Error %
Tenaud *et. al.* [148]	0.0297	-
M_1	0.0320	7.7
M_2	0.0325	9.4
M_3	0.0306	3.0
M_4	0.0295	0.7

Table 3.6: Error on the integral of the vorticity modulus at $t = 1.0$, for 4 different meshes.
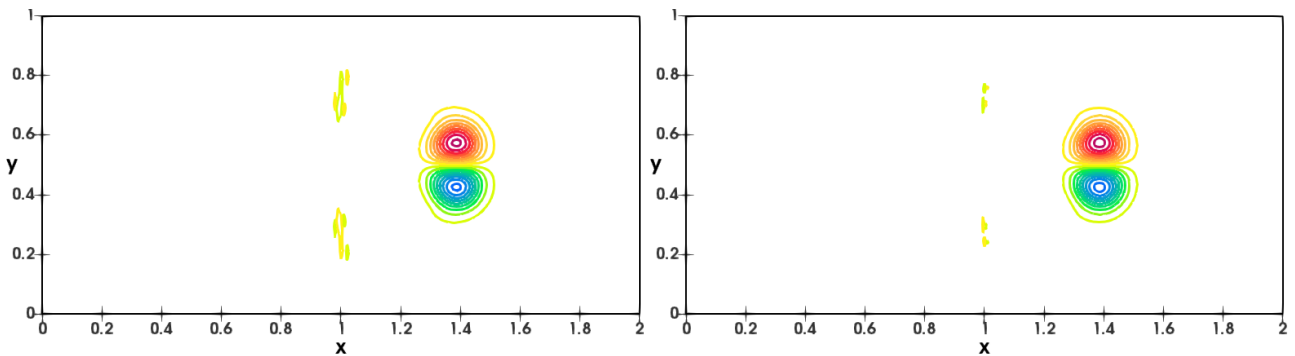
Figure 3.13: Isocontours of vorticity at $t = 1$ obtained for M_3 (left) and M_4 (right).

Influence of Distortion

Because of the flow geometry, and more precisely the presence of a straight vertical shock wave, only hyperbolic-tangent distortions (Eq. 2.28) have been used. Several deformation parameters have been chosen, ranging from $DP = 0.5$ to $DP = 3.5$, but only the results for $DP = 1.0$, $DP = 2.0$ and $DP = 3.0$ will be presented here. The subsequent meshes can be found in Figure 3.14.
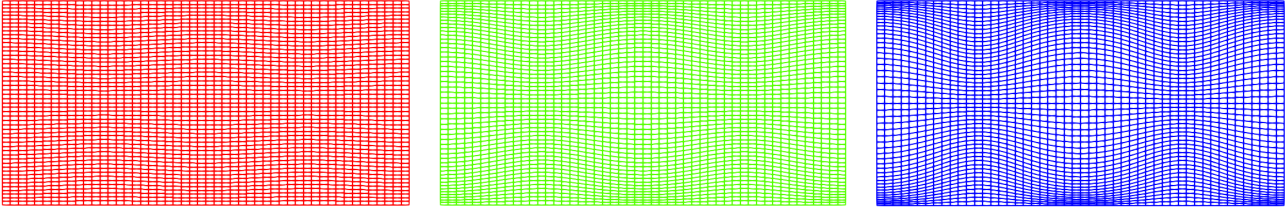
Figure 3.14: Hyperbolic tangent-distorted mesh with three different distortion parameters.

For this test case, the influence of the distortion is negligible (Figure 3.15). Quantitatively, the error is less than 1% for all the tested deformation parameters and is identical to the one obtained in the cartesian case (Table 3.7).
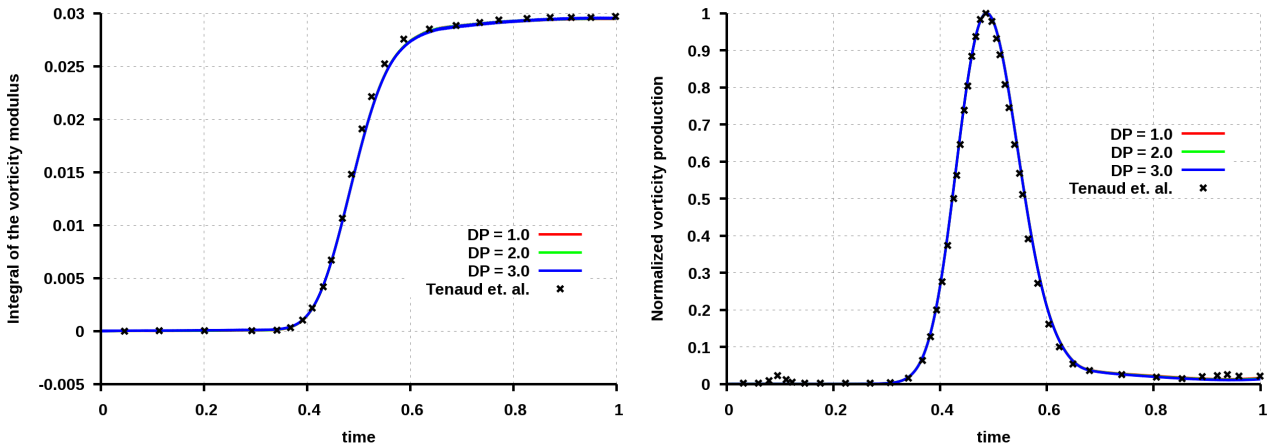
Figure 3.15: Time evolution of IVM (left) and normalised IBT (right) for three different HTD meshes.

A qualitative study has been carried out through the comparison of several isocontours (pressure, density, and vorticity) with the reference data for $t = 0.5$ and $t = 1.0$. $t = 0.5$ corresponds to the moment when the centre of the spot of temperature reaches the position of the shock wave and therefore the maximum of vorticity production. At that time, the flow fields are very similar between the present DNS results and the data from Tenaud *et. al.* . All the characteristics of the interaction are recovered, such as the pressure waves originating from the centre of the temperature spot, the bending of the initially straight shock wave, and the creation of two contra-rotating vortices just downstream of the interaction. At the final time ($t = 1$), the shape of the isocontours of density and pressure near the shock wave, proving that the interaction between the shock wave and temperature spot is still active even though the temperature spot is positioned

Mesh	IVM at $t = 1$.	
	Value	Error %
Tenaud *et. al.* [148]	0.0297	-
Cartesian mesh	0.0295	0.7
$DP = 1.0$	0.0295	0.7
$DP = 2.0$	0.0295	0.7
$DP = 3.0$	0.0295	0.7

Table 3.7: Error on the integral of the vorticity modulus at $t = 1.0$, for 3 different distortion parameters.

at $(x = 1.4)$, are very close to the reference one. As discussed earlier, the only significant difference comes from the presence of vorticity contours inside the shock wave that are neither physical nor recovered by the reference simulations.

In this part, the case of the interaction between a temperature spot and a shock wave has been studied for cartesian and HTD meshes. In the former case, the ability of Chorus to tackle flows with shock waves in cartesian geometry has been confirmed, with a very good agreement with the reference data. In the latter case, the influence of the mesh distortion has been shown to be very insignificant, leading to errors equivalent to those for a cartesian mesh, and recovering every expected features of the flows with accuracy.
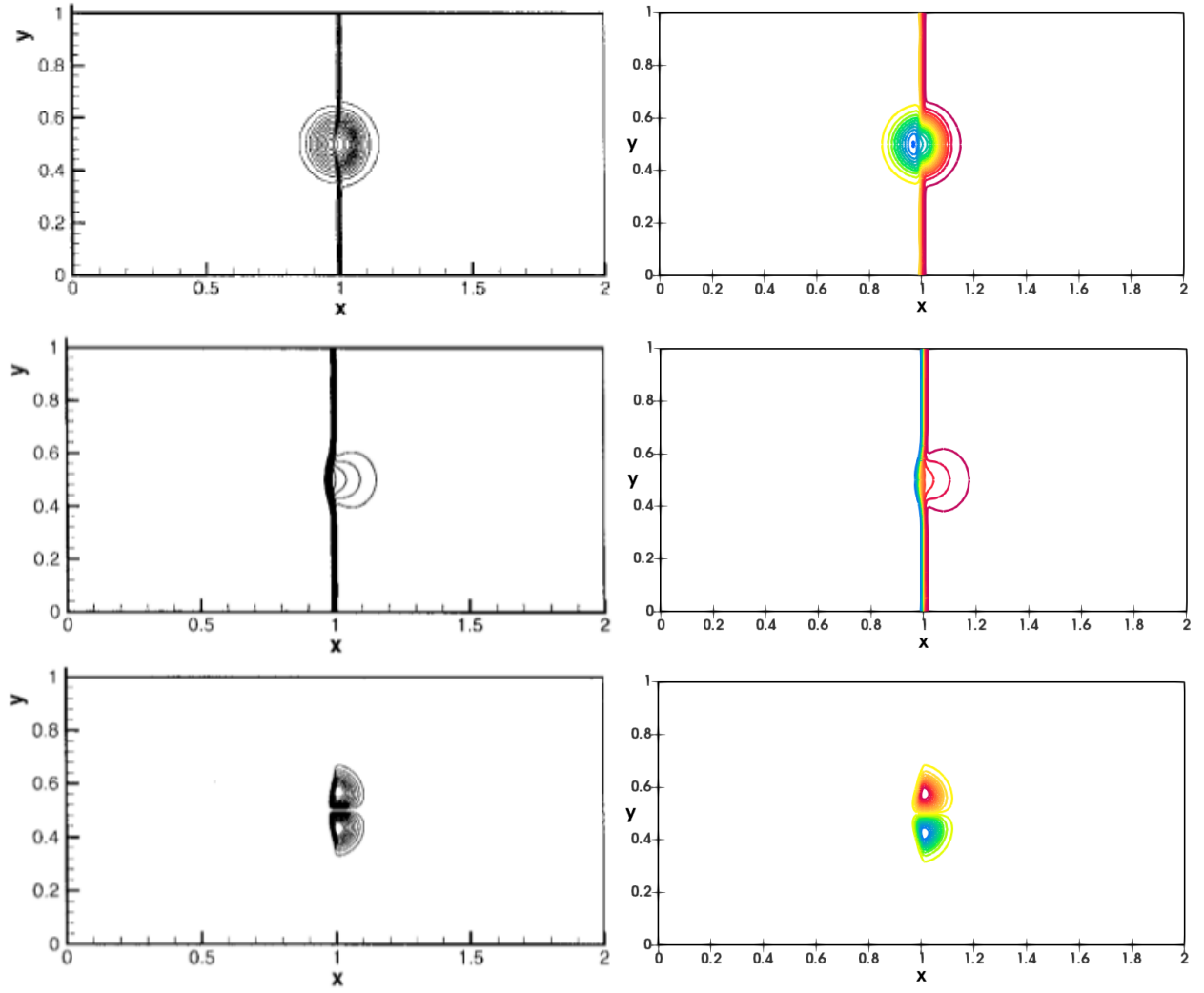
Figure 3.16: Isocontours of density (top), pressure (center) and vorticity (bottom) for $t = 0.5$. Left: Reference data from [148]; right: Present results obtained with $DP = 3.0$.
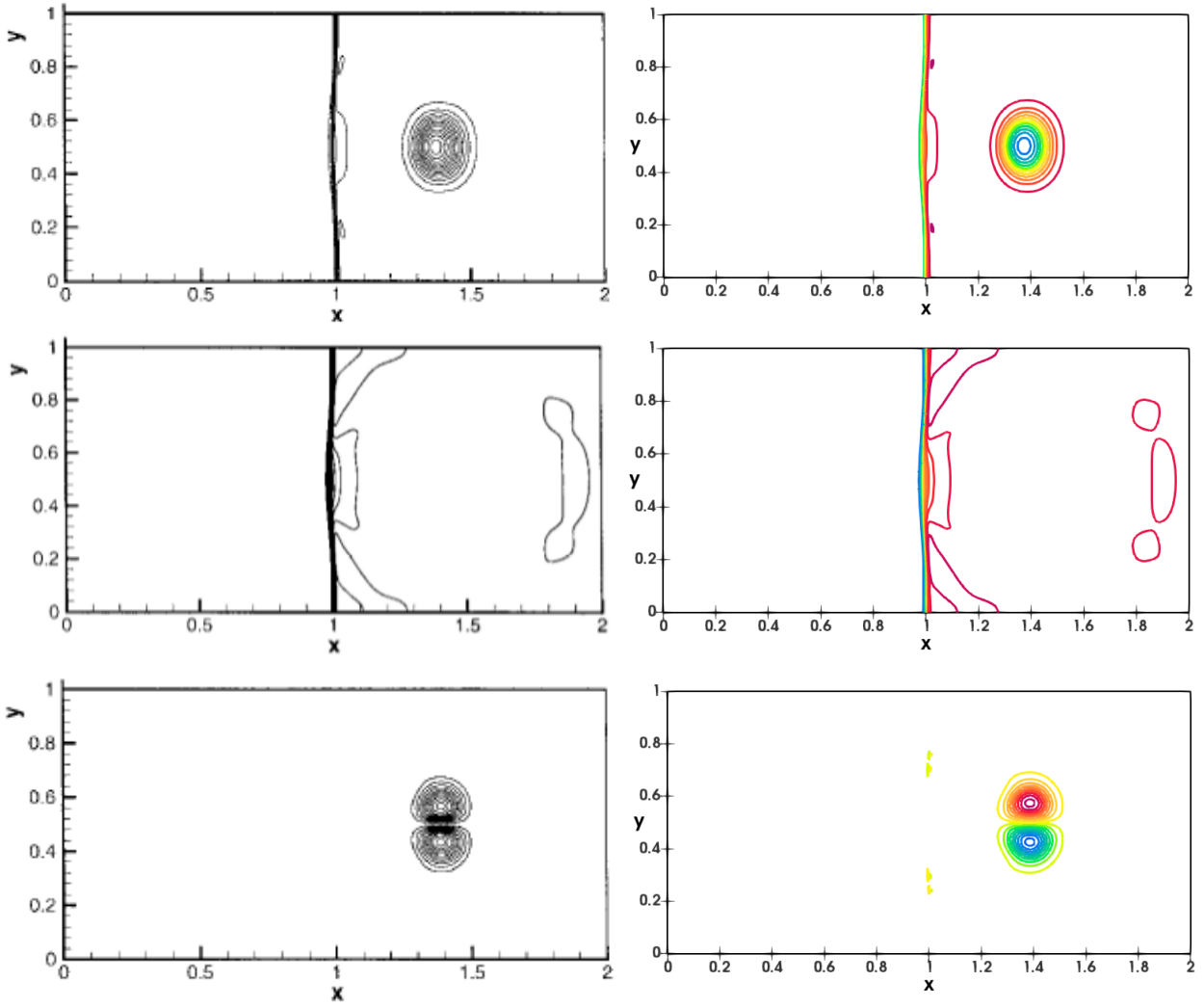
Figure 3.17: Isocontours of density (top), pressure (center) and vorticity (bottom) for $t = 1.0$. Left: Reference data from [148]; right: Present results obtained with $DP = 3.0$.

3.3 Taylor-Green Vortex

Introduction

The third test-case to be considered is the 3D case of the Taylor-Green Vortex (TGV), one of the problems that have been intensively studied since 2012 in the framework of the *International Workshop on High Order CFD Methods* [158]. The goal here is to switch to a 3D flow and analyse the capability of the OSMP scheme to accurately predict the decay cascade of homogeneous turbulence (but not isotropic) for distorted meshes.

Two of the mandatory results to be plotted for the benchmark are the temporal evolution of the kinetic energy integrated on the whole computational domain (Ω) (E_k) and the temporal evolution of the kinetic energy dissipation rate (ϵ), defined by:

$$E_k = \frac{1}{\rho_0 \Omega} \int_\Omega \rho \frac{\mathbf{v} \cdot \mathbf{v}}{2} \, d\Omega \tag{3.3}$$

$$\epsilon = -\frac{dE_K}{dt} \tag{3.4}$$

3.3.1 Flow configuration

In a three-dimensional domain of dimensions $[-\pi, \pi]^3$, a Taylor-Green Vortex (TGV) is created by imposing the following initial conditions:

$$\rho = \rho_0$$
$$u = u_0 \, sin\left(\frac{x}{L_0}\right) cos\left(\frac{y}{L_0}\right) cos\left(\frac{z}{L_0}\right)$$
$$v = -u_0 \, cos\left(\frac{x}{L_0}\right) sin\left(\frac{y}{L_0}\right) cos\left(\frac{z}{L_0}\right)$$
$$w = 0$$
$$T = T_0$$
$$p = \frac{\rho_0 T_0}{\gamma M^2} + \frac{\rho_0 u_0^2}{16}\left(cos\left(\frac{2x}{L_0}\right) + cos\left(\frac{2y}{L_0}\right)\right)\left(cos\left(\frac{2z}{L_0}\right) + 2\right)$$

where ρ_0, u_0, T_0 and L_0 are the reference density, velocity, temperature, and length, respectively, and are all set equal to 1. The fluid is supposed to verify the ideal gas law with $\gamma = c_p/c_v = 1.4$ and $Pr = 0.71$. The Mach number is chosen such that the flow is nearly incompressible ($Ma = 0.1$) and therefore, the viscosity and heat conductivity are assumed constant. The Reynolds number, based on u_0 and L_0, is equal to 1,600. From a numerical point of view, the time step is chosen such as $CFL = 0.5$, and periodic boundary conditions are applied in all three directions. The simulations have been run for 20 periods, corresponding to a dimensionless time $t = 20$.

The underlying physics of this flow is very interesting and complex though rather easy to apprehend. Initially independent from one another (Fig. 3.18-left), the eight large vortical structures start to interact with each other. Those non-linear interactions will

force the flow to undergo the transition towards turbulence that will lead to the creation of smaller and smaller structures until their kinetic energy is dissipated into heat at Kolmogorov scales (Fig. 3.18-right). It is noteworthy that even if the flow is not isotropic, this decay phase is very similar to the one observed for homogeneous isotropic turbulence.
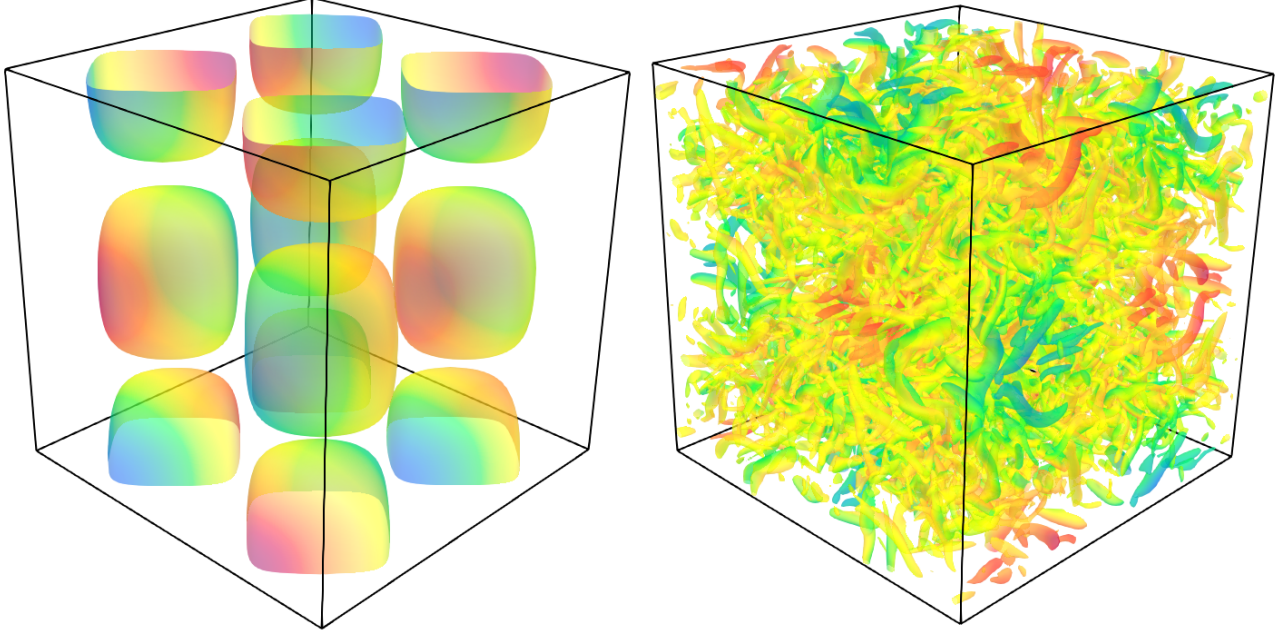
Figure 3.18: Vortical structures evidenced by using the Q-criterion coloured by the x-component of the velocity. Left: $t = 0$; right: $t = 20$.

3.3.2   Mesh Convergence

A mesh convergence study has been performed for uniform cartesian meshes ranging from 32^3 to 512^3 CVs. The mesh parameters are gathered in Table 3.8.

Mesh Name	# of CVs	Δt
M_1	32^3	$5\ 10^{-3}$
M_2	64^3	$5\ 10^{-3}$
M_3	128^3	$2\ 10^{-3}$
M_4	256^3	10^{-3}
M_5	512^3	$5\ 10^{-4}$

Table 3.8: Mesh parameters

The time evolution of the dissipation rate ϵ is plotted in figure 3.19-left. It could be split into two parts. Up to $t = 9$, ϵ is sharply increasing. The dissipation occurring at the Kolmogorov scale, this increase of ϵ is linked to the progressive creation of smaller and smaller structures through the energy cascade. At this point, small structures stop to

be created and as the flow is not fed by any kind of external energy, the decay towards a fluid at rest starts to occur. As expected by the previous observations, the coarsest mesh, M_1, is in very poor agreement with the reference data taken from Wang *et. al.* [158]. Because of the size of its cells, this mesh is unable to correctly capture the small structures of the flow and the associated dissipation. As a consequence, the dissipation peak appears much too early and the decay is occurring much too quickly. This behaviour leads to a wrong profile for the kinetic energy, directly linked to ϵ through Eq. 3.4, with lower-than-expected values before $t = 11$ and higher-than-expected values after $t = 11$ (Figure 3.19-right). To a lesser extent, the same phenomenon is observed for M_2. A very good agreement is found for 128^3 CVs (M_3), 256^3 CVs (M_4) and 512^3 CVs (M_5), even if the dissipation peak is significantly underestimated for 128^3 CVs (Table 3.9). It is noteworthy that the reference data were obtained using a dealiased pseudo-spectral code (developed at Université Catholique de Louvain) which is known to have spatially neither numerical dissipation nor numerical dispersion errors. The excellent results obtained for M_4 and M_5 compared to the reference data (less than 1.5% for equivalent meshes) hence demonstrate the very high efficiency of CHORUS in the framework of turbulent flows.
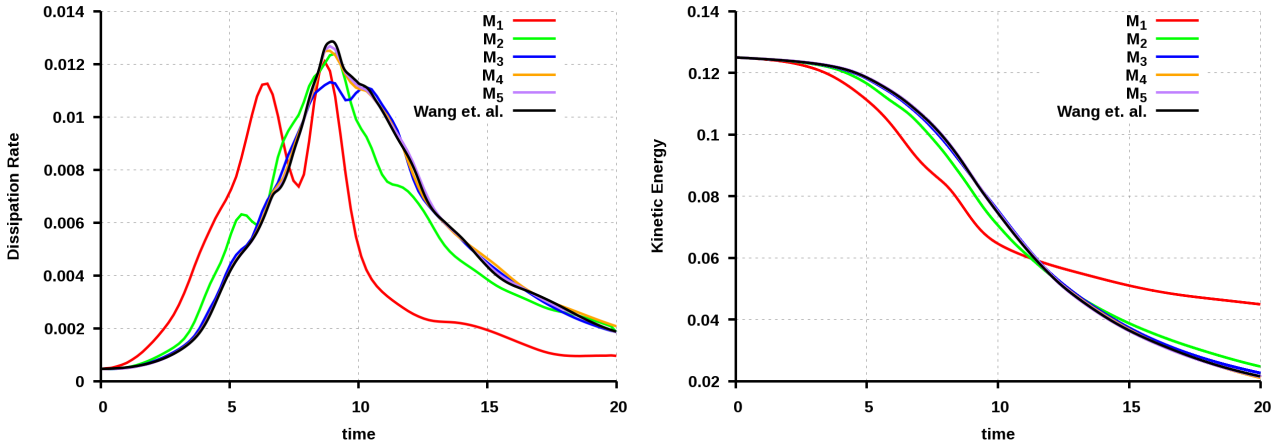
Figure 3.19: Time evolution of the dissipation rate ϵ (left) and the kinetic energy of the whole domain E_k (right) for five different cartesian meshes.

Case	E_{kmin}		ϵ_{max}	
	Value	Error %	Value	Error %
Wang *et. al.* [158]	0.02157	-	0.01286	-
M_1	0.04492	108.2	0.01209	5.9
M_2	0.02475	14.7	0.01241	3.5
M_3	0.02263	4.9	0.01132	11.9
M_4	0.02112	2.1	0.01255	2.4
M_5	0.02150	0.3	0.01269	1.3

Table 3.9: Errors on the minimum of Kinetic Energy and the maximum of dissipation rate with respect to the reference values, for five different cartesian meshes.

Provided the very small errors occurring for M_4, the influence of the distortion will be run using the same quantity of cells (256^3).

3.3.3 Influence of Distortion

Because of the rather high cost of the simulations, around 600 CPU hours per case on IDRIS' Ada (IBM x3750) for 256^3 CVs, only one kind of deformation could have been studied. As the very small influence of the distortion for HTD meshes has already been demonstrated for the convection of a vortex (advection-diffusion case) and the interaction between a shock wave and a temperature spot (flow with shock), sine-distorted meshes will be used in this part. The intended goal is to confirm one of the first observations that have been made for sine-distorted meshes, indicating that the error seemed to be deformation-dependent.

As the flow here is 3D, sine-deformation has been applied in all three directions using Eq. 2.31. Several distortion amplitudes ranging from $A = 0.03$ to $A = 0.60$ but only results for $A = 0.09$, $A = 0.18$ and $A = 0.30$ will be presented here. The distorted meshes obtained with those parameters can be found in Figure 3.18-top.

As shown in figure 3.20 and confirmed by Table 3.10, the error is not sensitive to the deformation amplitude. Indeed, as soon as a deformation is imposed to the geometry, the errors take values close to 7% for E_{kmin} and 3% for ϵ_{max}. This observation is to be tempered since a more extensive study shows that the previous statement is valid only up to a certain amplitude of deformation roughly estimated here at around $A = 0.30$ (Fig. 3.21). For stronger deformations, the error on the kinetic energy is quickly increasing even if it is not the case for the dissipation.
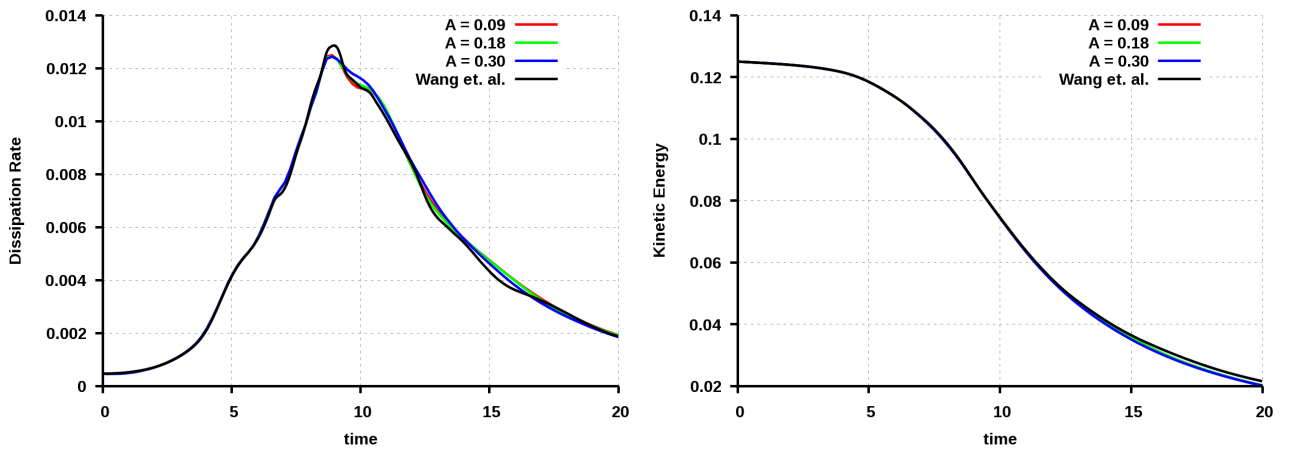
Figure 3.20: Time evolution of the dissipation rate ϵ (left) and the kinetic energy of the whole domain E_k (right) for three different SD meshes.

The errors obtained here, for all the SD meshes, are the highest noted in this chapter, although the undistorted results are amongst the best. As stated for the vortex convection test-case, the rather high error is more likely due to the fact that the cells are very non-orthogonal in all directions.

Case	E_{kmin}		ϵ_{max}	
	Value	Error %	Value	Error %
Wang *et. al.* [158]	0.02157	-	0.01286	-
Cartesian mesh	0.02112	2.1	0.01255	2.4
$A = 0.09$	0.02007	7.0	0.01251	2.7
$A = 0.18$	0.02023	6.2	0.01245	3.2
$A = 0.30$	0.02014	6.6	0.01244	3.3

Table 3.10: Errors on the minimum of Kinetic Energy and the maximum of dissipation with respect to the reference values, for 5 different meshes.

Conclusion

This chapter allowed us to quantify the errors introduced by different types of deformation for three test-cases dealing with convection and/or turbulence and/or shocks. In its cartesian version, CHORUS has been shown to be a very efficient code in any situation. As expected, the deformation of the mesh creates errors that are rather low if the control volumes stay close to a parallelepiped (hence nearly orthogonal). If a non-orthogonality is introduced, the errors are significantly increased.

In the following chapters, where compression ramps are to be considered, a special care should then be taken when creating the meshes.
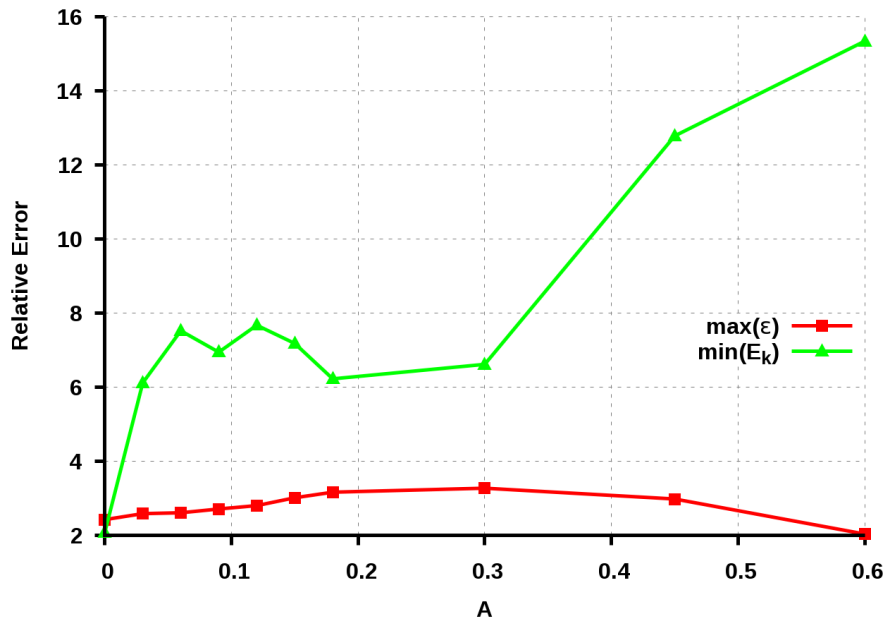
Figure 3.21: Evolution of the errors on E_{kmin} and ϵ_{max} as a function of the deformation amplitude A.
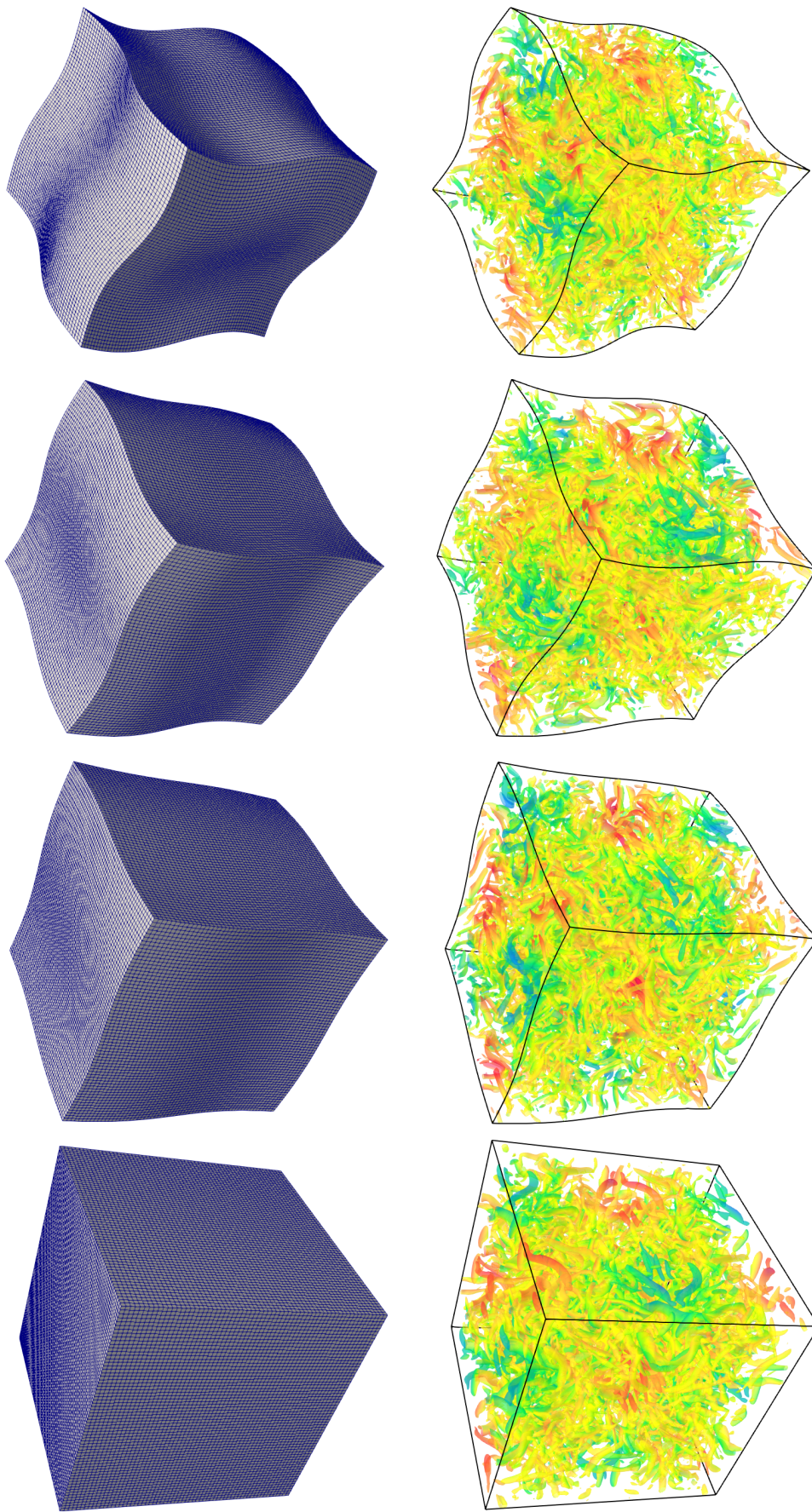
Figure 3.22: Mesh (top) and Isosurfaces of the Q-criterion coloured by the x-component of velocity at $t = 20$ (bottom) for four different meshes. From left to right: Cartesian mesh, $A = 0.09$, $A = 0.18$ and $A = 0.30$.

Chapter 4

Validation for the ramp case

Contents

Before innovative DNS are performed, the code needs to be validated on the framework of supersonic flows around compression corner, which is the core of the present dissertation. The validation studies have been carried out for the case of both inviscid and viscous flows over a compression ramp and the comparison with theoretical as well as numerical data will be presented here.

4.1 Inviscid case

The case of the steady, inviscid air flow around a compression corner has first been investigated. For this flow, theoretical solutions are available for the shock angle as well as for the pressure/temperature/density jump across the shock (See for instance [7] for a complete theoretical development).

4.1.1   Flow configuration

The simulations has been performed for a ramp angle and a Mach number ranging from $\theta = 10°$ to $\theta = 20°$ and from $Ma = 2$ to $Ma = 4$, respectively. The fluid properties are considered constant with $\gamma = 1.4$ and the Prandtl number $Pr = 0.72$. Air is supposed to verify the ideal gas law. The physical domain spans from $x = 0$ to $x = 0.22\ m$ and from $z = 0$ to $z = 0.0527\ m$ in the streamwise and wall-normal directions respectively. The ramp corner is located at $x_c = 0.0610\ m$ (Figure 4.1).
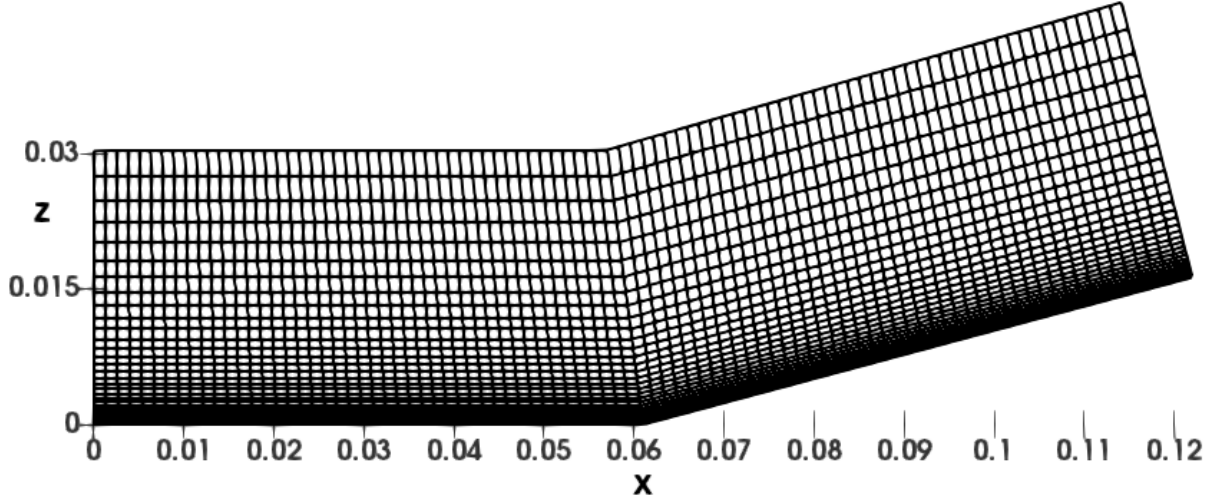
Figure 4.1: Example of a physical domain (and mesh) used for the validation in the inviscid case.

From a numerical point of view, a mesh of 90×30 cells has been chosen. An uniform spacing of $\Delta x = 1.35 \times 10^-3\ m$ has been used in the streamwise direction. A power law stretching, though unnecessary since the flow is inviscid, has been applied in the wall-normal direction resulting in cell sizes varying from of $\Delta z_{min} = 2 \times 10^{-4}\ m$ close to the wall to $\Delta z_{max} = 3 \times 10^{-3}\ m$ in the freestream. It was chosen to fit the mesh used for the comparative study with Carter's data, that will be presented in section 4.2. Concerning the boundary conditions, all flowfield variables are specified at the inlet (leftmost) boundary, outflow conditions are applied on both the top and rightmost boundaries. The wall has been treated as adiabatic and a slip condition has been applied.

4.1.2   Results

Contours of Mach number are shown in figure 4.2 for $(Ma = 2, \theta = 15°)$ and $(Ma = 3, \theta = 10°)$. As expected by the supersonic aspect of the flow, the presence of the ramp induces the creation of an oblique shock wave which has two major effects. First, the flow, originally horizontal upstream of the corner, is suddenly deviated to match the new boundary conditions downstream of the corner, where the flow still needs to be parallel to the wall. This results to a switch between kinetic and internal energies. As a consequence, pressure, density, and temperature are highly increased through the shock, at the expense of the velocity.
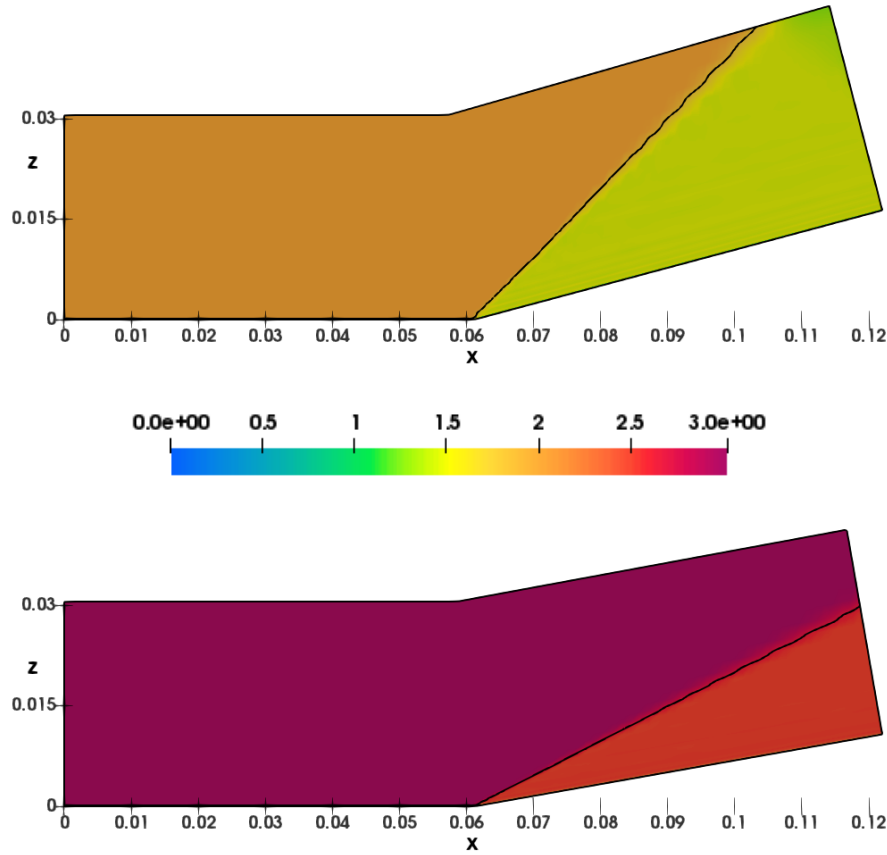
Figure 4.2: Contours of the Mach number for a inviscid flow on a supersonic ramp. Top: $Ma = 2$ and $\theta = 15°$. Bottom: $Ma = 3$ and $\theta = 10°$.

Ma_d, the Mach number downstream of the shock as well as β, the shock angle estimated from the previous figures, are gathered in Table 4.1. The results on both quantities are in very good agreement with the theoretical values.

Case	Ma_d		β	
	DNS	Theory	DNS	Theory
$Ma = 2$ and $\theta = 15°$	1.445	1.445	45.5°	45.3°
$Ma = 3$ and $\theta = 10°$	2.505	2.505	27.5°	27.4°

Table 4.1: Comparison between DNS results and theory for two inviscid cases.

The jump conditions across the shock wave are some very important quantities to monitor because they determine the physical reality of the shock. The pressure, density, and temperature profiles are shown in figure 4.3 and compared with the Rankine-Hugoniot results for the three different Mach numbers ($Ma = 2$ to 4) and ramp angle ($10°$ to $20°$). For every tested case, the theoretical values of Ma_d and β are perfectly recovered by Direct Numerical Simulations.
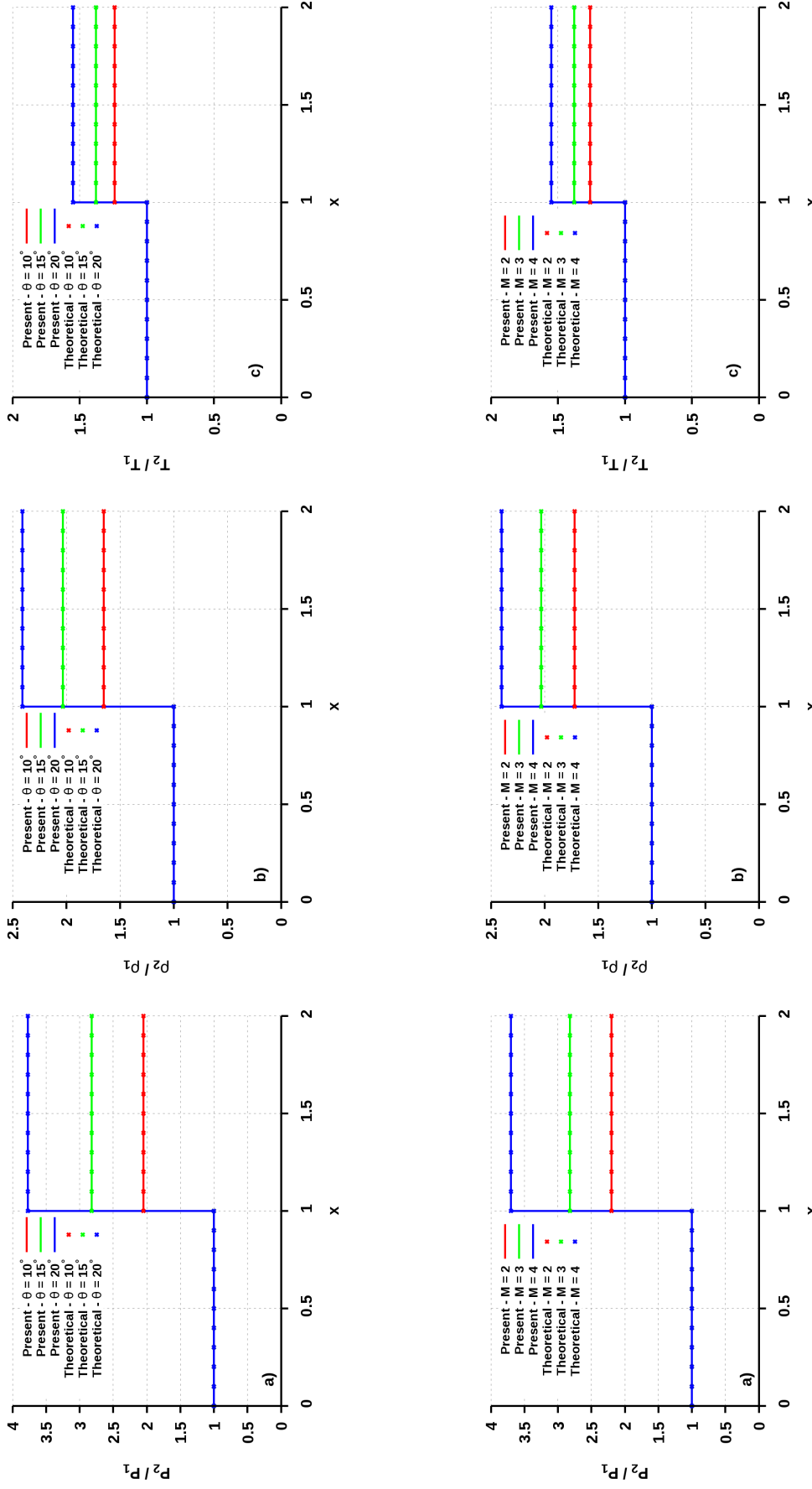
Figure 4.3: Pressure (a), density (b) and temperature (c) profiles. Top: Influence of the ramp angle at $Ma = 3$. Bottom: Influence of the Mach number for $\theta = 15°$.

The results obtained in the inviscid have fitted very well with the theoretical data. It was expected since the numerical difficulties mainly come from the introduction of solid walls that introduce strong velocity (and temperature) gradients. In order to check the ability of CHORUS to compute viscous supersonic flows in complex geometries, a reference case, dealing with the laminar flow around a compression ramp, will be considered in the next section.

4.2 Carter's case

The objective of this Ph.D. being the simulation of laminar flow in complex ramp geometries and in order to be sure that the code is working in that kind of configurations, a reference study has been searched to compare with CHORUS ' results. Unfortunately, pure laminar cases are very scarce since most researchers superimpose small perturbations to their laminar inflow profile, either to force the transition to turbulence [116] or to study the reaction of the flow to specific solicitations [112, 131, 132]. A NASA study [28] that perfectly matched the expectations and which was also used in a paper from Hung and MacCormack [79], has finally been found.

4.2.1 Flow configuration

In this case, the flow over a heated compression ramp at $\theta = 10°$ and $Ma = 3.0$ has been considered. The Reynolds number based on the freestream quantities and the position of the ramp corner x_c has been chosen such that $Re_{x_c} = 1.68 \times 10^4$. Sutherland's law has been used to model the variation of the viscosity with respect to the temperature and the fluid is supposed to verify the ideal gas law, with $\gamma = 1.4$ and $Pr = 0.72$.

The exact same domain and mesh as those defined in section 4.1 have been used in this case. Concerning the boundary conditions, all flowfield variables are specified at the inlet (leftmost) boundary, outflow conditions are applied on both the top and rightmost boundaries. The wall has been treated as isothermal ($T_w/T_\infty = 2.8$) and a no-slip condition has been applied.

4.2.2 Results

The streamwise evolutions of the pressure C_p and skin-friction C_f coefficients, defined by Eqs 4.1 and 4.2, are represented in Figure 4.4.

$$C_p = \frac{p_w - p_\infty}{p_\infty} \tag{4.1}$$

$$C_f = \frac{\tau_w}{\frac{1}{2}\rho_\infty U_\infty^2} \tag{4.2}$$

The comparison between the present DNS and the numerical results from Carter [28] and Hung & MacCormack [79] shows a very good agreement for the pressure, especially with Carter's data. A small discrepancy occurs around the corner in Hung and MacCormack's simulation but, as this undershoot also appears on the friction coefficient, it can be linked
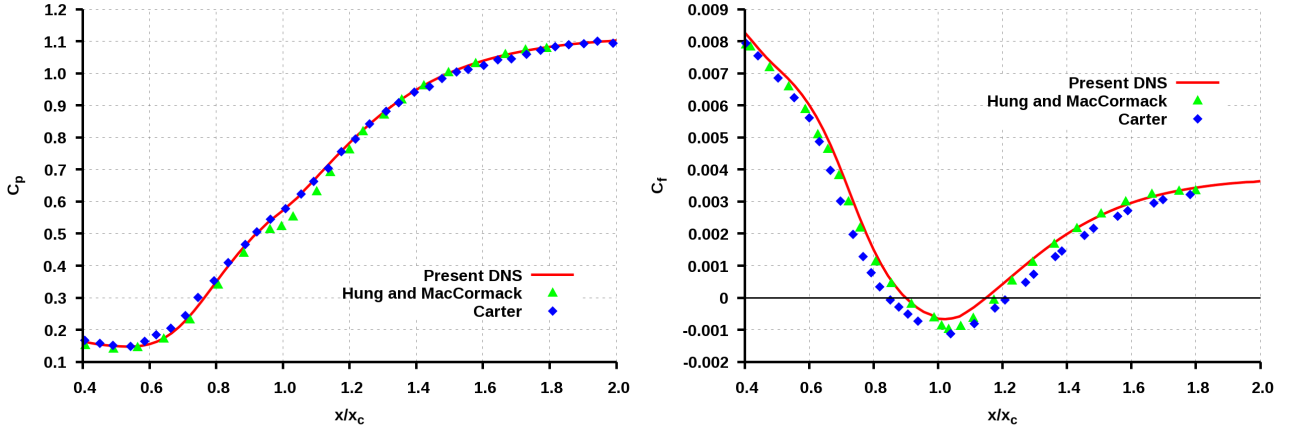
Figure 4.4: Streamwise evolution of the pressure (left) and skin-friction (right) coefficients.

to their simulations. The comparison on the friction coefficient is a little less good as far as Carter's results are concerned but better for Hung's. The underestimation of C_f by Carter can be explained by the use of a poorly chosen domain/mesh. Indeed, as it can be easily seen in Figure 4.5, the wall pressure is strongly dependent on the computational box and it is expected to be the same for C_f. Nevertheless, all the curves in [28] were obtained using box I, except Figure 4.4-left that used box IV. As a result, the following analysis will be more qualitative than qualitative.
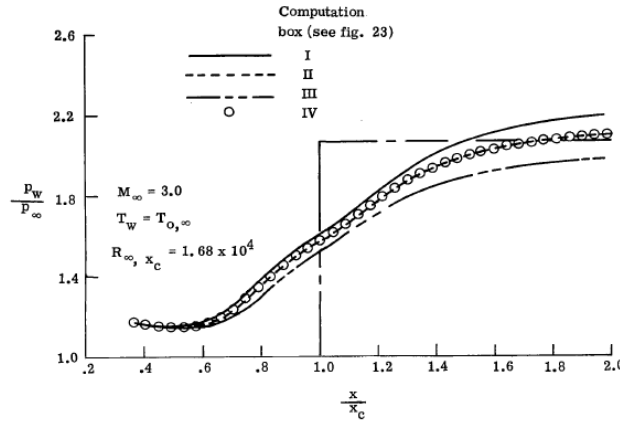
Figure 4.5: Influence of the computational box on the wall pressure evolution taken from [28]. Box IV is defined as the reference in Carter's report.

The density field is shown in Figure 4.6. In order to highlight the presence of the separation, streamlines are superimposed to the density field. The length of the bubble obtained by visualising the streamlines is similar to the value computed through the skin-friction coefficient $L_R = 0.25 \frac{x}{x_c}$. In his study, Carter found that the separation and reattachment occurred around $\frac{x_s}{x_c} = 0.84$ and $\frac{x_r}{x_c} = 1.22$ corresponding to a recirculation length $L_R = 0.38 \frac{x}{x_c}$. Once again, this discrepancy can be linked to Carter's under-resolution.
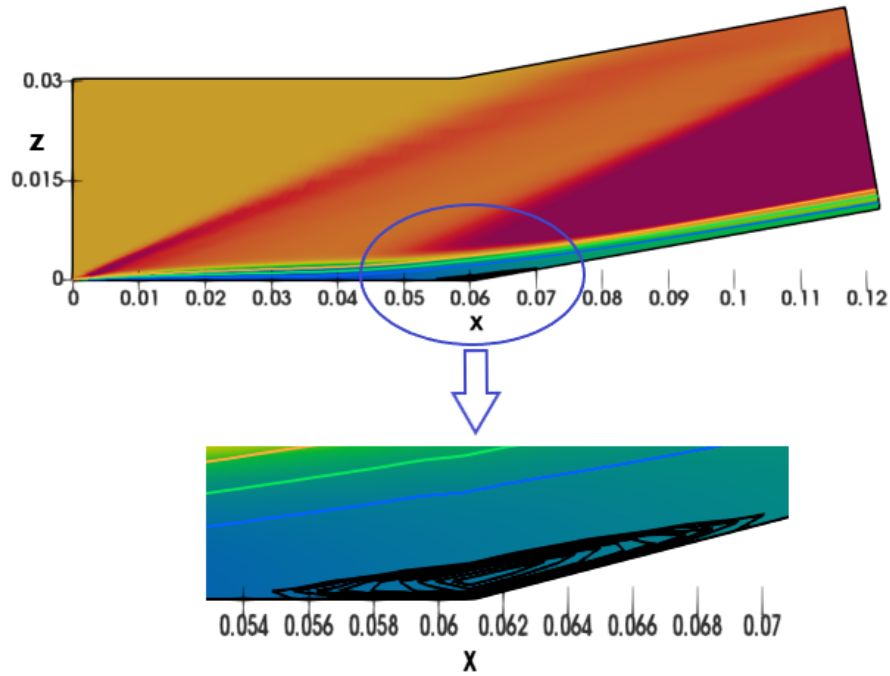
Figure 4.6: Density field and streamlines at $Ma = 3.0$ and $\theta = 10°$.

The influence of the ramp angle has also been analysed. The streamwise evolutions of the wall pressure and the density fields obtained for three different ramp angles ($5°$, $7.5°$ and $10°$) at $Ma = 3$ are plotted in Figures 4.7 and 4.8 respectively. The DNS results qualitatively agree well with the inviscid theory as well as the reference data. The shape of the wall-pressure profiles shows that, as predicted by the theory, a higher ramp angle leads to a higher pressure jump. If the subsequent adverse pressure gradient is high enough, the boundary layer separates and a recirculation region is then created. It is found that the boundary layer separates only for $\theta = 10°$ as expected from Carter's study.
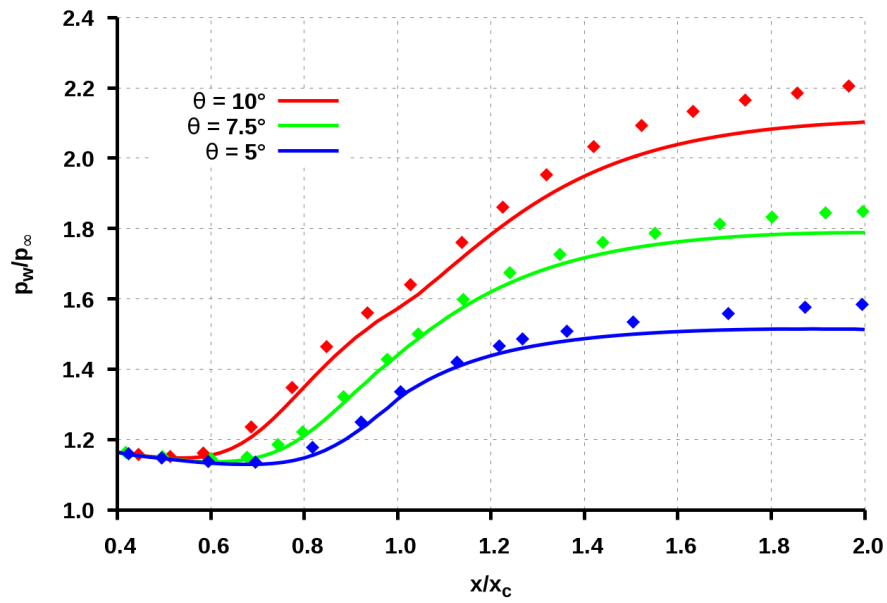
Figure 4.7: Streamwise evolution of the wall pressure for three different ramp angles at $Ma = 3$. Symbols come from [28].
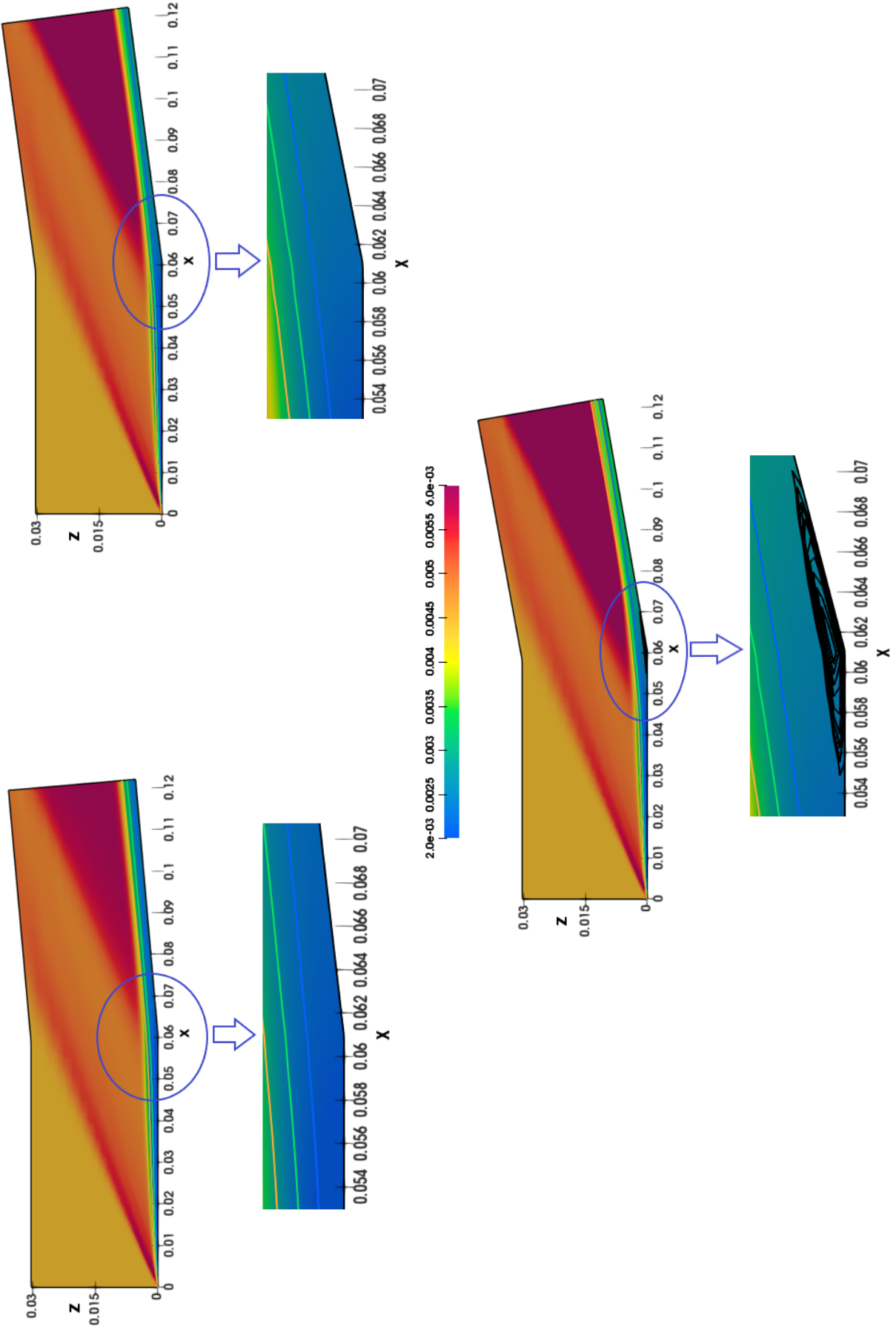
Figure 4.8: Density field and streamlines at $Ma = 3.0$ for three ramp angle: $\theta = 5°$ (upper left), $\theta = 7.5°$ (upper right) and $\theta = 10°$ (bottom). Zoom in the separation and no-separation regions.

The comparison with Carter's and Hung's studies have shown that the results obtained with CHORUS are in good agreement with reference data. However, those studies are rather old (the late 1970s) and a lot of progress has been made in numerical methods for high-speed flow simulations. Unfortunately, as it was mentioned earlier, there are very few (to say the least) recent studies concerning simulations or experiments of fully laminar flow around ramps or other complex geometries that could have helped to assess CHORUS' ability to compute such flows. It has then be decided to create our own test case, using a well-documented and well spread Open Source Solver: OPENFOAM .

4.3 OPENFOAM's case

In this section, one of the most-used and documented solver of the last decade is used to perform numerical simulations of a 2D compression corner flow, using the classical numerical methods of laminar Navier-Stokes equations resolution. A specific test-case has been created to compare with DNS results from CHORUS . The aim of this work is essential to highlight the classical numerical approach limitations to solve and capture the unsteady character of shockwave-boundary layer interaction flows. A brief description of the code is given. The computational domain, grid system and boundary condition are also described.

4.3.1 Numerical methods and code

The `rhoCentralFoam` solver of the OPENFOAM (Open source Field Operation And Manipulation) software package for compressible flows has been used to compute the steady laminar solutions of 2D compression corner flows. It is a finite volume, density-based, unsteady, time-accurate solver developed by Greenshields *et. al.* [67]. The presence of discontinuities, such as irregularities and contact surfaces in high-speed flows, requires specific numerical schemes that can fix these properties, avoiding spurious oscillations resulting from the presence of high gradients. In this regard, the Kurganov and Tamdor numerical scheme [93], a second-order both time and space accurate central scheme is implemented in the solver. It can provide accurate, non-oscillatory solutions. This solver has been successfully tested, and validated by a number of authors [166, 77, 52].

4.3.2 Computational domain and boundary conditions

The computational domain spans from $x = -4.2\ mm$ to $x = 4.2\ mm$ in the streamwise direction. The leading edge of the flat plate and the compression corner are located at $x = -4.2\ mm$ and $x = 0\ mm$ respectively. The required computational mesh, represented in Figure 4.9-left, is created by using the `blockMesh` utility of OPENFOAM . It is divided into 2 blocks, one upstream of the compression corner ($x < 0$) and the other one downstream of it. Each block contains 100×250 cells in the streamwise and wall-normal directions, respectively. To accurately capture the flow physics for a ramp-induced shockwave-boundary layer interaction, a specific care has been taken while generating the mesh to ensure a very fine grid where large gradients are encountered (leading edge, walls, and compression corner)
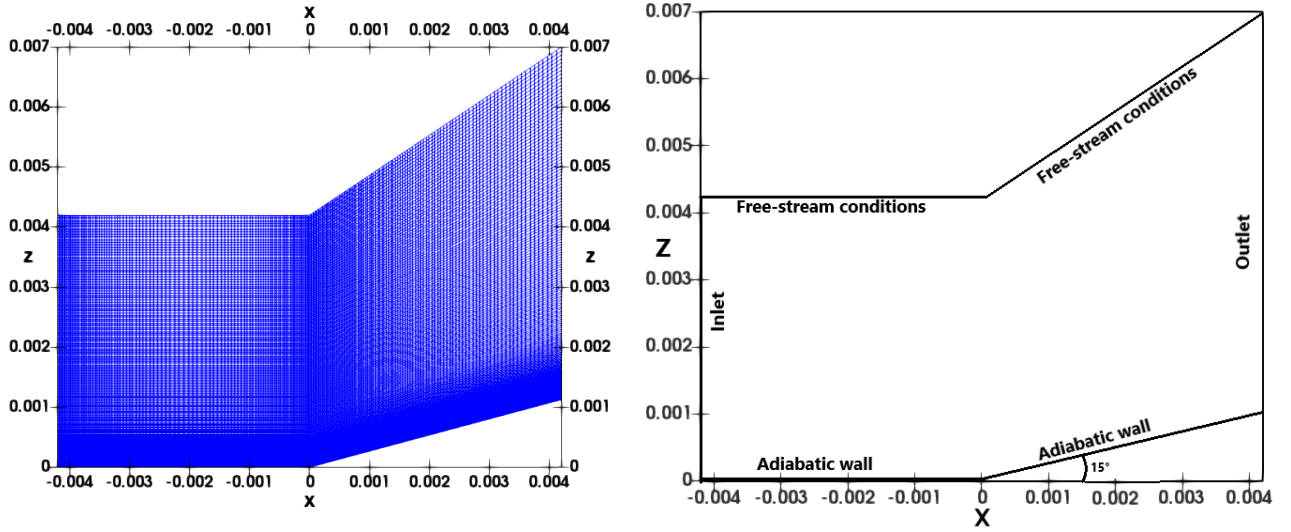
Figure 4.9: Illustration of the mesh (left) and boundary conditions (right) used in OPEN-FOAM

The boundary conditions used in OPENFOAM are represented in Figure 4.9-right. At the inlet and upper boundaries, all the freestream conditions ($Ma = 2.5$, $T = 288.15\ K$, $p = 82700\ Pa$ and $\rho = 1.0\ kg.m^{-3}$) are specified. on the left boundaries. A no-slip adiabatic wall condition is applied on the lower boundary. At the outlet, the flow variables are extrapolated from the inner values.

4.3.3   Results

Unlike with the simulations performed with OPENFOAM , the DNS results obtained by CHORUS are, by nature, unsteady. The flow also being unsteady, as it will be shown in Chapter 5, the DNS results used for comparison have been time-averaged. In order to ensure the quality of the averaging, a little less than $2{,}000{,}000$ samples have been taken, spanning from $T_{start} \simeq 45\ T_{FT}$ to $T_{end} \simeq 90\ T_{FT}$. T_{FT} is the so-called Flow-Through time that corresponds to the time it takes for a fluid particle to go from the inlet to the outlet boundary.

The Mach contours obtained with CHORUS and OPENFOAM are represented in Figure 4.10. A first glance at this figure does not reveal any significant differences between the two approaches. The separation zone, appearing in dark (since it is a zone of small velocity and therefore small Mach numbers), has the same global shape. In addition, All three expected shocks (leading edge, separation, and reattachment shocks) are recovered and have the same angles. When using CHORUS, however, a slight train of waves is observed upstream of the reattachment shock.

In order to compare more thoroughly the two codes, more quantitative analyses have been performed. The streamwise evolutions of the wall pressure and friction coefficient are shown in Figure 4.11. Except for small discrepancies, the results from both codes are in good agreement with each other. Before the separation $\left(\dfrac{x}{x_c} < 0.2 \right)$, the wall pres-
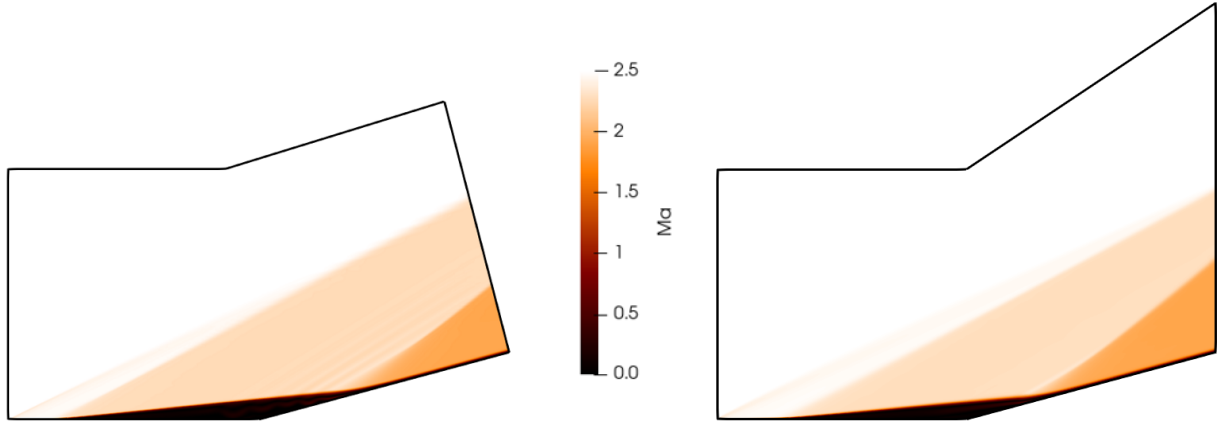
Figure 4.10: Mach contours obtained with CHORUS (left) and OPENFOAM (right).

sure is exactly the same for both cases, demonstrating that the flow and boundary conditions are correct. In the separated zone $\left(0.5 < \dfrac{x}{x_c} < 1.2\right)$, and after the reattachment $\left(\dfrac{x}{x_c} > 1.6\right)$, the values of the plateaux of wall pressure are very close. The main differences concern the location of the separation and reattachment points, the recirculation zone being slightly larger when the flow is computed using CHORUS .
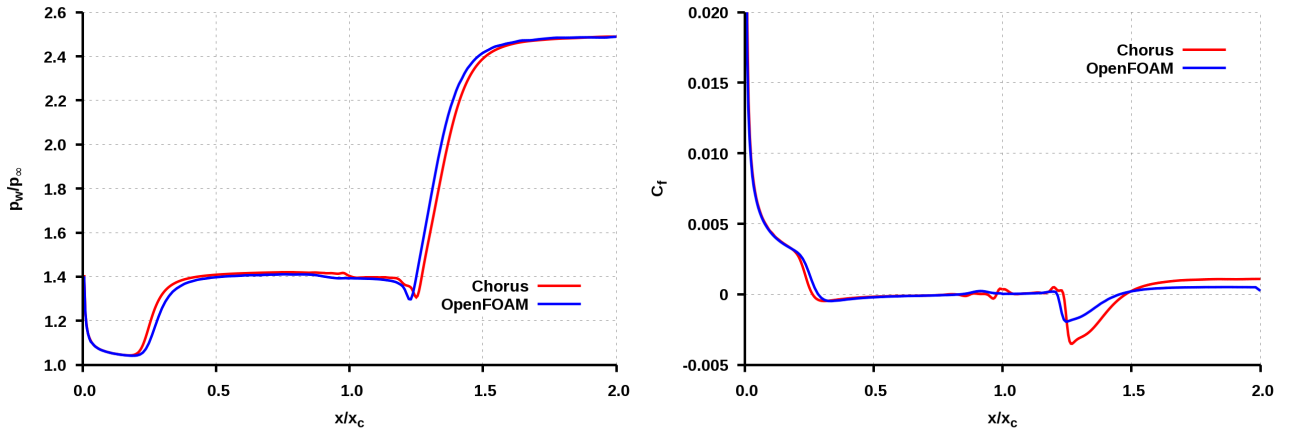
Figure 4.11: Streamwise evolution of the wall pressure (left) and skin-friction coefficient (right).

With respect to the friction coefficient, the differences are slightly bigger, especially for $1.2 < \dfrac{x}{x_c} < 1.5$ which corresponds to the region just at the end of the recirculation bubble, and around the reattachment point. Even if C_f is globally identical up to $\dfrac{x}{x_c} = 1.2$, they evolve in two rather different fashions downstream.

Two phenomena can explain that discrepancy. The first one is strongly related to the physics of the flow. As one will see in chapter 5, the flow conditions are such that the

boundary layer transition occurs in the shear layer just above the separation bubble. Therefore, 3D vortices are shed in this layer and will evolve into hairpin vortices after the reattachment. The flow is highly-3D and then, it cannot be accurately predicted using 2D simulations. Many studies ([23, 58, 109]) have indeed shown that the dynamics of the separation bubble is not recovered when using 2D-simulations and, worse, that non-physical vortices are created in order to tackle the impossibility for the flow to go in the non-existent spanwise direction.

The second phenomenon has to do with the different techniques implemented in the codes. When using OPENFOAM, the steady version of the Navier-Stokes equations is solved until a steady-state is reached. On the other hand, CHORUS solves the unsteady Navier-Stokes equations, and then, time-averaging is performed. In the case of nominally unsteady flows such as the case considered here, it is well known that those two solutions are not the same and may significantly differ from one another (See [101] for example). As a consequence, and since the flows computed are not exactly the same, the wall pressure and friction coefficient should not be identical.

Those two phenomena can be seen in Figure 4.12, representing the negative contours of the streamwise velocity in the separation bubble for both simulations. It clearly appears that the flow in the separation bubble is not exactly the same for both approaches due to their inherent differences. In addition, the wavy pattern of the contours obtained with CHORUS evidence the presence of the non-physical vortices as discussed earlier. It is noteworthy that those oscillations are responsible for the train of shock that can be seen in Figure 4.10. Moreover, because of the very long integration time used for the time-averaging, those structures are not due to a lack of convergence in the time-averaging process.
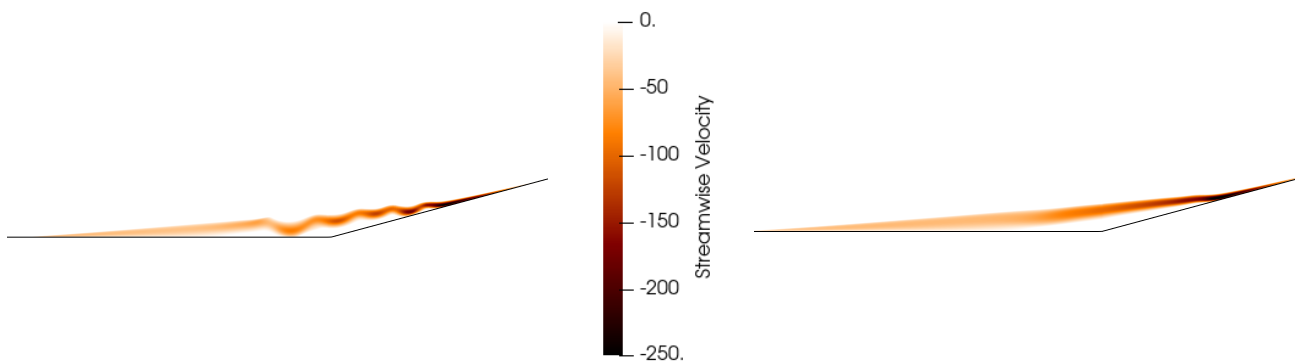
Figure 4.12: Negative streamwise velocity contours obtained with CHORUS (left) and OPENFOAM (right) in the recirculation zone.

For all those reasons, a perfect match should not be sought between the simulations using CHORUS and OPENFOAM, but rather a concordance in the observed behaviour. Consequently, it seems that under those conditions, the two approaches are in very fair agreement and this indicates that CHORUS is perfectly able to be used for simulating the flow in complex geometries.

4.4   Influence of Orthogonality

As shown in chapter 3, the matter of mesh orthogonality is of crucial importance and has to be assessed when dealing with ramp configurations. A quick bibliographic study on simple compression ramps showed that there is no consensus in the scientific community whether the mesh should be orthogonal to the wall or not. For example, Non-orthogonal meshes were used in [28, 79, 41, 82] while [2, 125, 104, 119, 97] considered orthogonal (or quasi-orthogonal) cells. In the more complicated case of compression-expansion (or expansion-compression) ramps, however, and for the sake of simplicity, only non-orthogonal meshes have been encountered [68, 57, 121].

The influence of the mesh orthogonality being highly numerical methods- and more globally code-dependent, a preliminary study has been performed in the Carter test-case presented in Section 4.2. Both mesh configurations are shown in figure 4.13. The number of points, resolution, and dimensions of the domain were kept identical for each case and only the way cells are created was changed. As the so-called orthogonal mesh is not perfectly orthogonal, in particular in the flat plate region, it will be referred to as quasi-orthogonal.
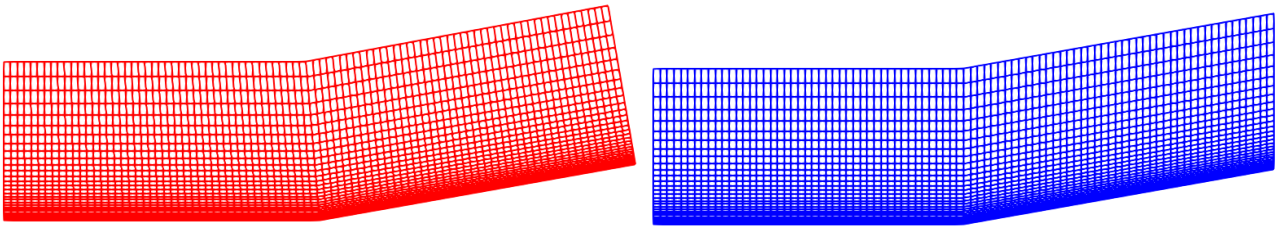
Figure 4.13: Representation of the quasi-orthogonal (left) and non-orthogonal mesh (right) configurations.

The comparisons between the pressure and skin-friction coefficients for both mesh configurations are shown in figure 4.14-left and 4.14-right, respectively.
As far as the ramp configuration is concerned, no noticeable differences are found between the two meshes. Therefore the orthogonality seems to only have a very small influence on the computations and either mesh could be chosen confidently. As a result, in the following chapter, quasi-orthogonal and non-orthogonal meshes will be used for the single ramp case and compression-expansion corner, respectively.

4.5   Conclusions

In the present section, Chorus has been used to simulate the flow around a compression corner. Three different configurations have been considered, namely the inviscid case, the Carter case, and a special configuration used for validation with OpenFOAM . All the presented results have demonstrated the capabilities of the code to accurately predict the flow around a compression corner, validating both the numerical approach and the grid generation technique. As a consequence, the code will be, from now, considered
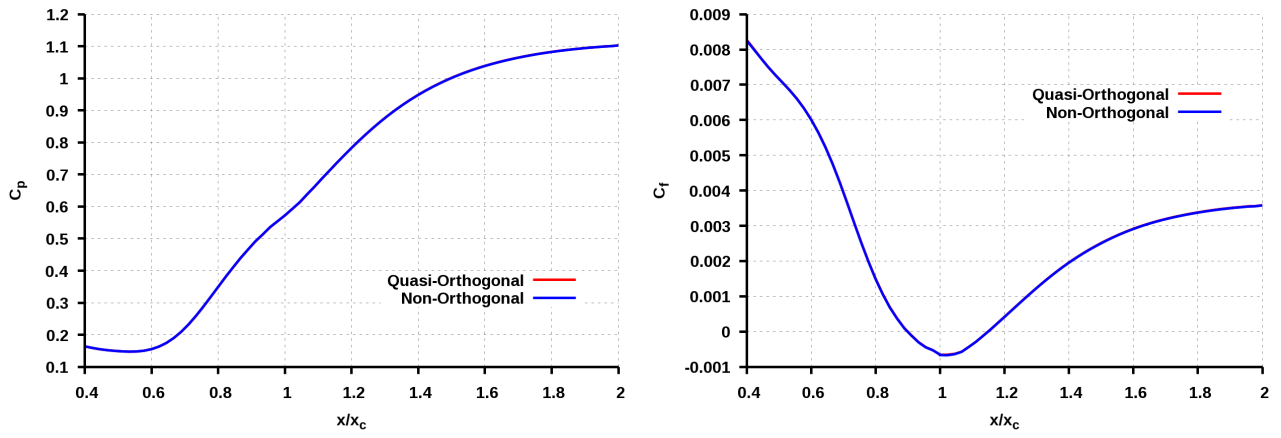
Figure 4.14: Streamwise evolutions of the pressure (left) and skin-friction (right) co-efficients for the non-orthogonal and quasi-orthogonal meshes in the Carter test-case configuration.

as validated and innovative trustworthy DNS will then be presented in the following chapter.

Chapter 5

Physical analysis of the flow over compression corners

Contents

In this chapter, the results from Direct Numerical Simulations will be presented for two different complex geometries: a classical compression ramp and a double ramp configuration, known as a Compression-Expansion ramp. The main objective of those simulations is to determine whether, in the laminar regime, the separation bubble is subjected to a low-frequency longitudinal motion as observed in the turbulent case [120, 69, 68]. For the interaction between an oblique shock wave and a flat plate, a very recent study [14] has demonstrated that this motion is not recovered in the laminar regime while it is present in the turbulent case. This study will try to show if it is also the case in the ramp configuration. The case of the ramp has been chosen to test the code's ability to tackle complex geometry, and because the unsteadiness of the separation bubble has been shown to be independent from the source of the SWBLI [32].

5.1   Dynamics of the recirculation bubble

As stated in Chapter 1, separation can occur if the Mach number and/or the ramp angle (or shock angle, in the case of the interaction between an oblique shock wave and a flat

plate) are high enough, leading to the creation of a recirculation bubble (Figure 5.1), referred to as RB in the following sections.

The dynamics of the separation bubble is actually very complex and not fully understood. To roughly summarize, three main unsteady phenomena take place inside the bubble. Two of them are related to the dynamics of the shear-layer just upstream of the reattachment point: the *vortex shedding* and the *flapping*. Because of the differences in velocity between the flows inside (low velocity) and outside (high velocity) of the RB, a Kelvin-Helmholtz instability occurs in the shear layer which leads to the formation of spanwise vortices (represented by the green spiral in Fig. 5.1). The frequency associated to this phenomena is $St_s = \dfrac{f\,L_R}{U_\infty} \simeq 0.5 - 0.6$, L_R being the length of the RB and U_∞ the velocity outside of the boundary layer. In addition, it has been evidenced [31, 88] that the *vortex shedding* does not occur at the same position but that it is subjected to a vertical *flapping* at $St_f \simeq 0.12 - 0.15$, as shown by the blue arrow in Figure 5.1. Finally, a third, more global phenomenon has been observed by Piponniau *et. al.* [115]. According to the authors, the entrainment in the shear layer is responsible for what they called the *breathing* of the separation zone: successive periods of enlargement and shrinkage happening at a very low frequency $St_b \simeq 0.03 - 0.04$ (pink arrows in Figure 5.1). This flow dynamics is rather universal and is verified either in incompressible or compressible flows.
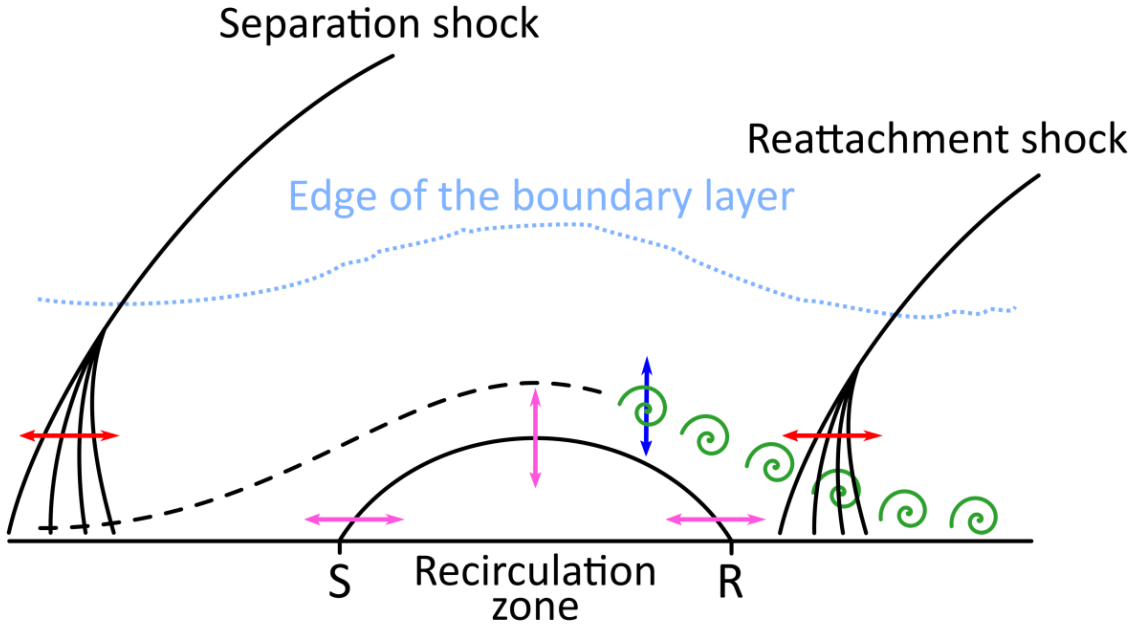
Figure 5.1: Sketch of the separation bubble for compressible flows. The four main unsteady phenomena are highlighted: *shedding* (green), *flapping* (blue), *breathing* (pink) and oscillations of the shock system, known as the unsteadiness of the RB (red). Adapted from [115].

In the framework of shockwave-boundary layer interactions (therefore compressible), a fourth phenomenon, known as the *unsteadiness of the separation bubble*, represented by red arrows in Figure 5.1, has been observed by several studies, either experimental [51] or numerical [11, 116, 153]. It is indeed well known that, when considering an in-

coming turbulent boundary layer, the separation shock just upstream of the RB as well as the reattachment shock are subjected to low-frequency streamwise oscillations occurring at $St_u \simeq 0.03 - 0.04$. Although the physical origins of those oscillations are still unknown, they have been linked to two potential causes: the bubble dynamics, and more specifically the *vortex shedding* in the shear layer [11, 120], and the structures in the incoming boundary layer [64]. The conclusions from Ganapathisubramani *et. al.* having been mitigated by several studies [50, 154] and the oscillation frequency St_o being very close to the *breathing* frequency St_b, the bubble dynamics seems to be the best candidate.

As stated before, the goal of this study is to improve our knowledge on the RB oscillations. Hence, in order to conclude in a more accurate fashion, only laminar incoming boundary layer, in which no vortical structures are present, will be considered. The aim is therefore to suppress one of the two suspected causes for the shock oscillations and check whether the low-frequency longitudinal motion still occurs.

5.2   Compression Ramp

5.2.1   Flow parameters

In this chapter, the laminar flow around a compression corner and a compression-expansion ramp (referred to as `SingleRamp` and `CompExp` in the following, respectively) has been considered. The freestream conditions are gathered in table 5.1.

Parameter	Value
Ma_∞	2.5
$U_\infty \ (m.s^{-1})$	850.7
$p_\infty \ (Pa)$	82,700
$\rho_\infty \ (kg.m^{-3})$	1.2
$T_\infty \ (K)$	288.15

Table 5.1: Freestream conditions used in the `SingleRamp` and `CompExp` cases.

In the `SingleRamp` case, the domain spans over $8.4 \ mm$, $4.2 \ mm$ and $2.1 \ mm$ in the streamwise, spanwise and wall-normal direction, referred to as x, y and z, respectively. The corner is located at $x_c = 4.2 \ mm$. In order to stay far away from the known value of the transition Reynolds number $Re_t = 3.15 \times 10^6$ [34], the Reynolds number based on the corner location is taken such that $Re_c = 200,000$. Finally, in a numerical point of view, $CFL = 0.5$. All the parameters are the same for the `CompExp` geometry, except for the domain that is twice as long ($L_x = 16.8 \ mm$) and where the compression and expansion corner are located at $x_c = 4.2 \ mm$ and $x_e = 8.4 \ mm$, respectively.

5.2.2   Mesh Convergence

Before starting the physical analysis of the flow in the `SingleRamp` configuration, a study on the mesh convergence has been performed. Three different meshes have been consid-

ered and their parameters are gathered in table 5.2. The resolution in the wall normal direction, with around 60 CVs in the boundary layer (at the end of the domain) and $\Delta z_w^+ = 0.7$ is state-of-the-art when dealing with DNS [116]. As a consequence, only the streamwise and spanwise resolutions have been varied. It is noteworthy that the friction velocity u_τ, used to compute the wall units, has been evaluated at the end of the computational domain.

Mesh Name	$N_x \times N_y \times N_z$	Δx^+	Δy^+
M_1	$400 \times 200 \times 100$	**29**	**29**
M_2	$640 \times 320 \times 100$	**20**	**20**
M_3	$800 \times 400 \times 100$	**17**	**17**

Table 5.2: `SingleRamp`: Mesh parameters used for the mesh convergence study.

A comparison of the results obtained for the three meshes is shown in Figure 5.2. It is clear from all three pictures that M_1, being away from M_2 and M_3 in each case, is clearly under-resolved. The largest differences are observed on the friction coefficient, where the size of the RB is overestimated (the separation happens earlier and the reattachment later) and where the value of C_f is highly underestimated for $\dfrac{x}{x_c} > 1.2$. It is not a surprise per say since this quantity is very sensitive to the grid resolution and a fine mesh should be use if one wants to accurately compute it. Even if the tangential velocity and wall pressure profiles are in fairly good agreement with those obtained for M_3, M_1 has been ruled out of the study for being too coarse. An intermediate mesh M_2 has then been considered and its results are in very good agreement with M_3 for all quantities, even if C_f is slightly under-resolved in the final part of the ramp. Therefore, M_2 seems to be a good candidate for our study.

However, and as it will be shown later, the flow conditions considered here are such that the boundary layer undergoes its transition towards turbulence somewhere upstream of the reattachment point. It, therefore, seemed interesting to assess the performances of M_2 in the framework of turbulent flows. For this kind of analysis, it is customary in the Fluid Mechanics community to consider the Reynolds stresses tensor $\overline{u_i' u_j'}$, obtained thanks to the Reynolds' decomposition, introduced by Osborne Reynolds in 1895 [123]. In that formalism, each instantaneous quantity $f(x, y, z, t)$ can be written:

$$f(x, y, z, t) = \overline{f}(x, y, z) + f'(x, y, z, t) \tag{5.1}$$

where $\overline{f}(x, y, z)$ is the ensemble average of the quantity f and $f'(x, y, z, t)$, its fluctuating part defined such that $\overline{f'} = 0$. In turbulence theory, the instantaneous signals can trustfully be considered as ergodic which enables the physicists to use the more convenient time average rather than the ensemble average. Because of the many properties of the averaging operator, the Reynolds stresses tensor can then be defined as:

$$\overline{u_i' u_j'} = \overline{u_i u_j} - \overline{u_i}\ \overline{u_j} \tag{5.2}$$

with i and j, two components of the velocity field. The entire mathematical and physical development can be found in [149]. A common usage is to plot the wall-normal profiles
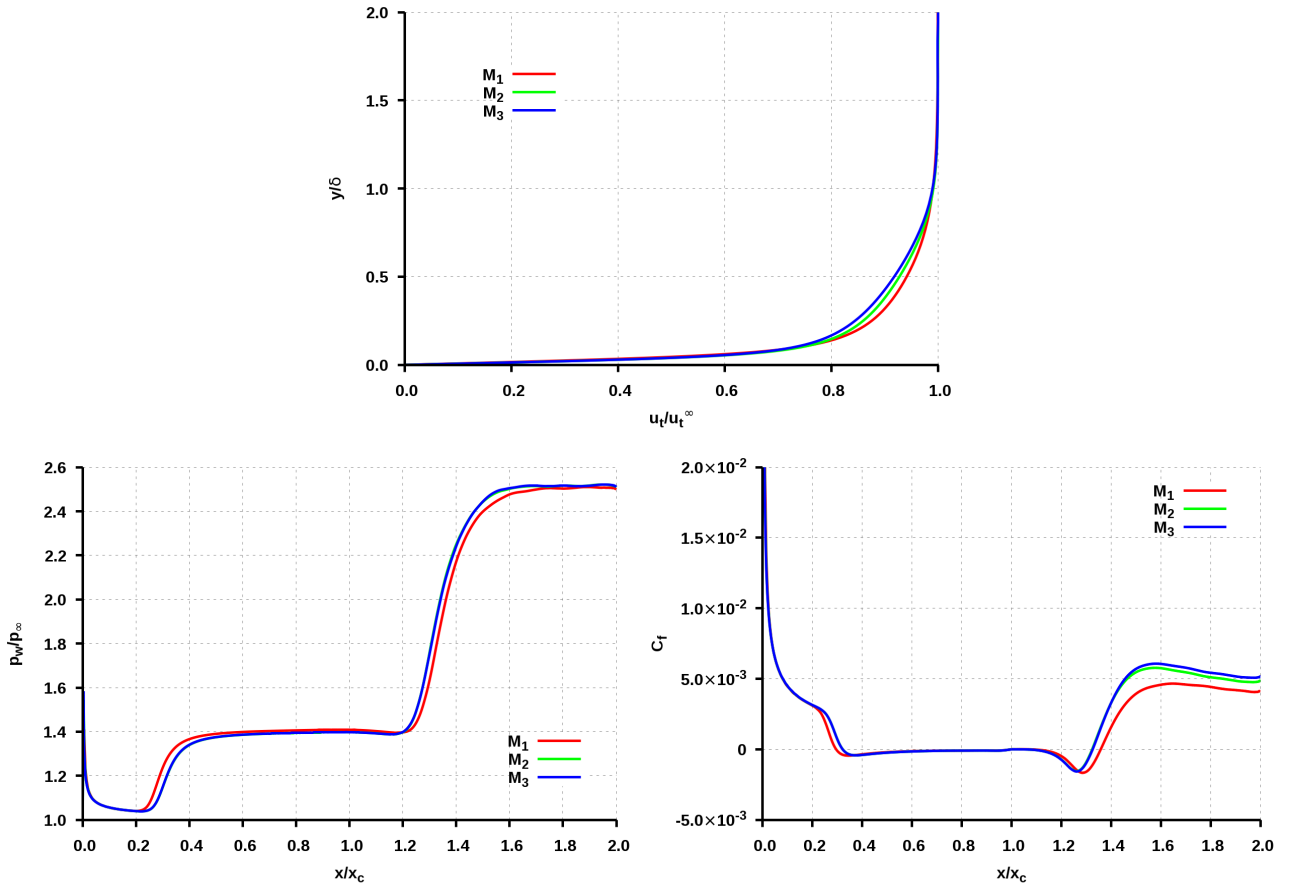
Figure 5.2: `SingleRamp`: Wall-normal profile of the tangential velocity u_t at $x = 8.4\ mm$ (top), Streamwise evolution of the spanwise-averaged wall-pressure (bottom-left) and friction coefficient (bottom-right) for three different meshes.

of the normalized density-scaled Reynolds stresses R_{ij} such that:

$$R_{ij} = \frac{\overline{\rho}\ \overline{u_i' u_j'}}{\overline{\rho}_w\ \overline{u_\tau^2}} \tag{5.3}$$

The extraction line for the profiles is highlighted by a white line in Figure 5.3, representing the time-averaged streamwise velocity field. It is located a few boundary layer thickness upstream of the reattachment point, in the recirculation zone, where a strong *vortex shedding* occur (Cf. Fig. 5.5).

The subsequent profiles are plotted in Figure 5.4 for the three meshes, M_1 being kept as a low-resolution reference value. Qualitatively speaking, the three meshes give very similar profiles for all the considered Reynolds stresses. The shapes of the profiles are very close, the peak in each case happens at almost the same position and their amplitudes are quite comparable. As expected, due to the under-resolution, the results for M_1 are not as good as those obtained with M_2, meaning that the turbulent features of the flow need a high enough resolution to be captured, that is not provided by M_1. A close look at the differences between M_2 and M_3 shows that M_2 could be a little under-resolved as well, which would explain the discrepancy observed for the friction coefficient (Fig. 5.2).
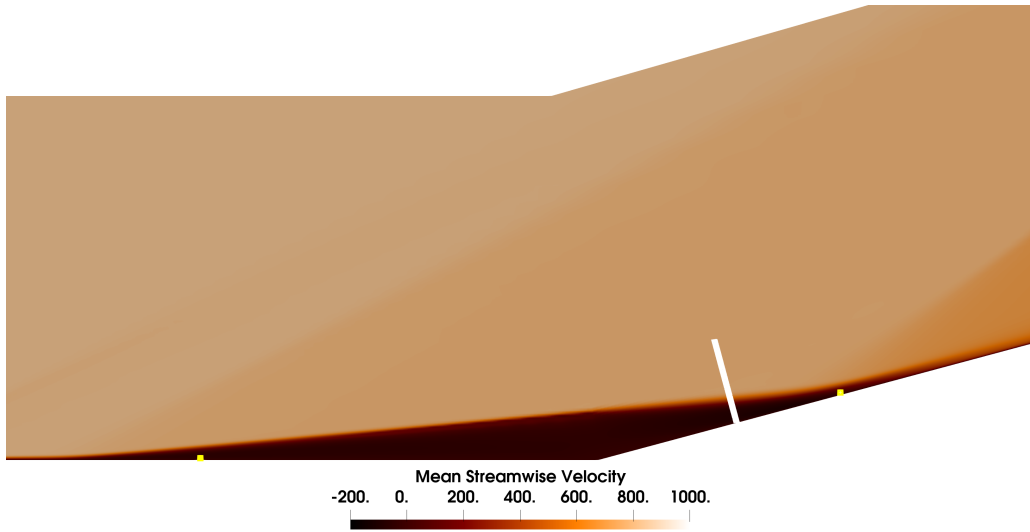
Figure 5.3: `SingleRamp`: Time- and spanwise-averaged streamwise velocity field showing the extraction line (white) for the $\overline{u_i' u_j'}$ profiles. The two yellow points are the location for the probes used in section 5.2.3.3.
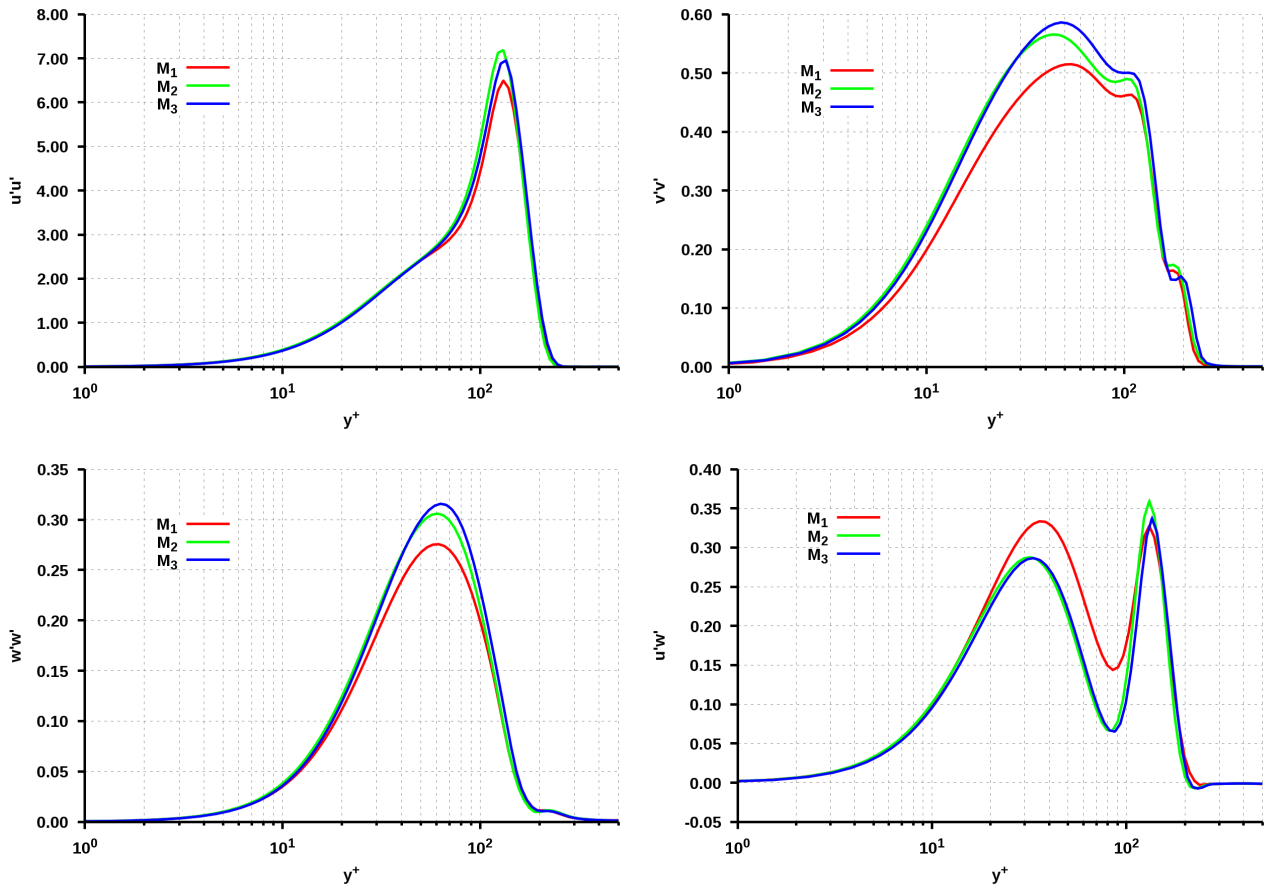
Figure 5.4: `SingleRamp`: Comparison of the normalized Reynolds stresses taken at $x = 0.005\ m$ for three different meshes.

In addition to the accuracy of the simulations, however, another important parameter for

the choice of a suitable mesh is the computational time. This study has benefited from a GENCI grant for the last four years and has consequently been granted several hundred thousand CPU hours on IDRIS' supercomputers. At the beginning of this Ph.D, only ADA was available. Its architecture was such that a maximum of 64 nodes could be efficiently used for the computations. In spite of its rather good performances (10^{-7} $s/CV/\Delta t$ for 64 nodes) a whole simulation on M_1 took around 800 clock-hours, corresponding to approximatively a month and a half (including the queue time), to be completed. The same simulations for M_2 and M_3 would then have taken 4 and 6 months respectively. As a consequence, all the computations were initially performed on M_1, the other options being too expensive. Fortunately, at the end of 2019, ADA has been shut down and replaced by JEAN-ZAY. It has been a really big improvement since, on this server, the code has shown a very good scalability up to 2048 nodes and the length of the computations has been steeply decreased. Only two weeks are indeed needed for the whole simulation, either on M_1 (using 512 nodes), M_2 (1024 nodes) or M_3 (2048 nodes). In order to improve the quality of this study, it was then decided to perform the convergence study presented here and rerun all the simulations initially performed on M_1, on the better-suited mesh M_2. Even if the results are not exactly the same as those obtained with the finer mesh M_3, they are very close and the needed resources are more than twice smaller than for M_3.

As a conclusion, the convergence study has shown that a minimal resolution is needed in order to compute accurately the more difficult-to-catch quantities such as friction coefficient and Reynolds stresses. The computational resources allocated to this study not being inexhaustible, it was decided to use the M_2 mesh for future computation since it presents a very good compromise between accuracy and computational time.

5.2.3   Results

Provided the discussion held in the last section, all the following results have been obtained with $640 \times 320 \times 100$ CVs in the streamwise (x), spanwise (y), and wall-normal (z) directions respectively. A regular mesh has been used in both the x and y directions and the cell sizes are such that $\Delta x^+ = \Delta y^+ = 20$. However, in the wall-normal direction and in order to save computational time, a power-law stretching has been applied, leading to $\Delta z_w^+ = 0.7$. Out of the 100 CVs used in the z direction, more than 55 are gathered in the boundary layer (at the end of the computational domain), which ensures a very accurate representation of the flow in this region of particular interest.

The aim of the present study being to evidence the existence (or the non-existence) of low-frequency oscillations undergone by the shock system and the recirculation zone, it is mandatory to consider very long integration times if one wants to capture those low frequencies. Consequently, the simulations have been run for around 135 Flow-Through times and the time-averaging has been performed on the last 32. In addition, all the time-averaged variables have also been spanwise-averaged.

5.2.3.1   Instantaneous fields

An example of the vortical structures can be found in Figure 5.5. They are evidenced using the Q-criterion, initially defined by Hunt *et. al.* [81] and discussed in [74]. The
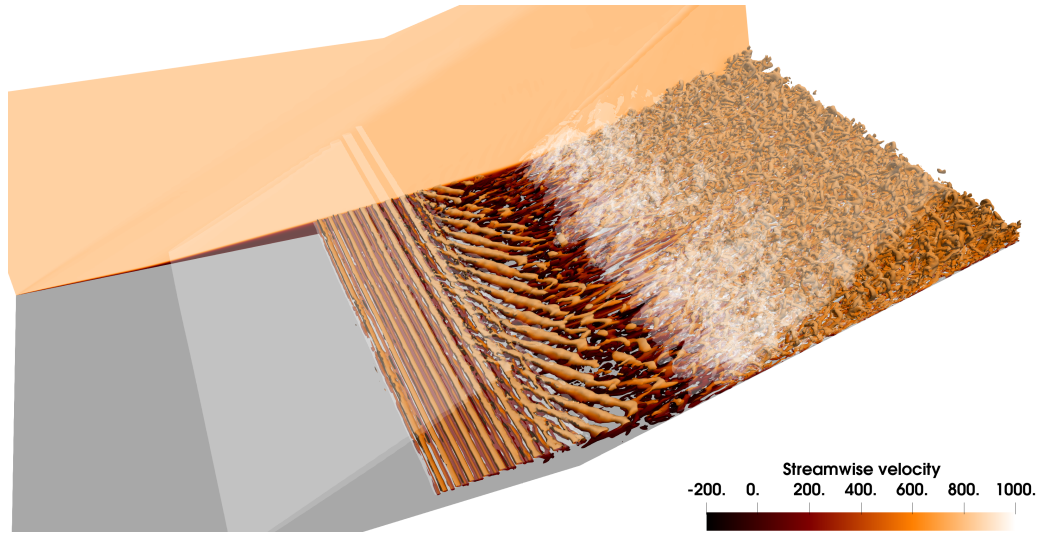
Figure 5.5: `SingleRamp`: Vortical structures evidenced by the Q-criterion, coloured by the streamwise velocity. The shock system is highlighted by isosurfaces of $div\ \mathbf{u}$.
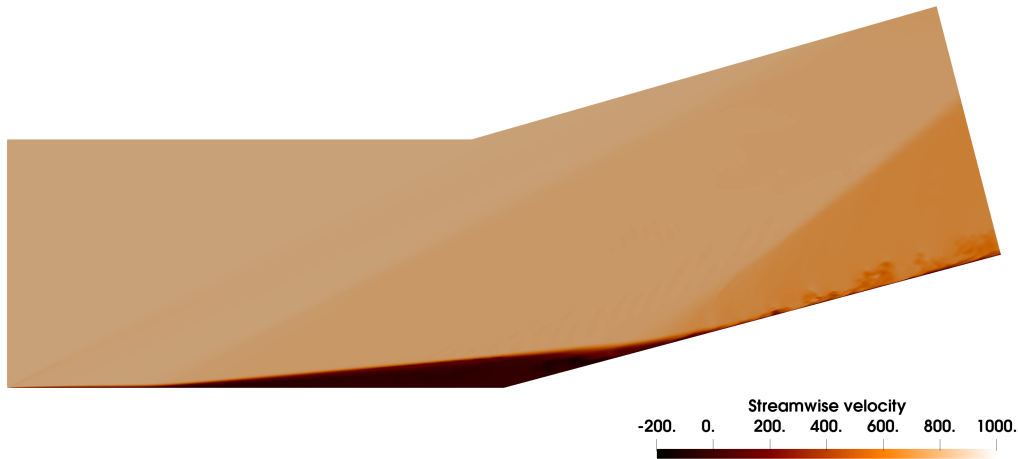
Figure 5.6: `SingleRamp`: Instantaneous field of streamwise velocity in the y_{max}-plane clearly showing the extent of the separation bubble (dark brown area).

instantaneous streamwise velocity field in the y_{max}-plane has been added to highlight the extent of the separation zone and is repeated in figure 5.6 for clarity. Isosurfaces of $div\ \mathbf{u}$ are finally used to show the shock system. As expected, the ramp angle-Mach Number combination leads to the creation of a large recirculation bubble. This bubble is bounded by two shocks: the perfectly 2D separation shock upstream and the highly 3D reattachment shock downstream. Initially, and because of the laminar aspect of the incoming boundary layer, no vortical structures are encountered. Under the influence of the separation shock, and the subsequent adverse pressure gradient, the separated boundary layer undergoes its transition to turbulence before the compression corner. That transition starts with the shedding of almost perfectly spanwise aligned vortices, that will progressively fade and switch to an oblique mode of transition and eventually form hairpin vortices, characteristics of wall turbulence.

The evolution of the shed vortices, going from 2D rollers to highly 3D structures, can be emphasised by extracting a numerical schlieren visualisation from the shedding plane (Fig. 5.7). This technique, defined by $S(x,y) = 0.8 \, exp \left(-15 \dfrac{|\nabla \rho|}{|\nabla \rho|_{max}} \right)$ was first introduced by Hadjadj and Kudryavtsev [71].
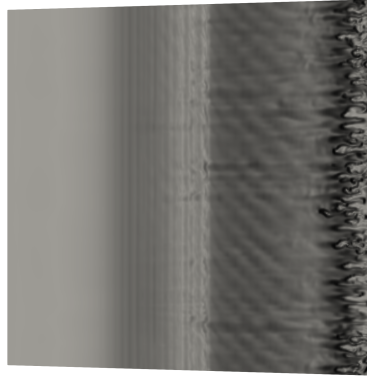
Figure 5.7: `SingleRamp`: Top view of the instantaneous numerical schlieren [71] extracted in the shedding plane.

At first, this oblique shedding was thought to be a numerical artefact. However, a comparison of the results obtained from M_1, M_2 and M_3 has demonstrated that this phenomenon is mesh-independent (Figure 5.8).
Even if the physical origin of this phenomenon is not clear, it seems that it should be sought on the side of the main modes of transition in compressible mixing layers [130] or of the oblique shedding observed in the case of a circular cylinder [160] rather than of the shifting of the Tollmien-Schlichting waves in a boundary layer [16], at least by the fact that a separated boundary layer, with its subsequent shear layer, is closer to a wake than to a non-separated boundary layer.

The time allocated to this thesis coming to its end, it has been decided not to investigate this phenomenon further. However, it is of great interest and should definitely be pursued in the future in order to increase our knowledge of boundary layer transition in separated flows.

Another interesting phenomenon that has been evidenced by those Direct Numerical Simulations is the presence, in the flow, of some kind of vorticity-free patches. In a fully turbulent boundary layer, the vortices uniformly exist everywhere. On the opposite, the transition from a laminar to a turbulent boundary layer happens through the creation of vorticity spots, first described by Emmons [55] and observed by Cantwell *et. al.* [27] (Figure 5.9).
In the present study, it has been evidenced that, for the considered Mach number and ramp angle, the transition occurs in the shear layer just upstream of the separation. As a consequence, it is expected that a quasi-turbulent boundary layer would reattach and develop along the ramp. Figure 5.10 however shows that the shedding is not uniform around the reattachment point but instead, some large zone of structure-free flow can occur every once in a while. This phenomenon is of practical interest because it introduces
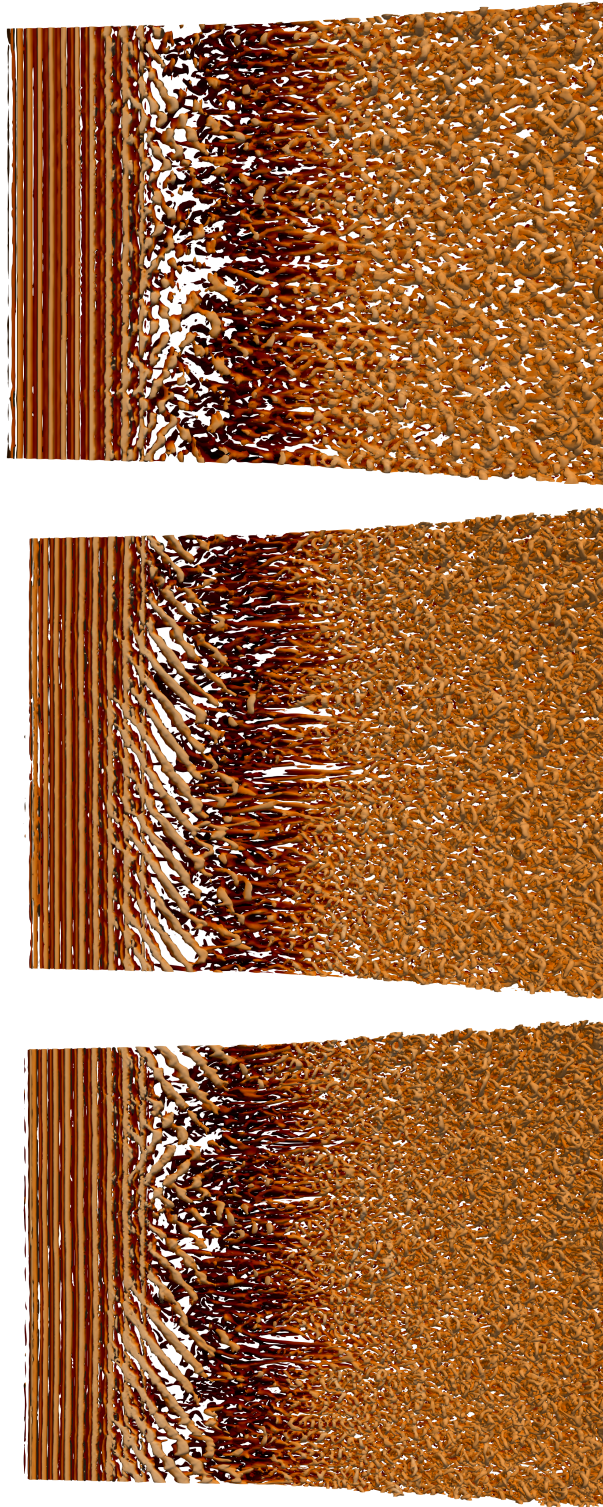
Figure 5.8: `SingleRamp`: Top view of the vortical structures obtained with three different meshes. Top: M_1, Middle: M_2 and Bottom: M_3. It is noteworthy that the transition occurs slightly earlier for M_1 than for the other two meshes.
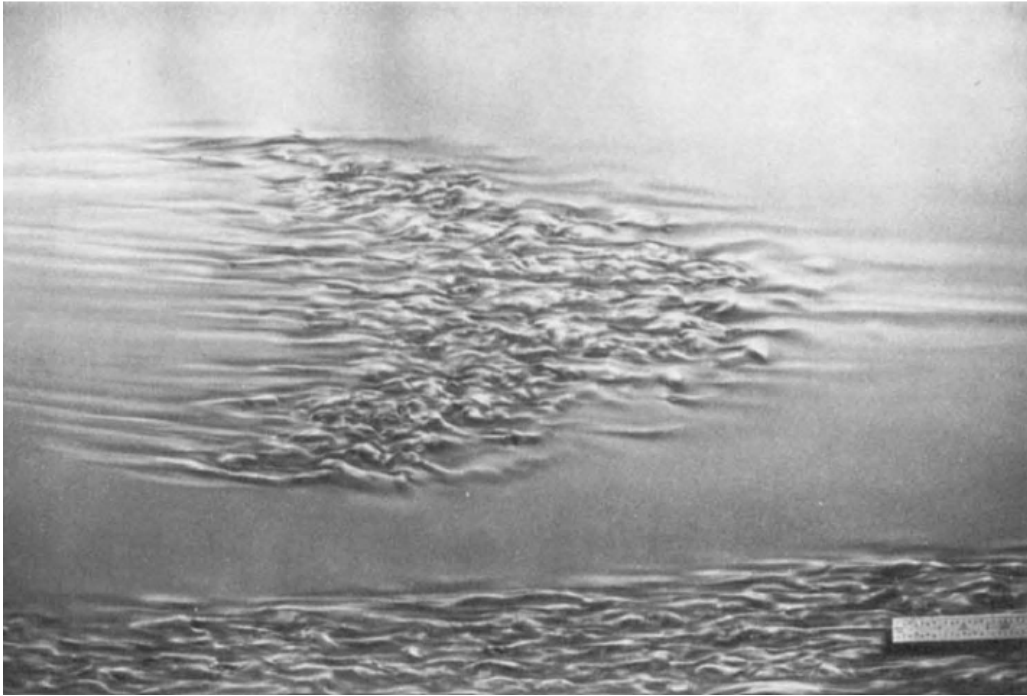
Figure 5.9: Visualisation of a turbulent spot in a transitional boundary layer (From [27]).

another highly-3D aspect to the flow and, more importantly, an additional low-frequency phenomenon that could possibly interact with the *breathing*, the *flapping* or the *vortex-shedding* [59]. Unfortunately, no physical explanation could have been found during the present study and further simulations will be undergone in the near future to tackle that problem.
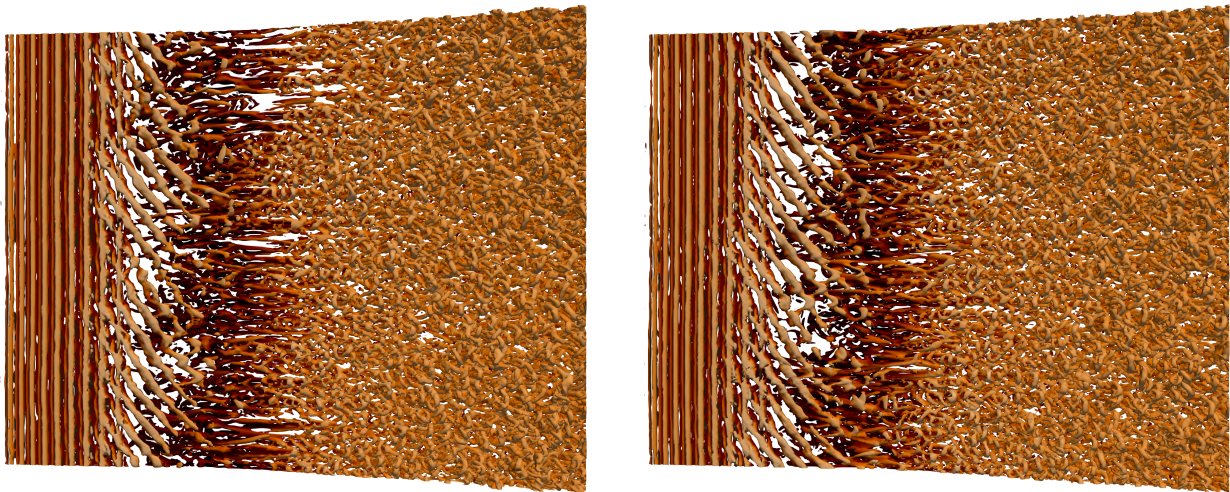
Figure 5.10: `SingleRamp`: Top view of the vortical structures obtained at two different time-steps.

5.2.3.2 Mean fields

The mean streamwise evolutions of the wall pressure and friction coefficient are gathered in Figure 5.11. After a short adaptation time, due to strong viscous phenomena at the leading edge of the plate, the pressure reaches a quasi-constant value up to $\frac{x}{x_c} = 0.25$ (Figure 5.11-left). It then experiences a steep increase when crossing the separation shock and reaches a plateau value of $\frac{p}{p_w} \simeq 1.4$. This plateau spans up to $\frac{x}{x_c} = 1.2$ where the reattachment shock further increases the pressure value to $\frac{x}{x_c} = 2.5$. This double plateau pattern is coherent with the inviscid theory and is recovered as soon as a two-strong-shock system is encountered [128]. It is noteworthy that in the turbulent case, where the separation bubble is much smaller, the reattachment shock is weaker, and therefore, the second pressure increase is smoother, but still present [21, 120].
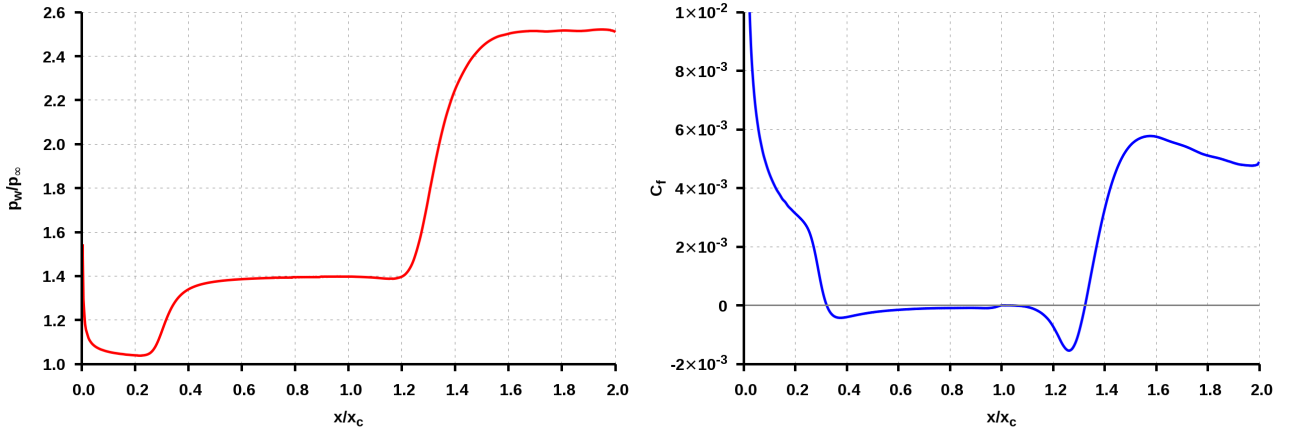
Figure 5.11: `SingleRamp`: Mean streamwise evolution of the mean wall pressure (left) and friction coefficient (right).

The analysis of the mean skin-friction coefficient (Figure 5.11-right) confirms the very large extent of the bubble, that has previously been evidenced by the first pressure plateau. Additionally, it can be observed that the separation bubble has a very peculiar shape, consisting in three distinct zones. The first one is characterised by its very large extent (spanning from $\frac{x}{x_c} = 0.3$ to $\frac{x}{x_c} = 1.0$) and very slightly negative values of C_f. On the other hand, the last zone ($1.1 < \frac{x}{x_c} < 1.3$) is subjected to a very short but intense backflow where C_f reaches its global minimum value. Between those two, a small zone of slightly positive friction coefficients, indicating that in this portion, the flow is from left to right, can be seen. Instead of being a unique separation bubble, this one can be defined as two small bubbles of distinct sizes and contrarotative vortices. This shape, that can be recovered in Figure 5.12, representing the negative-value contours of the mean stream-wise velocity, is similar to the one described by Ben Hassan Saïdi when considering the interaction between an oblique shock and a laminar boundary layer developing on a flat plate [14].

The mean-field of the turbulent kinetic energy (TKE), defined by $k = \frac{1}{2}\left(\overline{u_i' u_i'}\right)$, using Einstein summation, is represented in Figure 5.13. As expected when analysing Figure 5.5, TKE starts to be created at high levels in the shear layer above the separation zone.

Figure 5.12: `SingleRamp`: Negative-value contours of the mean streamwise velocity around the separation bubble.

It is the location where the initially laminar boundary layer undergoes its transition towards turbulence and it corresponds to the place where the large spanwise vortex rolls are created through a Kelvin-Helmholtz instability. The TKE then increases up to a maximum, occurring around the reattachment point. After this location, and due to the subsequent shock, the boundary layer thickens, leading to a decrease of TKE levels and progressively relax to a quasi-fully turbulent regime, characterised by the presence of hairpin vortices.

Figure 5.13: `SingleRamp`: Time- and spanwise-averaged turbulent kinetic energy field.

5.2.3.3   Probes and spectra

The successive streamwise positions of the separation and reattachment points, defined by the cell indexes i_s and i_r respectively, have been extracted from the computations of the friction coefficient at each time step. They are such that :

Separation:	$C_f^{i_s-1} > 0$	and	$C_f^{i_s} < 0$
Reattachment:	$C_f^{i_r} < 0$	and	$C_f^{i_r+1} > 0$

The time evolutions of i_s and i_r are represented in Figure 5.14. As far as the separation is concerned, the oscillations have been found to be very small. Being limited to only 2 indexes ($i_s = 103$ and $i_s = 104$), it has then been concluded that those oscillations were a numerical artefact due to the fact that the separation actually takes place inside
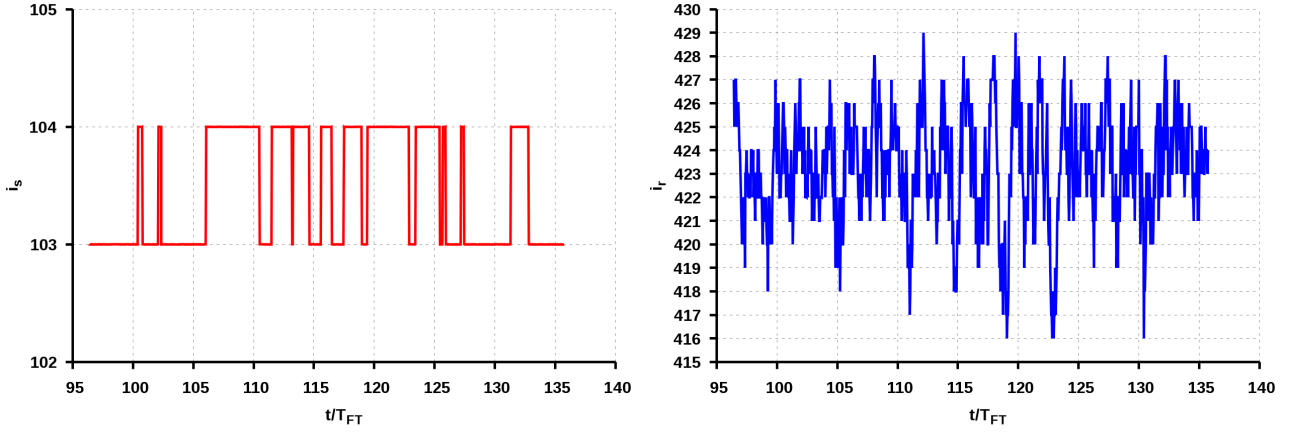
Figure 5.14: `SingleRamp`: Time evolution of the separation point (left) and reattachment point (right). i_s and i_r are the cell indexes at which the separation and reattachment occur, respectively.

the control volume. The reattachment point, on the other hand, is subjected to high-frequency longitudinal oscillations, spanning over more than 10 CVs.

Those observations have led to the conclusion that, unlike in the turbulent case, the *breathing* of the separation bubble is not recovered when considering an incoming vortex-free laminar boundary layer since. Indeed, if applicable, both separation and reattachment points would have been subjected to in-phase oscillations which is not the case here.

The normalized power spectra density obtained from Figure 5.14-right is plotted in Figure 5.15. Three distinct zones can easily be seen. The first one corresponds to the low frequencies ($St < 10^{-1}$). Between $St = 10^{-1}$ and $St = 3.10^{-1}$ a mid-frequency zone is observed, with the higher peak values. Finally, the high-frequency zone spreads from $St = 3.10^{-1}$ to $St = 8.10^{-1}$. Comparing to the physical analysis of Section 5.1, it appears that those three zones match with the range of the *breathing*, *flapping* and *vortex-shedding*. It has hence been demonstrated that the reattachment point, in the laminar case, is subjected to the same solicitations as in the turbulent case, unlike the separation point.

The biggest mistake would have been to conclude that the *breathing* of the separation bubble, not being observed in the laminar case, is essentially due to the vortical structures in the incoming boundary layer. A way to disprove this conclusion is to analyse the time evolution of any quantity at some points located in the separation bubble, close to the separation and reattachment point. Two candidates have been chosen and their locations can be seen in Figure 5.3. The first probe is located just downstream the separation point ($\frac{x_1}{x_c} = 0.45$) at a distance from the wall $z_1^+ \simeq 15$. The position of the second probe, in the vicinity of the reattachment point, is such that $\frac{x_2}{x_c} = 1.33$ and $z_2^+ \simeq 15$. Both probes are located at midspan. The time evolution of the streamwise velocity and the subsequent Power Spectra Density are gathered in Figure 5.16. The signal from probe 2 is quite representative of a turbulent velocity signal. The oscillations contain a lot of different frequencies and amplitudes. This is confirmed by the analysis of the power
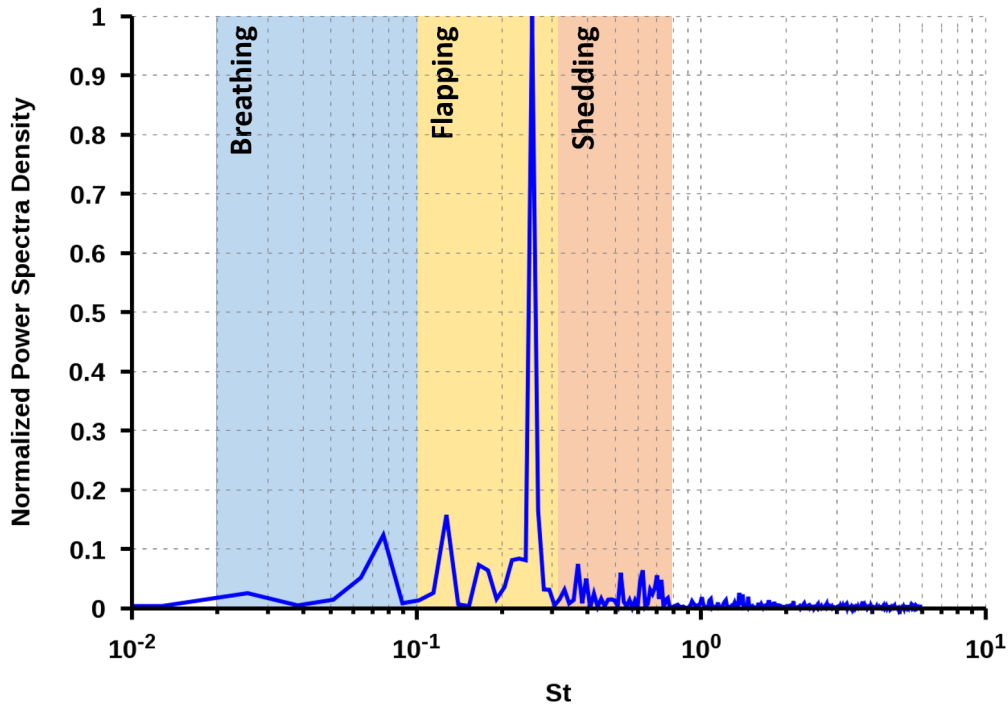
Figure 5.15: `SingleRamp`: Normalized Power Spectra Density obtained from the time evolution of the reattachment point (Figure 5.14.right)

spectra density where, as expected from the behaviour of the reattachment point, all the characteristic frequency of *breathing*, *flapping* and *shedding* are recovered. With respect to Figure 5.15, it is noteworthy that the spectrum obtained with a velocity signal is fuller than the one from the location of the reattachment point. This is due to the turbulent aspect of the flow away from the wall and this is particularly noticeable in the high-frequency zone corresponding to the *shedding*. In this part of the spectrum, much more frequencies are indeed found, mainly because of the randomness of the *shedding* in a turbulent framework.

The most interesting result concerns probe 1. As it has been written earlier, no evidence of any oscillations of the separation point has been found. However, when studying the spectrum coming from a probe close to this point, it is clear that all the frequency informations is propagated upstream up to this peculiar point. Indeed, except for a small attenuation of the peaks related to the *vortex-shedding*, all three unsteady phenomena are recovered. This is a fundamental result in the understanding of the bubble dynamics.

5.2.3.4 Conclusion

It has been evidenced that the phenomenon known as the *breathing* of the separation bubble, omnipresent in the turbulent case, is not recovered when an incoming laminar boundary layer is considered, even if the reattachment shock has been shown to oscillate at similar frequencies. It was first suspected that the physical phenomenon involved in the *breathing* could be the presence of coherent structure in the incoming boundary layer. A thorough study of the velocity signal coming from probes located in the vicinity of the
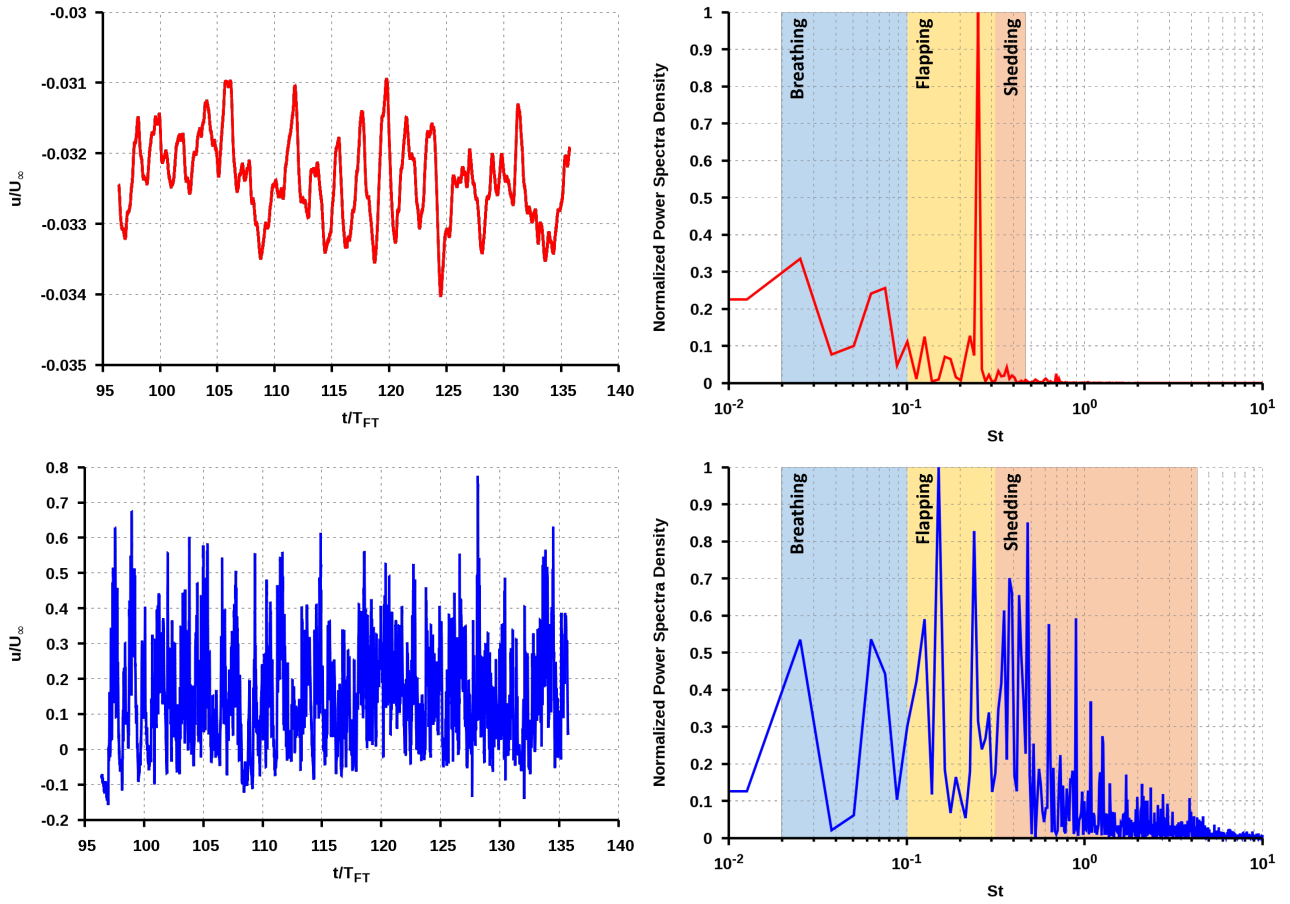
Figure 5.16: `SingleRamp`: Time evolution of the streamwise velocity and the susbequent Normalized Power Spectra Density obtained from two probes located in the separation bubble, in the vicinity of the separation (top) and reattachment (bottom) points.

separation point has demonstrated that, even if this point is fixed at the same location over time, it receives all the frequency information related to the *breathing*, *flapping* and *vortex-shedding*. Besides the absence of vortical structures, the second main difference between a laminar and a turbulent boundary layer lies in their ability to separate. It is indeed well-known that the laminar boundary layer is more inclined to separate from the wall than their turbulent counterpart. As a consequence, the extent of the separation bubble in this study (several dozens of boundary layer thicknesses) is much larger than in the classical turbulent compression ramp (only a few boundary layer thicknesses). During its travel upstream from the reattachment point towards the separation point, the information energy is damped through viscous dissipation. In the turbulent case, where the distance is rather small, the damping is also small and it does not have any consequences. On the contrary, in the laminar case, and even if it reaches the separation point, the information does not have enough energy to make it oscillate. The origin of the *breathing* is therefore to be sought in the dynamics of the shear layer instead of in the vortical structures upstream of the compression corner.

5.3   Compression-Expansion Ramp

In an effort to test the code's ability to handle complex geometries, the case of a compression-expansion ramp has been considered. In its first part ($x < 8.4\ mm$), this test-case is in almost every point identical to the compression ramp studied in the previous section. All the flow parameters (Table 5.1)as well as the cell-sizes are the same, resulting in a 41-million-CV mesh ($1,280 \times 320 \times 100$). The only difference comes from the use of a non-orthogonal mesh in the inclined portion, as previously discussed in Section 4.4. In order to create an expansion corner, a horizontal flat plate is added for $8.4\ mm < x < 16.8\ mm$.

The instantaneous coherent structures are represented in Figure 5.17, using the Q-criterion coloured by the streamwise velocity. All the features described in the previous section are recovered here: the transition occurring in the shear layer, the oblique shedding, the highly 3D reattachment shock, the relaxation towards a fully turbulent boundary layer....
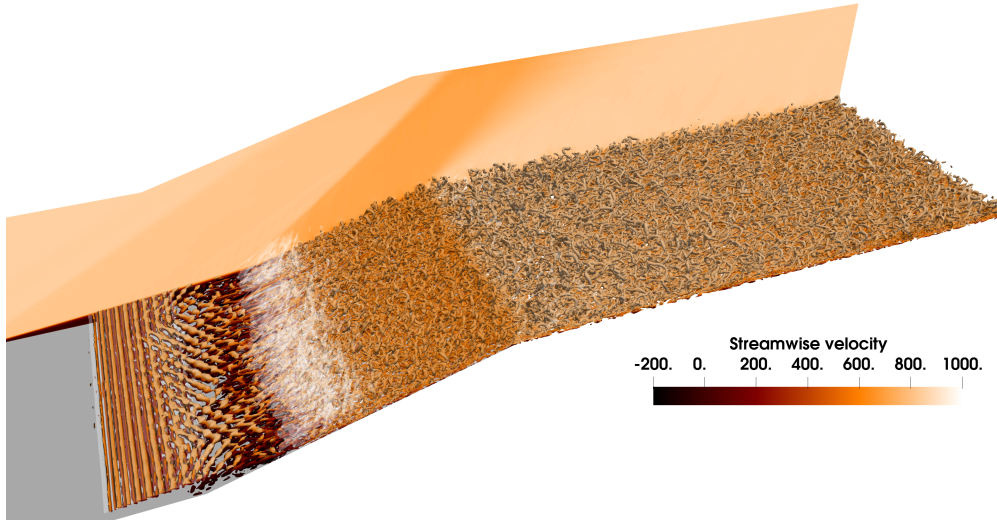
Figure 5.17: `CompExp`: Vortical structures evidenced by the **Q**-criterion, coloured by the streamwise velocity. The shock system is highlighted by isosurfaces of $div\ \mathbf{u}$.

Because of the outwards angle located at $x_e = 8.4\ mm$, the flow experiences a smooth deviation through a fan of expansion waves. As a result, the velocity is progressively increased at the expense of all the thermodynamic variables (pressure, density, and temperature). This phenomenon is clearly visible in Figure 5.18, representing a zoom of the vortical structures around the expansion corner, where the lighter colour indicates a higher velocity. That acceleration also leads to the elongation of the vortices in the streamwise direction.

The mean streamwise velocity contours (Fig. 5.19) show the complete shock system, consisting in a weak leading edge shock, followed by the separation shock, the reattachment shock, and finally the fan of expansion waves. The recirculation zone (in dark brown), very similar to the one obtained in the `SingleRamp` configuration, is well defined. The thickening of the boundary layer, in the second half of the domain, is also clearly visible,
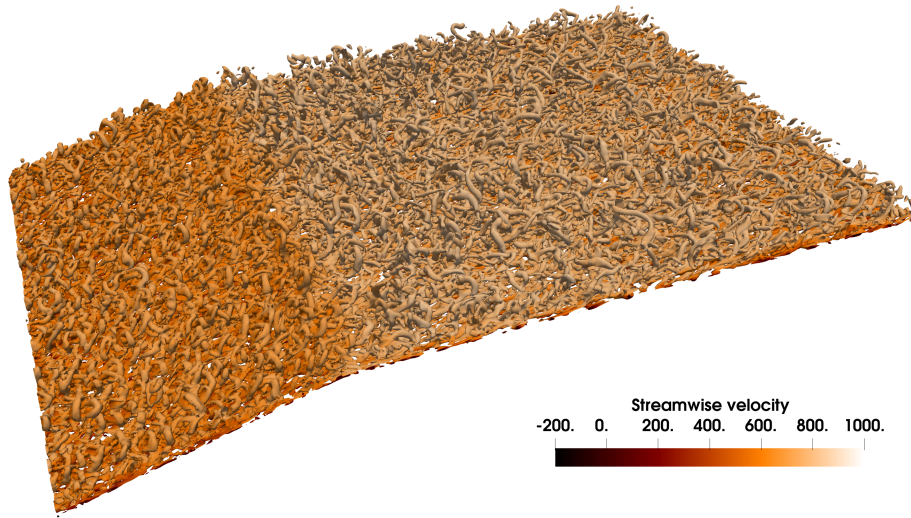
Figure 5.18: `CompExp`: Vortical structures evidenced by the Q-criterion, coloured by the streamwise velocity. Zoom on the expansion corner.

as the turbulent boundary layer develops along the flat part of the compression-expansion ramp.
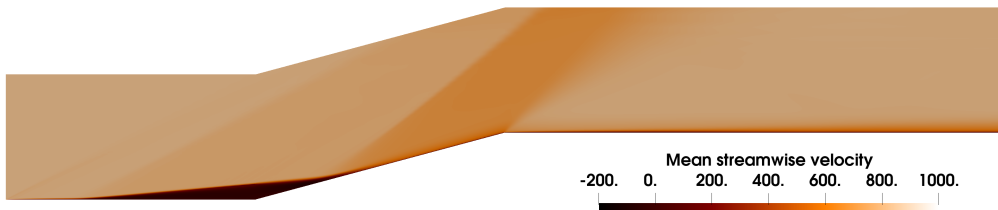
Figure 5.19: `CompExp`: Time- and spanwise-averaged streamwise velocity contours.

The mean, spanwise-averaged, streamwise evolution of the wall-pressure and skin-friction coefficient are gathered in figure 5.20. The result for the `SingleRamp` case have been included for comparison. As expected by the highly supersonic aspect of the flow, the presence of the expansion corner has no influence whatsoever on the upstream wall pressure distribution. The flow being supersonic everywhere, except in the thin subsonic part of the boundary layer, very close to the wall, it is not possible for the flow to have any information about the upcoming expansion corner. As a consequence, the flow in the first half of the domain is almost identical to the one observed in the `SingleRamp` case. It is noteworthy that the friction coefficient is in excellent agreement for $x < x_c$ but exhibits a larger, yet small, difference from the `SingleRamp` results in the ramp part. As a first

guess, this has been linked to the use of a non-orthogonal mesh but this should be investigated further. On the other hand, the steep peak located at $x = x_e$ is due to a poor treatment of the expansion corner in the computation of the wall-normal derivatives. Finally, it seems obvious from the shape of the friction coefficient for $x > x_e$ that the turbulent, zero-pressure-gradient regime has not been entirely reached by the boundary layer. Again, further investigations, involving for instance the plots of mean velocity profiles, Reynolds stresses or spectra, are needed in order to conclude with respect to those turbulent aspects.
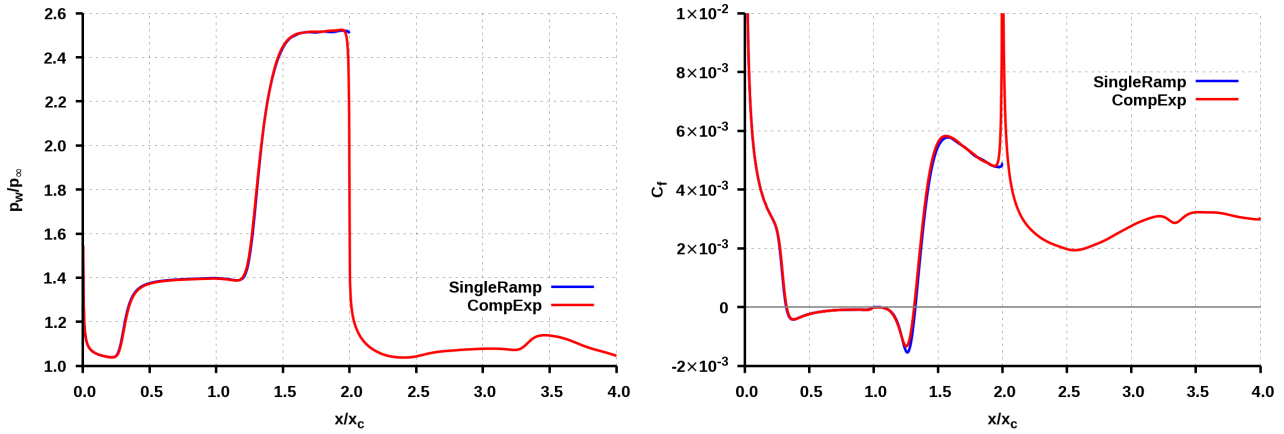
Figure 5.20: `CompExp`: Streamwise evolution of the spanwise-averaged wall-pressure (left) and friction coefficient (right). The results from the `SingleRamp` configuration have been plotted for comparison.

5.4 Conclusion

In this chapter, CHORUS has been used to performed Direct Numerical Simulations of the laminar flow around two geometries: a compression ramp (`SingleRamp`) and a compression-expansion ramp (`CompExp`). Those two cases have been chosen for their real practical interest since they can be found in almost every supersonic configurations.

Thanks to those highly-resolved, high-order simulations, it has been evidenced that in the `SingleRamp` configuration, and unlike in the turbulent case, the separation bubble induced by the ramp is not subjected to the *breathing* phenomenon, a succession of global shrinkage and enlargement phases. Alternatively, the separation shock is fixed in space while only the reattachment shock oscillates. It has been however demonstrated, that even if the separation shock does not move, all the frequency information associated to the *breathing* reaches it. As a consequence, the old mystery of the physical cause of the low-frequency streamwise oscillations of the separation zone have been solved since all the physical analysis performed in this study relates those oscillations to the vortex shedding in the shear layer.

Even if the physical analysis has not yet been finished, the simulations on the `CompExp` geometry has shown the ability of CHORUS to simulate the supersonic turbulent flow in

complex geometries with the presence of shocks. As expected, in the part of the flow shared with the `SingleRamp` case, the results are very close to each other. Nevertheless, further analysis is needed to improve our knowledge on the effect of the expansion corner on the flow.

Conclusions and perspectives

Summary of the work and concluding comments

In aeronautical and aerospace applications, the supersonic flow phenomena know as shock wave/boundary layer interactions have a clear appearance in almost all high-speed flow situations. The transonic flow over an airfoil, supersonic flow over a flat plate, over a compression ramp, and inside an air-intake, a nozzle, and a diffuser are well-known examples of these types of interactions. The interaction between a shock wave and a boundary layer provokes, under certain circumstances (high deflection angle or Mach number) a premature separation. The separation could create an unsteady recirculation bubble and, subsequently, a complex shock waves system consisting of the separation and reattachment shocks as well as a fan of expansion waves as well as shear layer. The interaction can also promote an early transition from laminar to turbulent flow. The oscillations in the recirculation bubble as well as in the subsequently reflected shock were noticed around the separation point in the form of low-frequency streamwise motion that could develop over some tenth of boundary layer thickness. The source of these oscillations is still not completely understood, but there are two strong premises which indicate that either it could be due to the random structures in the incoming boundary layer or to the shedding of coherent structures (vortices) in the mixing/shear layer downstream of the separation point. There are several studies in the past that concerned the SWBLI unsteadiness by dealing with the turbulent boundary layer and only a few studies dealing with the laminar boundary layer. Some of the previous studies concluded that the low-frequency streamwise motion is likely to be associated with the irregular structures in the incoming boundary layer.

The objective of the present thesis work was to provide a better insight into the SWBLI unsteadiness due to the low-frequency streamwise oscillations of the separation bubble. In order to investigate this low-frequency motion, the numerical simulation of the interaction between the shock wave and the laminar boundary layer in complex geometries has been carried out. To perform those simulations, a modified numerical approach for curvilinear coordinate, implemented in an in-house parallel (MPI) Finite-Volume based DNS/LES solver (CHORUS) developed at LIMSI-CNRS is used. A Monotonicity-Preserving shock-capturing scheme, based on the Lax-Wendroff method through a 7th order accurate coupled space and time approximations, is used for the convective fluxes of the Navier-Stokes equations. The diffusive fluxes are discretized by a classical second-order centered scheme. The code was initially built for simple geometries discretized with regular cartesian coordinates. The ability of the code dealing with curvilinear co-

ordinates for treating supersonic flows in relatively "complex geometries" with regard to high time and memory consuming DNS calculations were never tested before.

The first part of the thesis work was dedicated to the validation of the modified numerical approach employing high order scheme. The influence of the mesh distortion (hyperbolic tangent-distorted mesh and sine-distorted mesh) has been analysed for three well-documented test cases (Advection-diffusion case, Taylor-Green vortex, and the interaction between a weak shock and a temperature spot). The errors introduced by different types of deformation for the three test cases dealing with advection, turbulence, and shock wave were quantified. The errors created by the deformation of the mesh were found comparatively low if the control volumes stay close to a parallelepiped. A significant rise has been seen due to the introduction of the non-orthogonality of the mesh. All the results indicated that the modified numerical scheme accurately predicts the turbulent aspects and the strong capacity of the monotonicity-preserving (MP) method to capture discontinuity without any unrealistic oscillations in the solution.

The second part of the thesis work was the validation of the code in the framework of supersonic flows around a compression corner, which is the core of the present dissertation before innovative DNS is performed. The validation studies have been carried out for the case of both inviscid and viscous flows over a compression ramp and the comparison with theoretical as well as numerical data has been presented. This comparison has shown that the results obtained with CHORUS code are in good agreement with the reference data. We also validated this CHORUS code with our own test case using extensively tested supersonic flow solver, `rhoCentralFoam` of the OPENFOAM open-source numerical package. The results obtained have shown a rather good agreement, provided the differences in the two numerical approaches and it has allowed us to considered CHORUS as validated for Direct Numerical Simulations of compressible flows with shocks in complex geometries.

Consequently, the last part of the thesis deals with the physical analysis of the flow created by an incoming laminar boundary layer and developing around two geometries: a classical compression ramp and a compression-expansion ramp. As said earlier, the goal of those simulations was to determine whether the low-frequency oscillations of the recirculation zone can be related to the coherent structures in the incoming boundary layer. The results have demonstrated that, for both the configurations, the separation shock IS NOT subjected to the longitudinal oscillations.

By analysing the instantaneous fields, it was found that the large recirculation bubble is bounded by two shocks: the perfectly 2D separation shock upstream and the highly 3D reattachment shock downstream. Also, two important phenomena have been evidenced in the present study. The first one is the shedding of almost perfectly spanwise aligned vortices at the beginning of the transition, that will progressively fade and switch to an oblique mode of transition and eventually form hairpin vortices. However, no physical explanation could have been found in the present study but it seems that it should be sought on the side of the main modes of transition in the compressible mixing layers [130]. Another important phenomenon is the zone of vorticity-free flow in the vortical shed-

ding that occurs in the shear layer around the reattachment point. This phenomenon is of practical interest because it introduces another highly-3D aspect to the flow and, more importantly, an additional low-frequency phenomenon that could interact with the breathing, the flapping, or the vortex-shedding [59]. Unfortunately, no physical explanation could have been found in the present study.

The analysis of the mean skin-friction coefficient confirms the large extent of the recirculation bubble. Also, it can be observed that the separation bubble has a very peculiar shape, consisting of three distinct zones. Instead of being a unique separation bubble, this one can be defined as two small bubbles of distinct sizes and contrarotative vortices. The similar shape of the recirculation bubble is described by Ben Hassan Saïdi [14] when considering the interaction between an oblique shock and a laminar boundary layer developing on a flat plate. The analysis of mean turbulent kinetic energy confirms the presence of the large spanwise vortex rolls which are created through a Kelvin-Helmholtz instability in the shear layer above the recirculation bubble. Also, the same analysis confirms the relaxation towards a fully turbulent boundary layer characterized by the presence of hairpin vortices downstream of the reattachment point.

Three distinct frequency zones have been seen in the normalized power spectra density analysis. The first one corresponds to the low frequencies ($St < 10^{-1}$), the second one corresponding to medium-frequency zone is observed between $St = 10^{-1}$ and $St = 3.10^{-1}$, and the final one corresponding to the high-frequency zone spreads from $St = 3.10^{-1}$ to $St = 8.10^{-1}$. It appears that those three zones match with the range of the breathing, flapping, and vortex-shedding after comparing with the dynamics of the recirculation bubble. It has hence been demonstrated that the reattachment line, in the laminar case, is subjected to the same solicitations as in the turbulent case, unlike the separation line. However, a thorough study of the velocity signal coming from probes located in the vicinity of the separation point has demonstrated that, even if this point is fixed at the same location over time, it receives all the frequency information related to the breathing, flapping, and vortex-shedding. Besides the absence of vortical structures, the second main difference between a laminar and a turbulent boundary layer lies in their ability to separate. It is indeed well-known that laminar boundary layers are more inclined to separate from the wall than their turbulent counterpart.

Finally, this study concluded that the absence of oscillations in the laminar case is not, as originally thought, due to the absence of coherent structures in the incoming boundary layer but rather to the fact that, in the laminar case, the separation bubble extent is too large. As a consequence, even if the perturbations that make the bubble oscillate in the turbulent case are present for the laminar boundary layer, they are damped in such a way that they are not able to move the shock system and/or the recirculation zone. Also, the simulations for the compression-expansion ramp has shown the ability of CHORUS to simulate the supersonic laminar/turbulent flow in complex geometries with the presence of shocks and flow expansion. However, the physical analysis has not yet been finished, as expected, in the part of the flow shared with the single-ramp case, the results are very close to each other.

Perspectives

Further simulations of the SWLBLI must be performed with smaller separation bubbles (smaller Mach number or smaller ramp angle) in order to check if a smaller separation zone is oscillating as expected from the conclusion of physical analysis in chapter 5. Moreover, further laminar simulations are needed with different Reynolds numbers (larger or smaller ramps) to check if the transition process is involved in any way in the breathing. In the present study, two interesting phenomena related to the instantaneous coherent structures have been evidenced which are known as oblique shedding and the presence of regions of vortex free flow in the flow-field. Unfortunately, no physical explanation could have been found during the present study and further simulations will be undertaken in the near future to tackle that problem. In the context of turbulent flow, simulations will be performed by using Synthetic Eddy Method developed by Ben Hassan Saïdi [14] for the single ramp case. As it is difficult to perform experiments with a laminar boundary layer in the ramp case, the implementation of the SEM will also be used to validate the code with experiments in the turbulent case.

It would be also interesting to perform the simulations of more complex geometries, to check if the same dynamical behaviour (Görtler vortices) is present and could be replicated using the numerical approach used in this present study. In addition, direct numerical simulation will be carried out for over-expanded generic nozzle flows.

Bibliography

[1] J. Ackeret, F. Feldmann, and N. Rott, *Investigations of compression shocks and boundary layers in gases loving at high speed*, tech. rep., NACA-TM-1113, 1947.

[2] N. A. Adams, *Direct simulation of the turbulent boundary layer along a compression ramp at m= 3 and re θ= 1685*, Journal of Fluid Mechanics, 420 (2000), pp. 47–83.

[3] L. Agostini, L. Larchevêque, P. Dupont, J.-F. Debiève, and J.-P. Dussauge, *Zones of influence and shock motion in a shock/boundary-layer interaction*, AIAA journal, 50 (2012), pp. 1377–1387.

[4] H. Amann, *Experimental study of the starting process in a reflection nozzle*, The Physics of Fluids, 12 (1969), pp. I–150.

[5] J. D. Anderson, *Fundamentals of aerodynamics*, McGraw-Hill New York, 1991.

[6] J. D. Anderson, *Computational fluid dynamics*, vol. 206, Springer, 1995.

[7] J. D. Anderson, *Modern compressible flow: with historical perspective*, McGraw-Hill New York, 3 ed., 2003.

[8] J. D. Anderson Jr, *Hypersonic and high-temperature gas dynamics*, American Institute of Aeronautics and Astronautics, 2006.

[9] J. Andreopoulos, K. Muck, J. Dussauge, A. Smits, and M. Selig, *Turbulence structure in a shock wave/turbulent boundary-layer interaction*, AIAA journal, 27 (1989), pp. 862–869.

[10] P. Ardonceau, D. Lee, T. A. Deroquefort, and R. Goethals, *Turbulence behavior in a shock wave/boundary layer interaction*, in In AGARD Turbulent Boundary Layers 14 p (SEE N80-27647 18-34), 1980.

[11] G. Aubard, X. Gloerfelt, and J.-C. Robinet, *Large-eddy simulation of broadband unsteadiness in a shock/boundary-layer interaction*, AIAA journal, 51 (2013), pp. 2395–2409.

[12] H. Babinsky and J. K. Harvey, *Shock wave-boundary-layer interactions*, vol. 32, Cambridge University Press, 2011.

[13] H. Babinsky, Y. Li, and C. Pitt Ford, *Microramp control of supersonic oblique shock-wave/boundary-layer interactions*, AIAA journal, 47 (2009), pp. 668–675.

[14] I. BEN HASSAN SAIDI, *Numerical simulations of the shock wave-boundary layer interactions*, PhD thesis, Université Paris Saclay, 2019.

[15] S. BERESH, N. T. CLEMENS, AND D. DOLLING, *Relationship between upstream turbulent boundary-layer velocity fluctuations and separation shock unsteadiness*, AIAA journal, 40 (2002), pp. 2412–2422.

[16] S. BERLIN, M. WIEGEL, AND D. S. HENNINGSON, *Numerical and experimental investigations of oblique boundary layer transition*, Journal of Fluid Mechanics, 393 (1999), pp. 23–57.

[17] S. A. BERRY, A. H. AUSLENDER, A. D. DILLEY, AND J. F. CALLEJA, *Hypersonic boundary-layer trip development for hyper-x*, Journal of spacecraft and Rockets, 38 (2001), pp. 853–864.

[18] S. M. BOGDONOFF, C. KEPLER, AND E. SANLORENZO, *A study of shock wave turbulent boundary layer interaction at m= 3*, tech. rep., PRINCETON UNIV NJ JAMES FORRESTAL RESEARCH CENTER, 1953.

[19] S. M. BOGDONOFF AND A. SOLARSKI, *A preliminary investigation of a shockwave-turbulent boundary layer interaction*, tech. rep., PRINCETON UNIV NJ JAMES FORRESTAL RESEARCH CENTER, 1951.

[20] J.-P. BOIN AND J.-C. ROBINET, *Three-dimensional unsteady laminar shock-wave/boundary layer interaction*, tech. rep., LABORATORY OF DIGITAL SIMULATION IN MECHANICS OF FLUIDS (SINUMEF) PARIS . . . , 2004.

[21] P. BOOKEY, C. WYCKHAM, AND A. SMITS, *Experimental investigations of Mach 3 shockwave turbulent boundary layer interactions*, AIAA Paper, 2005-4899 (2005), pp. 1–15.

[22] C. BREHM, M. F. BARAD, J. A. HOUSMAN, AND C. C. KIRIS, *A comparison of higher-order finite-difference shock capturing schemes*, Computers & Fluids, 122 (2015), pp. 184–208.

[23] M. BREUER, *Numerical and modeling influences on large eddy simulations for the flow past a circular cylinder*, International Journal of Heat and Fluid Flow, 19 (1998), pp. 512–521.

[24] P. BUENO, N. CLEMENS, D. DOLLING, AND B. GANAPATHISUBRAMANI, *Cinematographic planar imaging of a mach 2 shock wave/turbulent boundary layer interaction*, in 43rd AIAA Aerospace Sciences Meeting and Exhibit, 2005, p. 441.

[25] O. BURGGRAF, *Asymptotic theory of separation and reattachment of a laminar boundary layer on a compression ramp*, tech. rep., OHIO STATE UNIV RESEARCH FOUNDATION COLUMBUS, 1975.

[26] O. R. BURGGRAF, D. RIZZETTA, M. WERLE, AND V. VATSA, *Effect of reynolds number on laminar separation of a supersonic stream*, AIAA Journal, 17 (1979), pp. 336–343.

[27] B. Cantwell, D. Coles, and P. Dimotakis, *Structure and entrainment in the plane of symmetry of a turbulent spot*, Journal of Fluid Mechanics, 87 (1978), pp. 641–672.

[28] J. E. Carter, *Numerical solutions of the Navier-Stokes equations for the supersonic laminar flow over a two-dimensional compression corner*, tech. rep., NASA-TR-R385, 1972.

[29] R. Chaplin, D. MacManus, F. Leopold, B. Martinez, T. Gauthier, and T. Birch, *Computational and experimental investigation into aerodynamic interference between slender bodies in supersonic flow*, Computers & Fluids, 50 (2011), pp. 155–174.

[30] D. Chapman, D. Kuehn, and H. Larson, *Investigation of separated flows in supersonic and subsonic streams with emphasis on the effect of transition, naca tech*, tech. rep., Note 3869, 1957.

[31] N. J. Cherry, R. Hillier, and M. E. M. P. Latour, *Unsteady measurements in a separated and reattaching flow*, Journal of Fluid Mechanics, 144 (1984), pp. 13–46.

[32] N. T. Clemens and V. Narayanaswamy, *Low-frequency unsteadiness of shock wave/turbulent boundary layer interactions*, Annual Review of Fluid Mechanics, 46 (2014), pp. 469–492.

[33] P. Comte and E. David, *Large-eddy simulation of görtler vortices in a curved compression ramp*, Experimentation, Modelling and Computation in Flow, Turbulence and Combustion, 1 (1996), pp. 45–61.

[34] J. Cousteix, *Aérodynamique: Turbulence et Couche Limite*, Cépaduès-Editions, 1989.

[35] U. Dallmann, *Three-dimensional vortex structures and vorticity topology*, Fluid Dynamics Research, 3 (1988), p. 183.

[36] V. Daru and C. Tenaud, *High resolution monotonicity-preserving schemes for unsteady compressible flows*, in Computational Fluid Dynamics 2002, Springer, 2003, pp. 241–246.

[37] V. Daru and C. Tenaud, *High order one-step monotonicity-preserving schemes for unsteady compressible flow calculations*, Journal of computational physics, 193 (2004), pp. 563–594.

[38] V. Daru and C. Tenaud, *Numerical simulation of the viscous shock tube problem by using a high resolution monotonicity-preserving scheme*, Computers & Fluids, 38 (2009), pp. 664–676.

[39] D. Daub, S. Willems, and A. Gülhan, *Experimental results on unsteady shock-wave/boundary-layer interaction induced by an impinging shock*, CEAS Space Journal, 8 (2016), pp. 3–12.

[40] J.-F. DEBIÈVE AND P. DUPONT, *Dependence between the shock and the separation bubble in a shock wave boundary layer interaction*, Shock Waves, 19 (2009), p. 499.

[41] N. R. DEEPAK, S. L. GAI, AND A. J. NEELY, *A computational investigation of laminar shock/wave boundary layer interactions*, The Aeronautical Journal, 117 (2013), pp. 27–56.

[42] G. DEGREZ, C. BOCCADORO, AND J. F. WENDT, *The interaction of an oblique shock wave with a laminar boundary layer revisited. an experimental and numerical study*, Journal of fluid mechanics, 177 (1987), pp. 247–263.

[43] J. DÉLERY AND J.-P. DUSSAUGE, *Some physical aspects of shock wave/boundary layer interactions*, Shock waves, 19 (2009), p. 453.

[44] J. DÉLERY, J. G. MARVIN, AND E. RESHOTKO, *Shock-wave boundary layer interactions*, tech. rep., ADVISORY GROUP FOR AEROSPACE RESEARCH AND DEVELOPMENT NEUILLY-SUR-SEINE (FRANCE), 1986.

[45] D. DOLLING, *Unsteadiness of the shock wave structure in attached and separated compression ramp flowfields*, in 16th Fluid and Plasmadynamics Conference, 1983, p. 1715.

[46] D. DOLLING AND M. MURPHY, *Unsteadiness of the separation shock wave structure in a supersonic compression ramp flowfield*, AIAA journal, 21 (1983), pp. 1628–1634.

[47] D. DOLLING AND C. OR, *Unsteadiness of the shock wave structure in attached and separated compression ramp flows*, Experiments in Fluids, 3 (1985), pp. 24–32.

[48] D. S. DOLLING, *High-speed turbulent separated flows: consistency of mathematical models and flow physics*, AIAA journal, 36 (1998), pp. 725–732.

[49] C. DONALDSON, *Effects of interaction between normal shock and boundary layer*, NACA CB 4A27, 4 (1944), p. 1.

[50] P. DUPONT, C. HADDAD, J.-P. ARDISSONE, AND J.-F. DEBIÈVE, *Space and time organisation of a shock wave/turbulent boundary layer interaction*, Aerospace Science and Technology, 9 (2005), pp. 561–572.

[51] P. DUPONT, C. HADDAD, AND J. DEBIEVE, *Space and time organization in a shock-induced separated boundary layer*, Journal of fluid Mechanics, 559 (2006), pp. 255–277.

[52] A. DURNA AND B. CELIK, *Time-periodic shock interaction mechanisms over double wedges at mach 7*, Shock Waves, 29 (2019), pp. 381–399.

[53] J.-P. DUSSAUGE, P. DUPONT, AND J.-F. DEBIÈVE, *Unsteadiness in shock wave boundary layer interactions with separation*, Aerospace Science and Technology, 10 (2006), pp. 85–91.

[54] A. DWIVEDI, J. W. NICHOLS, M. R. JOVANOVIC, AND G. V. CANDLER, *Optimal spatial growth of streaks in oblique shock/boundary layer interaction*, in 8th AIAA Theoretical Fluid Mechanics Conference, 2017, p. 4163.

[55] H. W. Emmons, *The laminar-turbulent transition in a boundary layer-part i*, Journal of the Aeronautical Sciences, 18 (1951), pp. 490–498.

[56] M. Erengil and D. Dolling, *Correlation of separation shock motion with pressure fluctuations inthe incoming boundary layer*, AIAA journal, 29 (1991), pp. 1868–1877.

[57] J. Fang, Y. Yao, A. A. Zheltovodov, Z. Li, and L. Lu, *Direct numerical simulation of supersonic turbulent flows around a tandem expansion-compression corner*, Physics of Fluids, 27 (2015), p. 125104.

[58] G. Fournier, *Contrôle de l'écoulement décollé autour de profils épais par la Simulation des Grandes Echelles*, PhD thesis, Université Paris 6, 2005.

[59] G. Fournier, A. Chpoun, Y. Fraigneau, and C. Tenaud, *Direct numerical simulations of the shock-induced separation of a laminar boundary layer*, in Direct and Large-Eddy Simulation X, Springer, 2018, pp. 327–332.

[60] G. Fournier, A. Chpoun, and C. Tenaud, *Shedding intermittency in a shock wave-laminar boundary layer interaction*, in 24th International Congress of Theoretical and Applied Mechanics, 2016.

[61] G. Gadd and J. Attridge, *A Note on the Effects of Heat Transfer on the Separation of a Laminar Boundary Layer*, HM Stationery Office, 1961.

[62] G. Gadd, D. W. Holder, and J. Regan, *An experimental investigation of the interaction between shock waves and boundary layers*, Proceedings of the Royal Society of London. Series A. Mathematical and Physical Sciences, 226 (1954), pp. 227–253.

[63] B. Ganapathisubramani, N. Clemens, and D. Dolling, *Planar imaging measurements to study the effect of spanwise structure of upstream turbulent boundary layer on shock induced separation*, in 44th AIAA Aerospace Sciences Meeting and Exhibit, 2006, p. 324.

[64] B. Ganapathisubramani, N. T. Clemens, and D. Dolling, *Effects of upstream boundary layer on the unsteadiness of shock-induced separation*, Journal of fluid Mechanics, 585 (2007), pp. 369–394.

[65] E. Garnier, P. Sagaut, and M. Deville, *Large eddy simulation of shock/boundary-layer interaction*, AIAA journal, 40 (2002), pp. 1935–1944.

[66] R. Giepman, F. Schrijer, and B. van Oudheusden, *A parametric study of laminar and transitional oblique shock wave reflections*, Journal of Fluid Mechanics, 844 (2018), pp. 187–215.

[67] C. J. Greenshields, H. G. Weller, L. Gasparini, and J. M. Reese, *Implementation of semi-discrete, non-staggered central schemes in a colocated, polyhedral, finite volume framework, for high-speed viscous flows*, International Journal for Numerical Methods in Fluids, 63 (2010), pp. 1–21.

[68] M. GRILLI, S. HICKEL, AND N. A. ADAMS, *Large-eddy simulation of a supersonic turbulent boundary layer over a compression–expansion ramp*, International Journal of Heat and Fluid Flow, 42 (2013), pp. 79–93.

[69] M. GRILLI, P. J. SCHMID, S. HICKEL, AND N. A. ADAMS, *Analysis of unsteady behaviour in shockwave turbulent boundary layer interaction*, Journal of Fluid Mechanics, 700 (2012), pp. 16–28.

[70] A. HADJADJ, *Large-eddy simulation of shock/boundary-layer interaction*, AIAA journal, 50 (2012), pp. 2919–2927.

[71] A. HADJADJ AND A. KUDRYAVTSEV, *Computation and flow visualization in high-speed aerodynamics*, Journal of Turbulence, 6 (2005), pp. 1–11.

[72] A. HADJADJ, Y. PERROT, AND S. VERMA, *Numerical study of shock/boundary layer interaction in supersonic overexpanded nozzles*, Aerospace science and technology, 42 (2015), pp. 158–168.

[73] R. J. HAKKINEN, I. GREBER, L. TRILLING, AND S. S. ABARBANEL, *The interaction of an oblique shock wave with a laminar boundary layer*, tech. rep., NASA Memorandum 2-18-59W, 1959.

[74] G. HALLER, *An objective definition of a vortex*, Journal of fluid mechanics, 525 (2005), pp. 1–26.

[75] A. HARTEN, *High resolution schemes for hyperbolic conservation laws*, Journal of Computational Physics, 49 (1983), pp. 357–393.

[76] A. HARTEN, B. ENGQUIST, S. OSHER, AND S. R. CHAKRAVARTHY, *Uniformly high order accurate essentially non-oscillatory schemes, iii*, in Upwind and high-resolution schemes, Springer, 1987, pp. 218–290.

[77] W. S. HINMAN AND C. T. JOHANSEN, *Mechanisms in the hypersonic laminar near wake of a blunt body*, Journal of Fluid Mechanics, 839 (2018), p. 33.

[78] Y. HOU, *Particle Image Velocimetry study of shock-induced turbulent boundary layer separation*, PhD thesis, University of Texas at Austin, 2003.

[79] C. HUNG AND R. MACCORMACK, *Numerical solutions of supersonic and hypersonic laminar compression corner flows*, AIAA Journal, 14 (1976), pp. 475–481.

[80] D. HUNT AND D. NIXON, *A very large eddy simulation of an unsteady shock wave/turbulent boundary layer interaction*, in Fluid Dynamics Conference, 1995, p. 2212.

[81] J. C. R. HUNT, A. WRAY, AND P. MOIN, *Eddies, stream, and convergence zones in turbulent flows*, tech. rep., Center for Turbulence Research Report CTR-S88, 1988.

[82] B. JOHN AND V. KULKARNI, *Effect of leading edge bluntness on the interaction of ramp induced shock wave with laminar boundary layer at hypersonic speed*, Computers & Fluids, 96 (2014), pp. 177–190.

[83] A. JOHNSON AND D. PAPAMOSCHOU, *Shock motion and flow instabilities in supersonic nozzle flow separation*, in 38th Fluid Dynamics Conference and Exhibit, 2008, p. 3846.

[84] E. KATZER, *On the lengthscales of laminar shock/boundary-layer interaction*, Journal of Fluid Mechanics, 206 (1989), pp. 477–496.

[85] D. KHOTYANOVSKY, A. KUDRYAVTSEV, AND A. SHERSHNEV, *Numerical study of the interaction of the supersonic flat-plate boundary layer with an oblique incident shock*, in AIP Conference Proceedings, vol. 2125, AIP Publishing, 2019, p. 030032.

[86] K. KIM AND R. ADRIAN, *Very large-scale motion in the outer layer*, Physics of Fluids, 11 (1999), pp. 417–422.

[87] A. KISTLER, *Fluctuating wall pressure under a separated supersonic flow*, The Journal of the Acoustical Society of America, 36 (1964), pp. 543–550.

[88] M. KIYA AND K. SASAKI, *Structure of large-scale vortices and unsteady reverse flow in the reattaching zone of a turbulent separation bubble*, Journal of Fluid Mechanics, 154 (1985), pp. 463–491.

[89] D. KNIGHT, H. YAN, A. G. PANARAS, AND A. ZHELTOVODOV, *Advances in cfd prediction of shock wave turbulent boundary layer interactions*, Progress in Aerospace Sciences, 39 (2003), pp. 121–184.

[90] D. D. KNIGHT AND G. DEGREZ, *Shock wave boundary layer interactions in high mach number flows a critical survey of current numerical prediction capabilities*, AGARD ADVISORY REPORT AGARD AR, 2 (1998), pp. 1–1.

[91] M. KRAUSE, M. BEHR, AND J. BALLMANN, *Modeling of transition effects in hypersonic intake flows using a correlation-based intermittency model*, in 15th AIAA International Space Planes and Hypersonic Systems and Technologies Conference, 2008, p. 2598.

[92] L. KRISHNAN, N. SANDHAM, AND J. STEELANT, *Shock-wave/boundary-layer interactions in a model scramjet intake*, AIAA journal, 47 (2009), pp. 1680–1691.

[93] A. KURGANOV AND E. TADMOR, *New high-resolution central schemes for nonlinear conservation laws and convection–diffusion equations*, Journal of Computational Physics, 160 (2000), pp. 241–282.

[94] M. I. KUSSOY, J. D. BROWN, J. L. BROWN, W. K. LOCKMAN, AND C. C. HORSTMAN, *Fluctuations and massive separation in three-dimensional shock-wave/boundary-layer interactions*, tech. rep., NASA-TM-89224, 1988.

[95] L. LARCHEVÊQUE, *Low-and medium-frequency unsteadinesses in a transitional shock–boundary reflection with separation*, in 54th AIAA aerospace sciences meeting, 2016, p. 1833.

[96] A. LAWAL, *Direct numerical simulation of transonic shock/boundary-layer interactions*, PhD thesis, University of Southampton, 2002.

[97] H. Lüdeke and N. D. Sandham, *Direct Numerical Simulation of the transition process in a separated supersonic ramp flow*, AIAA Paper, (2010).

[98] J. E. Lewis, T. Kubota, and L. Lees, *Experimental investigation of supersonic laminar, two-dimensional boundary-layer separation in a compression corner with and without cooling.*, AIAA journal, 6 (1968), pp. 7–14.

[99] J. Li, N. Grube, S. Priebe, and P. Martin, *LES study of shock wave and turbulent boundary layer interaction*, in 51st AIAA Aerospace Sciences Meeting including the New Horizons Forum and Aerospace Exposition, 2013, p. 984.

[100] J. Li, N. E. Grube, S. Priebe, and P. Martin, *Analysis of the large eddy simulation of a shock wave and turbulent boundary layer interaction*, in 43rd AIAA Fluid Dynamics Conference, 2013, p. 2734.

[101] C. Lian and C. L. Merkle, *Contrast between steady and time-averaged unsteady combustion simulations*, Computers & fluids, 44 (2011), pp. 328–338.

[102] H. W. Liepmann, A. Roshko, and S. Dhawan, *On reflection of shock waves from boundary layers*, tech. rep., CALIFORNIA INST OF TECH PASADENA, 1951.

[103] M. Loginov, N. Adams, and A. Zheltovodov, *Large-eddy simulation of shock wave/turbulent boundary layer interaction at high reynols number*, in PAMM: Proceedings in Applied Mathematics and Mechanics, vol. 4, Wiley Online Library, 2004, pp. 464–465.

[104] M. S. Loginov, N. A. Adams, and A. A. Zheltovodov, *Large-Eddy Simulation of shock-wave/turbulent-boundary-layer interaction*, Journal of Fluid Mechanics, 565 (2006), pp. 135–169.

[105] H. Lüdeke, R. Radespiel, and E. Schülein, *Simulation of streamwise vortices at the flaps of re-entry vehicles*, Aerospace science and technology, 8 (2004), pp. 703–714.

[106] K. Mahesh, S. K. Lele, and P. Moin, *The influence of entropy fluctuations on the interaction of turbulence with a shock wave*, Journal of Fluid Mechanics, 334 (1997), pp. 353–379.

[107] P. Martin, S. Xu, and M. Wu, *Preliminary work on dns and les of stbli*, in 33 rd AIAA Fluid Dynamics Conference and Exhibit, 2003.

[108] W. B. McClure, *An experimental study of the driving mechanism and control of the unsteady shock induced turbulent separation in a mach 5 compression corner flow.*, tech. rep., AIR FORCE INST OF TECH WRIGHT-PATTERSON AFB OH, 1992.

[109] R. Mittal and S. Balachandar, *Effect of three-dimensionality on the lift and drag of nominally two-dimensional cylinders*, Physics of Fluids, 7 (1995), pp. 1841–1865.

[110] F. Nasuti and M. Onofri, *Shock structure in separated nozzle flows*, Shock Waves, 19 (2009), pp. 229–237.

[111] A. T. Nguyen, H. Deniau, S. Girard, and T. A. De Roquefort, *Unsteadiness of flow separation and end-effects regime in a thrust-optimized contour rocket nozzle*, Flow, Turbulence and Combustion, 71 (2003), pp. 161–181.

[112] A. Pagella, A. Babucke, and U. Rist, *Two-dimensional numerical investigations of small-amplitude disturbances in a boundary layer at Ma = 4.8: Compression corner versus impinging shock wave*, Physics of Fluids, 16 (2004), pp. 2272–2281.

[113] V. Pasquariello, S. Hickel, and N. A. Adams, *Unsteady effects of strong shock-wave/boundary-layer interaction at high reynolds number*, Journal of Fluid Mechanics, 823 (2017), pp. 617–657.

[114] A. Paull, R. Stalker, and D. Mee, *Experiments on supersonic combustion ramjet propulsion in a shock tunnel*, Journal of Fluid Mechanics, 296 (1995), pp. 159–183.

[115] S. Piponniau, J.-P. Dussauge, J.-F. Debiève, and P. Dupont, *A simple model for low-frequency unsteadiness in shock-induced separation*, Journal of Fluid Mechanics, 629 (2009), pp. 87–108.

[116] S. Pirozzoli and F. Grasso, *Direct numerical simulation of impinging shock wave/turbulent boundary layer interaction at m= 2.25*, Physics of Fluids, 18 (2006), p. 065113.

[117] K. J. Plotkin, *Shock wave oscillation driven by turbulent boundary-layer fluctuations*, AIAA Journal, 13 (1975), pp. 1036–1040.

[118] J. Poggie and K. M. Porter, *Flow structure and unsteadiness in a highly confined shock-wave–boundary-layer interaction*, Physical Review Fluids, 4 (2019), p. 024602.

[119] S. Priebe and M. P. Martin, *Low-frequency unsteadiness in the dns of a compression ramp shockwave and turbulent boundary layer interaction*, in 48th AIAA Aerospace Sciences Meeting Including the New Horizons Forum and Aerospace Exposition, 2010, p. 108.

[120] S. Priebe and M. P. Martín, *Low-frequency unsteadiness in shock wave–turbulent boundary layer interaction*, Journal of Fluid Mechanics, 699 (2012), pp. 1–49.

[121] E. G. Rad and S. M. Mousavi, *Wall modeled large eddy simulation of supersonic flow physics over compression–expansion ramp*, Acta Astronautica, 117 (2015), pp. 197–208.

[122] P. Reijasse, F. Bouvier, and P. Servel, *Experimental and numerical investigation of the cap-shock structure in overexpanded thrust-optimized nozzles*, OFFICE NATIONAL D ETUDES ET DE RECHERCHES AEROSPATIALES ONERA-PUBLICATIONS-TP, (2002).

[123] O. Reynolds, *On the dynamical theory of incompressible viscous fluids and the determination of the criterion*, Philosophical Transactions of the Royal Society of London, Series A, 186 (1895).

[124] D. Rizzetta, O. Burggraf, and R. Jenson, *Triple-deck solutions for viscous supersonic and hypersonic flow past corners*, Journal of Fluid Mechanics, 89 (1978), pp. 535–552.

[125] D. P. Rizzetta, M. R. Visbal, and D. V. Gaitonde, *Large-eddy simulation of supersonic compression-ramp flow by high-order method*, AIAA Journal, 39 (2001), pp. 2283–2292.

[126] J.-C. Robinet, *Bifurcations in shock-wave/laminar-boundary-layer interaction: global instability approach*, Journal of Fluid Mechanics, 579 (2007), pp. 85–112.

[127] J.-C. Robinet, V. Daru, and C. Tenaud, *Two-dimensional laminar shock wave/boundary layer interaction*, in BAIL conference, Toulouse France, 2004.

[128] A. Roghelia, H. Olivier, I. Egorov, and P. Chuvakhov, *Experimental investigation of görtler vortices in hypersonic ramp flows*, Experiments in Fluids, 58 (2017), p. 139.

[129] A. Roshko and G. Thomke, *Supersonic turbulent boundary-layer interaction with a compression corner at very high reynolds number*, in Proc. ARL Symp. on Viscous Interaction Phenomena in Supersonic and Hypersonic Flow, 1969, pp. 109–138.

[130] N. D. Sandham, *A numerical investigation of the compressible mixing layer*, PhD thesis, Stanford University, 1989.

[131] A. Sansica, N. Sandham, and Z. Hu, *Forced response of a laminar shock-induced separation bubble*, Physics of fluids, 26 (2014), p. 093601.

[132] A. Sansica, N. D. Sandham, and Z. Hu, *Instability and low-frequency unsteadiness in a shock-induced laminar separation bubble*, Journal of Fluid Mechanics, 798 (2016), pp. 5–26.

[133] J. Seddon and E. Goldsmith, *Intake aerodynamics, aiaa education series, aiaa*, 1999.

[134] M. S. Selig, J. Andreopoulos, K. Muck, J. Dussauge, and A. Smits, *Turbulence structure in a shock wave/turbulent boundary-layer interaction*, AIAA journal, 27 (1989), pp. 862–869.

[135] G. S. Settles, T. J. Fitzpatrick, and S. M. Bogdonoff, *Detailed study of attached and separated compression corner flowfields in high reynolds number supersonic flow*, AIAA journal, 17 (1979), pp. 579–585.

[136] A. A. Sfeir, *Supersonic laminar boundary layer separation near a compression corner*, tech. rep., CALIFORNIA UNIV BERKELEY DIV OF AERONAUTICAL SCIENCES, 1969.

[137] C.-W. Shu, *Essentially non-oscillatory and weighted essentially non-oscillatory schemes for hyperbolic conservation laws*, in Advanced numerical approximation of nonlinear hyperbolic equations, Springer, 1998, pp. 325–432.

[138] C.-W. SHU AND S. OSHER, *Efficient implementation of essentially non-oscillatory shock-capturing schemes*, Journal of Computational Physics, 77 (1988), pp. 439–471.

[139] J. SIVASUBRAMANIAN AND H. F. FASEL, *Numerical investigation of shock-induced laminar separation bubble in a mach 2 boundary layer*, in 45th AIAA Fluid Dynamics Conference, 2015, p. 2641.

[140] A. J. SMITS AND K.-C. MUCK, *Experimental study of three shock wave/turbulent boundary layer interactions*, Journal of Fluid Mechanics, 182 (1987), pp. 291–314.

[141] M. R. SOLTANI, A. DALIRI, AND J. S. YOUNSI, *Effects of shock wave/boundary-layer interaction on performance and stability of a mixed-compression inlet*, Scientia Iranica. Transaction B, Mechanical Engineering, 23 (2016), p. 1811.

[142] L. SOUVEREIN, B. OUDHEUSDEN, F. SCARANO, AND P. DUPONT, *Unsteadiness characterisation in a shock wave turbulent boundary layer interaction through dual-piv*, in 38th Fluid Dynamics Conference and Exhibit, 2008, p. 4169.

[143] K. STEWARTSON AND P. WILLIAMS, *On self-induced separation ii*, Mathematika, 20 (1973), pp. 98–108.

[144] G. STRANG, *On the construction and comparison of difference schemes*, SIAM Journal on Numerical Analysis, 5 (1968), pp. 506–517.

[145] M. SUN, H. WANG, AND F. XIAO, *Jet in Supersonic Crossflow*, Springer, 2019.

[146] A. SURESH AND H. HUYNH, *Accurate monotonicity-preserving schemes with runge–kutta time stepping*, Journal of Computational Physics, 136 (1997), pp. 83–99.

[147] W. SUTHERLAND, *Lii. the viscosity of gases and molecular force*, The London, Edinburgh, and Dublin Philosophical Magazine and Journal of Science, 36 (1893), pp. 507–531.

[148] C. TENAUD, E. GARNIER, AND P. SAGAUT, *Evaluation of some high-order shock capturing schemes for direct numerical simulation of unsteady two-dimensional free flows*, International Journal for Numerical Methods in Fluids, 33 (2000), pp. 249–278.

[149] H. TENNEKES AND J. L. LUMLEY, *A first course in turbulence*, MIT press, 1972.

[150] V. THEOFILIS, *Global linear instability*, Annual Review of Fluid Mechanics, 43 (2011), pp. 319–352.

[151] K. W. THOMPSON, *Time dependent boundary conditions for hyperbolic systems*, Journal of computational physics, 68 (1987), pp. 1–24.

[152] E. F. TORO, *Riemann solvers and numerical methods for fluid dynamics: a practical introduction*, Springer Science & Business Media, 2013.

[153] E. TOUBER AND N. D. SANDHAM, *Oblique shock impinging on a turbulent boundary layer: low-frequency mechanisms*, AIAA Paper, (2008).

[154] E. TOUBER AND N. D. SANDHAM, *Comparison of three large-eddy simulations of shock-induced turbulent separation bubbles*, Shock Waves, 19 (2009), p. 469.

[155] O. H. UNALMIS AND D. DOLLING, *Experimental study of causes of unsteadiness of shock-induced turbulent separation*, AIAA journal, 36 (1998), pp. 371–378.

[156] P. VISWANATH, *Shock-wave-turbulent-boundary-layer interaction and its control: A survey of recent developments*, Sadhana, 12 (1988), pp. 45–104.

[157] M. A. VYAS, M. WAINDIM, AND D. V. GAITONDE, *Budget of turbulent kinetic energy in a shock wave/boundary-layer interaction*, in 46th AIAA Fluid Dynamics Conference, 2016, p. 3187.

[158] Z. J. WANG, K. FIDKOWSKI, R. ABGRALL, F. BASSI, D. CARAENI, A. CARY, H. DECONINCK, R. HARTMANN, K. HILLEWAERT, H. T. HUYNH, N. KROLL, G. MAY, P.-O. PERSSON, B. VAN LEER, AND M. VISBAL, *High-order CFD methods: current status and perspective*, International Journal for Numerical Methods in Fluids, 72 (2013), pp. 811–845.

[159] M. WERLE AND V. VATSAT, *New method for supersonic boundary-layer separations*, AIAA Journal, 12 (1974), pp. 1491–1497.

[160] C. H. K. WILLIAMSON, *Oblique and parallel modes of vortex shedding in the wake of a circular cylinder at low reynolds numbers*, Journal of Fluid Mechanics, 206 (1989), pp. 579–627.

[161] M. WU, P. BOOKEY, P. MARTIN, AND A. SMITS, *Analysis of shockwave/turbulent boundary layer interaction using dns and experimental data*, in 43rd AIAA Aerospace Sciences Meeting and Exhibit, 2005, p. 310.

[162] M. WU AND M. P. MARTIN, *Analysis of shock motion in shockwave and turbulent boundary layer interaction using direct numerical simulation data*, Journal of Fluid Mechanics, 594 (2008), pp. 71–83.

[163] H. YAN, D. KNIGHT, AND A. A. ZHELTOVODOV, *Large eddy simulation of supersonic compression corner using eno scheme*, tech. rep., RUTGERS-THE STATE UNIV NEW BRUNSWICKNJ DEPT OF MECHANICAL AND AEROSPACE . . . , 2001.

[164] H. YAN, G. URBIN, D. KNIGHT, AND A. A. ZHELTOVODOV, *Compressible large eddy simulation using unstructured grid: supersonic boundary layers and compression ramps*, International Confenference on the Methods of Aerophysical Research, Part, 1 (2000), pp. 215–224.

[165] Y. YAO, D. RINCON, AND Y. ZHENG, *Shock induced separating flows in scramjet intakes*, in International Journal of Modern Physics: Conference Series, vol. 19, World Scientific, 2012, pp. 73–82.

[166] B. ZANG, V. US, AND T. H. D. NEW, *Openfoam based numerical simulation study of an underexpanded supersonic jet*, in 55th AIAA Aerospace Sciences Meeting, 2017, p. 0747.

[167] A. ZHELTOVODOV, *Peculiarities of development and modeling possibilities of super-sonic turbulent separated flows*, in Separated Flows and Jets, Springer, 1991, pp. 225–236.

Titre: Simulations numériques de l'interaction onde de choc-couche limite en géométrie complexe

Mots clés: Mécanique des fluides, Ecoulements compressibles, Simulations Numériques Directes, Simulations des Grandes Echelles, Calcul Haute Performance, Maillages curvilignes

Résumé: L'objectif du présent travail de thèse est de fournir une meilleure compréhension des phénomènes physiques responsables des oscillations longitudinales basse fréquence de la bulle de séparation observées dans les écoulements supersoniques. Afin d'étudier ce mouvement à basse fréquence, des calculs (DNS) de l'interaction entre l'onde de choc et la couche limite laminaire dans des géométries complexes ont été réalisés. Pour effectuer ces simulations, la prise en compte des coordonnées curvilignes a été implémentée dans le solveur CHORUS massivement parallèle (MPI), basé sur la méthode des volumes finis et développé au LIMSI-CNRS. La première partie manuscrit est la validation de l'approche numérique. L'influence de la distorsion du maillage a été analysée à partir de plusieurs cas-test. Les erreurs introduites par différents types de déformation pour les trois cas-test considérés (advection, turbulence et écoulement avec onde de choc) ont été analysées. Dans la mesure où les volumes de contrôle restent proches d'un parallépipède, il a été montré que les erreurs dues à la déformation restaient faibles. Dans certains cas, il a été observé que l'introduction d'une non-orthogonalité du maillage entrainait une augmentation significative de ces erreurs. La deuxième partie concerne la validation du code dans le cadre de l'écoulement supersonique autour d'une rampe de compression, qui est le cœur de la présente étude. Les validations ont été réalisées dans le cas d'écoulements non visqueux et visqueux sur une rampe de compression et la comparaison avec des données théoriques et numériques a été présentée. Cette comparaison a montré que les résultats obtenus avec le code CHORUS sont en bon accord avec les données de référence. Cependant, ces études sont assez anciennes et de nombreux progrès ont été réalisés dans les méthodes numériques pour les simulations d'écoulements à grande vitesse. Malheureusement, il n'y a que peu d'études ré-

centes concernant des simulations ou des expériences d'écoulement entièrement laminaire autour de rampes ou d'autres géométries complexes qui auraient pu aider à évaluer la capacité de Chorus à calculer de tels ´écoulements. Il a donc été décidé de créer notre propre cas-test à l'aide d'un solveur de flux supersonique largement testé, rhoCentralFoam d'OpenFOAM. Les résultats obtenus ont montrés un assez bon accord au vu des différences fondamentales entre les deux approches. Ceci nous a donc permis de considérer que le code Chorus était validé et pouvait, avec une grande confiance, être utilisé pour réaliser des DNS dans le cadre d' écoulement compressibles autour de géométries complexes. En conséquence, le dernier chapitre s'est attelé à l'analyse physique de l'écoulement crée par le développement d'une couche limite laminaire autour de deux géométries: une rampe de compression classique et une rampe de compression-détente. Le but de ces simulations était de déterminer si les oscillations basse fréquence de la zone de recirculation pouvaient être reliées à la présence de structures cohérentes dans la couche limite incidente. Les résultats ont montré que, dans les deux configurations testées, AUCUNE oscillation n'est observée sur le choc de décollement ou sur la bulle de recirculation. L'analyse des spectres obtenus grâce à des sondes situées au voisinage du choc de décollement a néanmoins mis en évidence que toutes les fréquences associées aux oscillations étaient présentes dans ces signaux. La conclusion de cette étude est que l'absence des oscillations n'est pas, comme pensé initialement, due à l'absence de structures tourbillonnaires dans la couche limite incidente mais plutôt au fait que, dans le cas laminaire, la taille de la zone de recirculation est extrêmement importante. Ainsi, même si les perturbations responsables des oscillations dans le cas turbulent sont également présentes en régime laminaire, elles sont trop amorties pour pouvoir déplacer le choc de décollement et/ou la zone de recirculation.

Title: Numerical simulation of shock wave-boundary layer interaction in complex geometries

Keywords: Fluid Dynamics, Direct Numerical Simulations, Large-Eddy Simulations, HPC, Curvilinear meshes

Abstract: The objective of the present thesis work is to provide a better insight of the SWBLI unsteadiness due to the low-frequency streamwise oscillations of the separation bubble. To investigate this low frequency motion, DNS of the interaction between the shock wave and laminar boundary layer in complex geometries has been carried out. To perform those simulations, a modified numerical approach for curvilinear coordinate, implemented in an in-house parallel (MPI) Finite-Volume based DNS/LES solver (CHORUS) developed at LIMSI-CNRS is used. The first part of the thesis is the validation of the modified numerical approach. The influence of the mesh distortion has been analyzed from several test cases. The errors introduced by different types of deformation for the three test cases dealing with advection, turbulence, and shock wave were identifiable. The errors created by deformation of the mesh are found comparatively low if the control volumes stay close to a parallelepiped. In some cases, a significant rise has been seen due to the introduction of the nonorthogonality of the mesh. The second part is the validation of code in the framework of supersonic flows around a compression corner which is the core of the present dissertation. The validation studies have been carried out for the case of both inviscid and viscous flows over a compression ramp and the comparison with theoretical as well as numerical data has been presented. This comparison has shown that the results obtained with CHORUS code are in good agreement with the reference data. However, those studies are rather old and a lot of progress has been made in numerical methods for high-speed flow simulations. Unfortunately, there are only a few recent studies concerning simulations or experiments of fully laminar flow around ramps or other complex geometries that could have helped to assess Chorus' ability to compute such flows. It has then been decided to create our own test case using an extensively tested supersonic flow solver, rhoCentralFoam of the OpenFOAM open-source numerical package. The results obtained provided the difference in the two numerical approaches and allowed us to consider Chorus as validated for DNS of compressible flows with shocks in complex geometries. Consequently, the last chapter deals with the physical analysis of the flow created by a laminar boundary layer developing around two geometries: a classical compression ramp and a compression-expansion ramp. As said earlier, the goal of those simulations was to determine whether the low-frequency oscillations of the recirculation zone can be related to the coherent structures in the incoming boundary layer. The results have demonstrated that, for both configurations, the separation shock IS NOT subjected to longitudinal oscillations. However, when analysing the spectra from probes in the vicinity of the separation point, it has appeared that all the frequency information is contained in those temporal signals. The conclusion of this study is that the absence of oscillations in the laminar case is not, as originally thought, due to the absence of coherent structures in the incoming boundary layer but rather to the fact that, in the laminar case, the separation bubble extent is too large. As a consequence, even if the perturbations that make the bubble oscillate in the turbulent case are present for laminar boundary layer, they are damped in such a way that they are not able to move the shock system and/or the recirculation zone. The next step to this study would be to reduce either the freestream Mach number or the ramp angle in order to have a smaller recirculation bubble and check if the motion appear in that case.